Technische Universität München
Fakultät für Physik

Abschlussarbeit im Masterstudiengang Physik

Correlation analysis of same charged pions in MB pp collisions at $\sqrt{s} = 13$ TeV with an improved resonance model

Maximilian Korwieser

27. Juni 2022

Erstgutachter (Themenstellerin): Prof. L. Fabbietti
Zweitgutachter: Prof. L. Heinrich

Betreuer: Dr. V. Montovani-Sarti, Dr. D. Mihaylov

Abstract

The goal of this work is to study momentum correlations between pairs of same charge pions. In particular these correlations are interpreted via the formalism of femtoscopy, which is a powerful tool, linking the properties of the correlation function in momentum space to the interaction as well as the emission source of the particle pair in question. While the particle emission source has already been studied for charged pions, this work aims to elaborate on the influence of strongly decaying resonances and the resulting modifications to the source distribution.

Recent advances in the field allow via a Monte Carlo procedure to account for the first time for strongly decaying resonances in a quantitative manner, instead of using a phenomenological motivated source distribution. The approach was already successfully employed in a number of studies, unveiling the bare spatial extension of the particle emitting source, without the increase in size due to particles stemming from the decay of resonances. It was shown in dedicated source studies, conducted on p–p and p–Λ correlations, that baryons, after accounting for the particle specific resonances, share a common emission source, which scales with the average transverse mass m_{T} of the particle pair. In this work the hypothesis for a universal particles is tested by applying the same method to the meson sector.

In order to achieve this, the correlation function of same charge pions is extracted from pp collisions taken at center of mass energies of $\sqrt{s} = 13$ TeV by the ALICE experiment during the Run2 campaign. In the following the extension of the particle emitting source is estimated, differentially as a function of m_{T}, using the correlations in conjunction with a dedicated source model. The modifications due to strongly decaying resonances are studied quantitatively for the first time for pions, leading to better understanding how resonances of different lifetimes transform the source. Finally the resulting m_{T} scaling of the radii for the charged pion source functions are compared to the results obtained in the baryon sector and are found to be compatible in the case of comparable particle multiplicities.

The findings of this study support the case of a universal particle source regardless if the particle in question is a meson or a baryon and therefore contribute to the current understanding of hadronization. Further the found space momentum correlations can help to refine transport models, which to this day often neglect the space coordinates during the particle production. Eventually the results of this study may also be used studying more complicated pairings including charged pions, as the source is with this study quantified.

Contents

Chapter 1

Introduction

The strong interaction is governed by the theory of quantum chromodynamics (QCD). One of the most intriguing properties of QCD is the running coupling constant α_s shown in the left panel of Fig. 1.1. Depending on the momentum transfer Q of the interaction two interesting regions, namely confinement and asymptotic freedom, are predicted by the theory. As the momentum is the conjugate variable of space, the momentum transfer is inversely connected to the distances probed during the interaction. For very small Q, meaning large distances, the value of α_s grows, hence indicating the region of confinement, with the direct consequence that particles carrying the non-abelian color charges of the SU(3) algebra cannot be separated by arbitrarily large distances. Due to this fact in most cases it is more convenient to work within the framework of effective field theories with effective degrees of freedom, e.g. hadrons instead of quark and gluon fields, which mediate the strong interaction. Hadrons are composite objects and can be classified according to their valence quark flavor content. Baryons (e.g. proton, neutron) refer to a bound system of three valence quarks while mesons are build from a pair of a valence quark and a valence anti-quark (e.g π^+, ϕ). In the case of large Q, meaning small distances, asymptotic freedom is predicted as α_s tends to small values. Here it is expected that the confined quarks and gluons dissolve into a so called quark-gluon plasma (QGP). Finally it should be noted that in the regime of small Q, as α_s grows, perturbation theory breaks down and calculations usually are performed within the framework of lattice QCD. The advantage of the finite lattice size is the introduction of a cut-off energy, albeit for this reason predictions for light particles require huge computational resources and have to this date not reached a satisfactory precision.

In order to study the properties of the QGP heavy-ion collisions (HIC) at large scale accelerator facilities like the large hadron collider (LHC) or relativistic heavy-Ion collider (RHIC) are employed. A sketch of the phase-diagram of QCD matter is shown in the right panel of Fig. 1.1, and several experiments as well as the phase-space probed are marked. Depending on the collision energy, a different section of the phase-space is probed. Due to the approximately equal amount of matter and anti-matter produced in high energy collisions, the experiments at the LHC probe the region of small chemical potentials μ_B and large temperature T. By contrast, low energy experiments can be used to probe large chemical potentials at lower temperatures. The results of these studies indicate that the QGP behaves like an ideal liquid, with a shear-viscosity close to the lowest theoretical bound [3]. This discovery encouraged the use of hydrodynamics in order to describe key properties of the system. Indeed in HIC several collective effects are observed and thought to arise from collective behavior during the QGP phase of the collision, which translates to momentum correlations between final state particles [4]. One example of a collective phenomenon is flow, which studies the momentum distribution of particles in the plane transverse to the beam axis. Another QCD related collective effect, is the creation of highly collimated streams of hadrons, called jets. A jet originates from a highly virtual quark or gluon, produced in a hard scattering, which branches into several different less virtual quarks and gluons, leading to a shower of quarks and gluons. Eventually, since confinement does not allow for free quarks and gluons to be

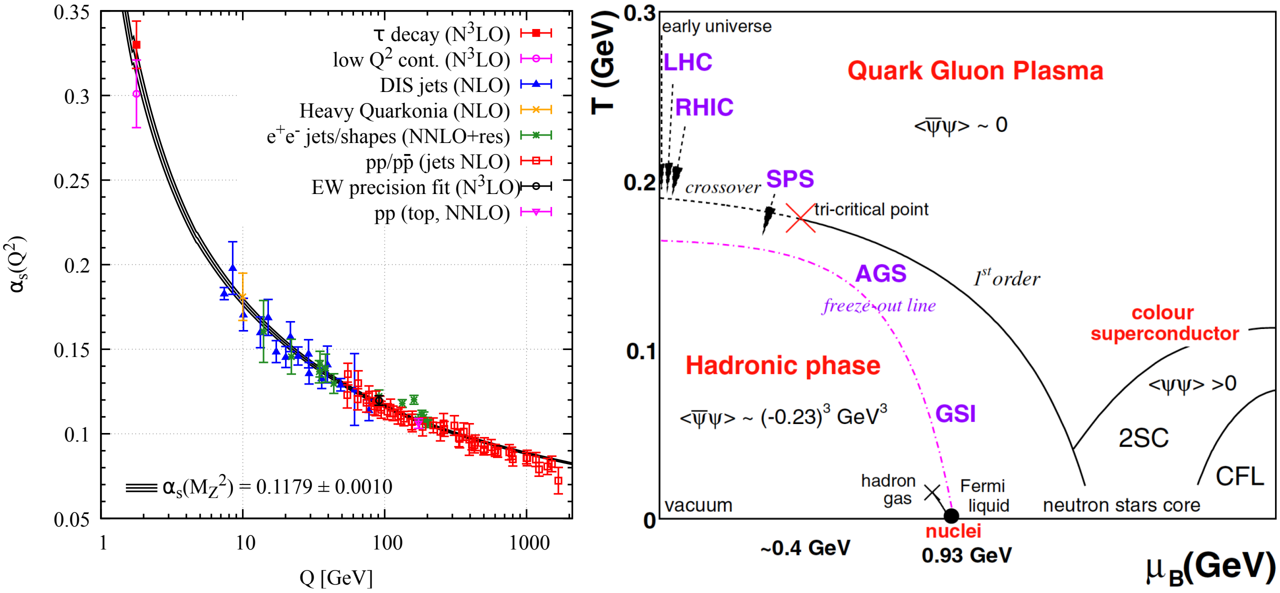

Figure 1.1: *Left*: World data of the strong coupling constant α_s taken from [1]. *Right*: Schematic depiction phase-diagram of QCD matter, the phase-space probed by several different large scale experiments is indicated [2].

present in the final state, the partons inside the shower will form hadrons. Thus, all hadrons produced from a common parton will be strongly correlated.

In between the QGP phase and the detection of the final state particles hadronisation, the process by which hadrons are formed from previously free quarks and gluons, must occur. It is important to note that while the hadro-chemistry is fixed on-wards from the point of hadronisation, the momenta of the produced particles can still be modified by final-state interactions and re-scatterings. Although the details of hadronisation are not yet fully understood, it is instructive to think of a 4D hypersurface, expanding with time, from which hadrons are emitted. In the context of HIC, this process is linked to the nature of the QGP. Within this picture the hypersurface of hadronisation characterizes the particle emission and carries the imprint of the collective behavior from the QGP phase. Hence it is expected to find signatures of collectivity in the emission source. In order to investigate the source femtoscopy was developed, which strives to realize measurements of momentum correlations between pairs of particles. The main paradigm becomes clear by inspecting the most important femtoscopic relation, given by the Koonin-Pratt equation

$$C(k^*) = \int d^3r^* S(r^*) |\psi(r^*, k^*)|^2. \tag{1.1}$$

The particle emitting source $S(r^*)$ contains the full information about the relative distances at which particles are emitted from the hadronisation hypersurface and hence is sensitive to collective effects during the QGP phase. The relative wave-function of the pair $\psi(r^*, k^*)$ obeys the Schrödinger equation. Therefore analyzing pairs for which $\psi(r^*, k^*)$ is known, gives the opportunity to study details about the particle emitting source. From calculations within hydrodynamic models a scaling behavior for the size of the source as a function of either the average transverse momentum of a pair k_{T}[1] or the transverse

[1] The average transverse momentum of a pair of particles is denoted by $k_{\mathrm{T}} = \frac{1}{2}|\mathbf{p}_{\mathrm{T}1} + \mathbf{p}_{\mathrm{T}2}|$, where $\mathbf{p}_{\mathrm{T}_i}$ is the transverse momentum of particle i.

mass ${m_{\mathrm{T}}}^2$ is expected. Indeed the measurements carried out so far by the ATLAS [5], CMS [6] and ALICE [7] collaborations provide evidence of this scaling.

Unlike the studies regarding the source in large systems, such as in Pb–Pb collisions, the study of the source in small systems, namely in pp collisions, is far from being completed. Differences between the two are expected, since in small systems no QGP should be formed. Nevertheless, a hypersurface can still be used to characterize the emission. In these analyses most often a Gaussian emission profile is assumed, however other shapes such as Cauchy or Levy stable distributions are also tested. Moreover, the smaller scale of the collision system leads to the fact that the emission hypersurface coincides with the hadronization (chemical freezeout), as a re-scattering phase does not occur. Further, in high energy collisions the production of hadrons is likely to be dominated by hard QCD scattering processes, which should be independent on the type of quarks involved. These considerations can be used to assume that there is a common emission for all hadrons, a hypothesis that was verified for protons, Λ [8] and most recently kaons [9, 10]. In the present work this hypothesis will be further investigated for mesons. Following the central equation of femtoscopy Eq. (1.1), fixing the particle emitting source from one pair of known interaction allows to test different relative wave-functions for another pair. Hence this method provides for a direct access to study the interaction between particles. This approach was successfully applied to a wide array of particle pairs, e.g. p–Λ, Λ–Λ, p–Σ^0, p–$\mathrm{K}^{\pm}$, p–Ξ, p–Ω, p–ϕ [8, 11–13], and for every analysis the source was benchmarked with the help of the well-constrained p–p correlation function [8]. Additionally, like in the case of HIC, the m_{T} scaling of the source was also observed in pp collisions. Further, measurements of flow observables [14, 15] and enhanced strangeness production [16, 17], signatures previously attributed to collective behavior in HIC, have been found in pp collisions, posing the question of the existence of collectivity in small systems.

The goal of this work is to study the source for same charge pion correlation functions in pp collisions. Unlike in the case of baryon pairs the analysis of meson pairs is hampered by the presence of an additional source of background, namely, mini-jets, in which the momentum correlations between mesons produced within the same jet cone lie below the femtoscopy signal. As both mesons within the jet are already highly collimated, when they are produced, the femtoscopic signal is contaminated and a procedure is needed in order to suppress contributions from such events. The »jettyness« of an event can be estimated with an event shape observable, the so-called sphericity, which measures the anisotropy of the particle momenta in the transverse plane (see sec. 3.1). Alternatively the underlying event topology can be studied with the help of Monte Carlo event generators where no femtoscopic signal is present. For this work both approaches will be used. Another challenging part of the analysis is the assessment of charged pions stemming from decays of short lived ($c\tau_{\mathrm{res}} < 5\,\mathrm{fm}$) resonances. A resonance will decay according to the well known exponential law and hence propagate a certain distance from the hadronisation hypersurface, effectively enlargening the source size. This effect is most pronounced for resonances with a decay length that is on the order of the size of the particle emitting source. Hence the expectation is that the source can be accurately modeled by assuming a Gaussian distribution, which is folded with the exponential decay functions of the contributing resonances [8]. Till now the non-gaussianity of the source for charged pion correlations has always been accounted for by using either a Cauchy or Levy stable distribution and results employing these are available for the CMS [18], LHCb [19] and ATLAS [20] collaborations. Nevertheless, with this approach the source is modelled only effectively, without a quantitative description of the underlying physics.

The motivation for this work is to study the hypothesis that the primordial source is Gaussian and common to all hadrons, mesons and baryons alike. The first quantitative study of the modification of

[2] The transverse mass m_{T} is calculated according to $m_{\mathrm{T}} = \sqrt{k_{\mathrm{T}}^2 + m^2}$ where m is the average mass of the particle pair.

the emission source due to the effect of resonances feeding to charged pions will be presented. The existing results on the topic of a common emission in small systems are only gathered by studying baryon-baryon pairs, hence probing particles with large transverse masses. The present study extends to the mesonic sector, accessing the low m_{T} region. The final results are presented for different particle multiplicities.

1.1 Correlation functions

1.1.1 Overview of femtoscopy

Originally the technique was introduced by the British astronomers Robert Hanbury Brown and Richard Q. Twiss about 70 years ago in an attempt to relate intensity correlations of incoming photons to the apparent angular size of the emitting source, in this case distant stars. This revolutionized the application of intensity interferometry leading to a new method to determine the apparent angular size of stars [21]. It was later realized that the same mathematical apparatus can be applied to microscopical systems, due to the particle wave duality in quantum physics. As the study of particle emitting sources is of utmost importance in the field of particle physics, the technique was subsequently adopted by Goldhaber et al. [22] to be used in experiments located at large high energy particle accelerator facilities, such as the LHC and forerunners.

In the particle physics community this method of measurement is commonly referred to as femtoscopy, derived from the fact that the particle sources produced in pp, p–Pb or Pb–Pb collisions are typically on the order of a few fm. While one often refers to particle emitting sources within the heavy-ion community, in fact the region of homogeneity (ROH) is probed, which gives an estimate on the spatial extension of a region from which pairs of particles with a particular pair-momentum are emitted. Hence the spatio-temporal extension of the total source volume is only the upper limit of the probed ROH, and inversely the ROH can be regraded as a lower limit of the extension of the total source volume.

1.1.2 Defining the observables

The observable of interest in femtoscopy is the two-particle momentum correlation function, which is defined as the probability to find simultaneously two particles with three momenta $\mathbf{p}_1$ and $\mathbf{p}_2$ divided by the product of the corresponding single particle probabilities

$$C(\mathbf{p}_1, \mathbf{p}_2) \equiv \frac{P(\mathbf{p}_1, \mathbf{p}_2)}{P(\mathbf{p}_1) \cdot P(\mathbf{p}_2)}. \tag{1.2}$$

These probabilities are directly related to the inclusive Lorentz invariant particle spectra $P(\mathbf{p}_1, \mathbf{p}_2) = E_1 E_2 \frac{\mathrm{d}^6 N}{\mathrm{d}^3\mathbf{p}_1 \mathrm{d}^3\mathbf{p}_2}$ and $P(\mathbf{p}_{1,2}) = E_{1,2} \frac{\mathrm{d}^3 N}{\mathrm{d}^3\mathbf{p}_{1,2}}$. Clearly in absence of any correlation signal the value of $C(\mathbf{p}_1, \mathbf{p}_2)$ equals unity, since $P(\mathbf{p}_1, \mathbf{p}_2)$ factorizes into the single particle probabilities.

In order to study the size of the particle emitting source certain approximations regarding the emission process and the momenta of the particles are necessary. Details about the approximations and their justifications are discussed extensively in [23], therefore here only the main result, the Koonin-Pratt relation, shall be highlighted. The Koonin-Pratt relation expresses the correlation as a function of the relative momentum of the pairs

$$C(k^*) = \int d^3 r^* S(r^*) |\psi(r^*, k^*)|^2, \tag{1.1}$$

$S(r^*)$ is the source function and contains the normalized distribution of the relative distance r^* between the particle pairs in their rest frame[3] (PRF), and $\psi(r^*, k^*)$ denotes the relative wave function of the particle pair. The single particle momentum k^* in the PRF is defined as $k^* = \frac{1}{2}|\mathbf{p}_1^* - \mathbf{p}_2^*|$, with $\mathbf{p}_1^*$ and $\mathbf{p}_2^*$ being the momentum vectors of the two particles. The wave function is determined by the interaction potential between the two particles. And is computed by solving the Schroedinger equation. In this work, the correlation function for the pair of bosons π^+–π^+ and π^-–π^- , for which the wave function is well understood by theory, is used in conjunction with Thermal-FIST [24] and EPOS [25] to obtain a description of the source function integrating the effects of feeddown from resonances.

The definitions of the correlation function given by Eq. (1.2) and Eq. (1.1) are identical. In order to link these definitions to experimentally accessible variables Eq. (1.2) is projected onto k^*

$$C(k^*) = \mathcal{N} \frac{S_{\text{same}}(k^*)}{M_{\text{mixed}}(k^*)}, \tag{1.3}$$

in which $S_{\text{same}}(k^*)$ represents the measured yield of correlated pairs (same-event sample), while $M_{\text{mixed}}(k^*)$ serves as an uncorrelated reference (mixed-event) sample. The former is obtained by pairing particles produced in the same physical collision (event), while the latter is obtained using event mixing techniques, in which the pairs are build from two particles stemming from different events. This procedure ensures that both particles cannot be correlated and hence the distribution of these pairs can be factorized into single particle distributions.

Finally the normalization parameter $\mathcal{N}$ is chosen such that the mean value of the correlation function equals unity at large k^* values, where no signal from final-state interactions is expected. The k^* up to which femtoscopic signal is expected can be estimated by making use of the uncertainty principle $\Delta x \cdot \Delta p > (\hbar/2)$, taking $\Delta x \approx 1\,\text{fm}$, which is a realistic value for the inter-hadron distance in pp collisions at the hadronisation hypersurface, the resulting momentum range is around $200\,\text{MeV}/c$. Therefore the region used for the normalization is typically located at k^* values above $0.2\,\text{GeV}/c$, however the presence of non-femtoscopic correlations might bias the normalization of the experimental correlation. For this reason the normalization $\mathcal{N}$ is often chosen arbitrary in a region corresponding to a flat correlation function, for this analysis $k^* \in (0.35 - 0.40)\,\text{GeV}/c$. Any subsequent comparisons to theoretical models are typically performed by allowing a re-normalization of the correlation function, embedded in a so-called non-femtoscopic baseline (see ch. 5.4).

1.1.3 Key features of correlation functions

Correlation functions exhibit intuitive properties regarding their interpretation, in this section a short overview of these is given. As already mentioned above in case of non-interacting particles the correlation function equals unity, for the case of an attractive interaction the correlation function will lie above unity, whereas the opposite is true for repulsive interactions. In addition to effects of the interaction, for identical indistinguishable particles the correlation function is sensitive to the symmetrization of the wave function. Depending on the spin (S) of the pair in question the effect of the symmetrization can lead to an enhancement in $C(k^*)$ or a depletion.

There are further effects that can lead to very specific shapes in the correlation function, such as the presence of coupled-channels (CC) [26], or decays into the pair of interest. However, for the study of same charge pion correlations the effect of CC are not relevant, while the contamination from resonances is present only for pairs of oppositely charged pions. For this reason the same charged pions provide a cleaner access to the femtoscopic signal related to the emission and are used in this work.

[3] Here, and throughout the subsequent chapters, all quantities evaluated in the pair rest frame (PRF) are denoted by *.

Chapter 2

Experimental Setup

In this chapter the detector used for data taking is introduced, while giving an overview of the most important detector systems as well as their usage withing the context of this work.

2.1 Event recording

Before an explanation of the detector is provided, a brief introduction about the basic notion of an event, how the detection works in principle, and finally what information can be extracted, is given. At the LHC the beam of protons is segmented into bunches, which are then successively accelerated till the maximum energy is reached[1]. Each bunch contains approximately 1.15×10^{11} protons, the bunches are separated in time by 25 ns and in total up to 5600 bunches can be stored in the accelerator.

The four large experiments (ALICE, CMS, LHCb and ATLAS) are positioned at the so-called interaction points, at which bunch-crossing are possible. Should during a bunch-crossing an inelastic interaction between two protons, stemming from the two bunches, occur and be selected by the trigger, the event recording is started. The triggers usually consist of several stages and are tuned to select primarily events, which are of interesting to physics analyses. The decision to trigger can e.g. involve the number of produced charged particles, within a certain rapidity, also commonly referred to as event multiplicity.

As the event recording is started all detector systems begin to collect information, meaning the signals induced by the traversing charged particles are recorded. The signals are produced due to interactions of the charged particles with the detector material leading to an energy deposition that can be read out. From the gathered data it is possible to reconstruct, with the help of dedicated reconstruction algorithms, the track of the individual charged particle, the energy as well as the momentum. The collection of the former is used to estimate the primary vertex, the point at which the initial inelastic interaction took place, while the latter are used for the single particle identification (PID) (see sec. 2.3). Additionally, should a weakly decaying resonance be produced, the tracking information can also be used to estimate the position of secondary vertex, the point at which the weak decay occurred.

Measuring particles from overlapping events contributes as so called pile-up and must be taken into account as a source of background. The summary of all the event data constitutes then the event, which is used as an input to the physics analysis.

[1]Details about each individual acceleration stage can be found in [27].

2.2 A Large Ion Collider Experiment (ALICE)

The ALICE (A Large Ion Collider Experiment) detector [28], located at the LHC, is an experiment originally dedicated to studies of heavy-ion collisions and the formation of quark-gluon plasma and consists of 17 different submodules, which serve the purpose of enabling precise particle identification and track reconstruction. In Fig. 2.1, the schematic structure of ALICE during RUN2, is presented. The central cylindrical part of ALICE is permeated by a magnetic field of $B = 0.5$ T [28], which is generated by the L3 solenoid magnet (10 in Fig. 2.1). The field lines are collinear to the beam pipe, and hence enable the measurement of the momentum for charged particles due to the Lorentz force. In the following, only the submodules which are relevant for this work are discussed.

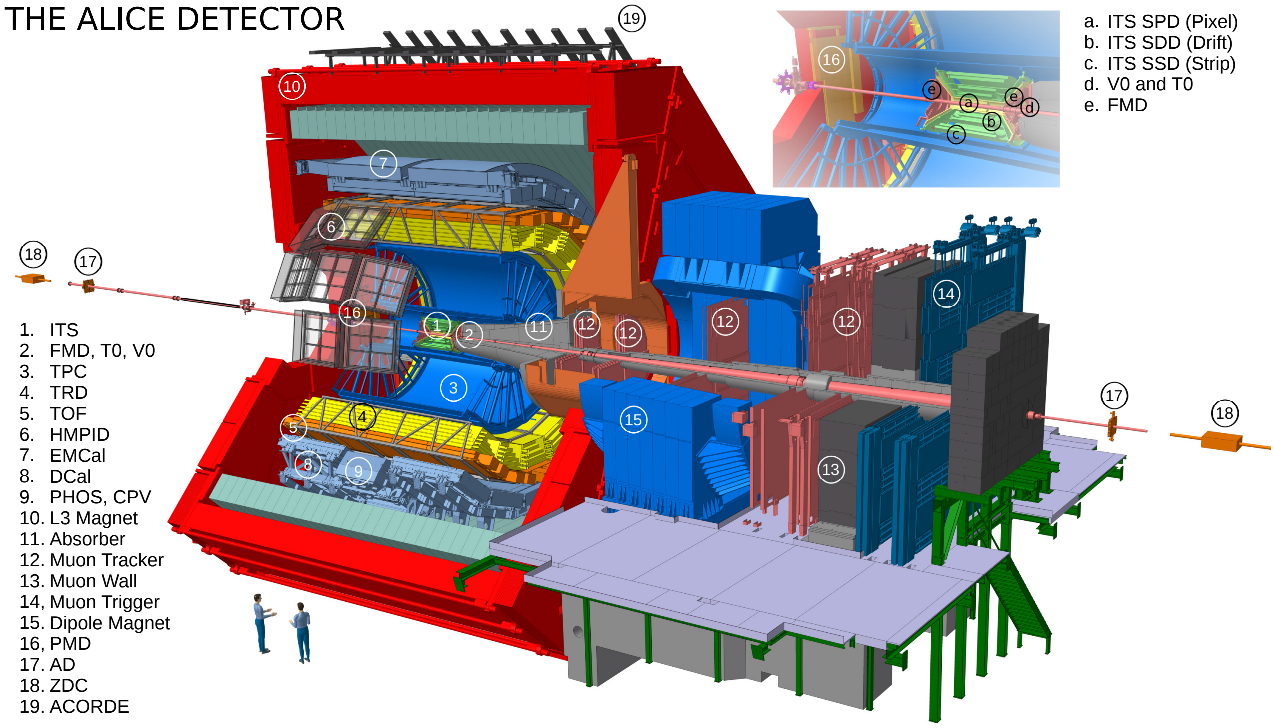

Figure 2.1: ALICE detector, during RUN2, with pointers to the sub-modules taken from [29].

2.2.1 Inner Tracking System

The ITS (Inner Tracking System, 1 in Fig. 2.1) is the innermost detector module and consists of 6 layers of silicon detectors. The two innermost layers correspond to the Silicon Pixel Detector (SPD), while the two intermediate layers correspond to the Silicon Drift Detector (SDD) finally the two outermost layers make up the Silicon Strip Detector (SSD), as seen in Fig. 2.2. The primary usage of the subsystem is the reconstruction of primary and secondary vertices with high spatial resolution. It contributes to the full track reconstruction as well as pile-up removal with a momentum resolution of $\sigma_{p_\mathrm{T}}/p_\mathrm{T} \approx 10-12, \%$ [28] for $p_\mathrm{T} < 1$ GeV$/c$. It covers the whole $0 < \phi < 2\pi$ range of the azimuthal angle and pseudo-rapidities of up to $|\eta| < 0.9$ corresponding (by $\eta = -\log(\tan\theta/2)$) to polar angles in the range of $0° < \phi < 135°$ [30]. The ITS is able to identify events with in-bunch pile-up. In this case more than one interaction per bunch-crossing occurs, leading to the reconstruction of two potential primary vertices within one event. Due to the ambiguity of assigning each particle to the correct primary vertex such events are excluded from further analysis. In order to reduce multiple scattering of the produced particles with the detector material, the ITS was build from the lightest materials available, such as carbon-fiber, thus minimizing the material budget. The spatial resolution is on the order of magnitude of 10 µm [30] which is sufficient to deal appropriately with the high multiplicities of around 2000 particles in HI collisions.

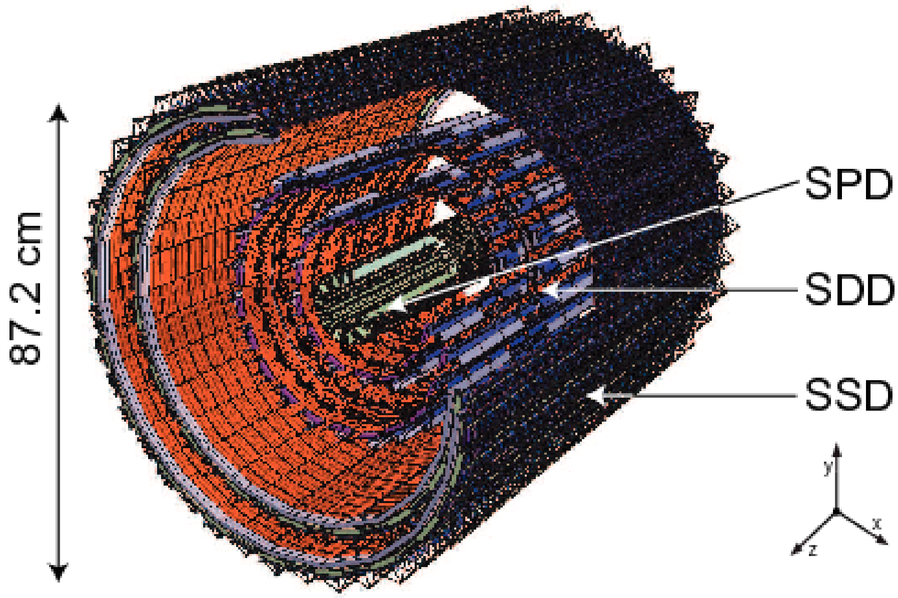

Figure 2.2: Inner tracking system of the ALICE detector, during RUN2, with pointers to the sub-modules taken from [31].

2.2.2 Time Projection Chamber

The Time Projection Chamber (TPC, 3 in Fig. 2.1) [30] is a gaseous detector used for the reconstruction of 3-D tracks and PID by loss of energy for charged particles. This is achieved by exploiting the ionization within the active detector volume caused by the traversing charged particles. The total sensitive volume of the TPC, a schematic is shown in Fig. 2.3, is $90\,\mathrm{m}^3$ with an inner (outer) radius of about 85 (250) cm, extending 500 cm in direction of the beam line. The drift gas changed several times during the data taking, mostly $\mathrm{Ar} - \mathrm{CO}_2$ (88-12 %) was used, as it provided stable conditions and has a desirable low ionization energy. Due to the applied high voltage between central electrode and end-plates ($\Delta U \approx 100\,\mathrm{kV}$), the ionization electrons, liberated by the incident particles from the collision, are drifting to the end-plates for measurement of the x and y coordinates as well as drift time. The drift time of these electrons in the TPC is maximally 100 µm [30]. During this time several LHC bunch crossings and multiple inelastic collision can occur. This leads to so-called out-of-bunch pile-up because not only the particles produced in the triggered event will be recorded, but also particles from events which occurred shortly before and after the triggering. The excellent reconstruction capability of the TPC is related to the 159 radial rows which the particle, depending on its momentum and angle, can traverse before leaving the TPC. This configuration allows to obtain the momentum of the particles with a resolution of $\sigma_{p_\mathrm{T}}/p_\mathrm{T} \approx 5,\%$ [28] for $p_\mathrm{T} < 10\,\mathrm{GeV}/c$ with a full 2π coverage of the azimuthal angle and within pseudo-rapidities of $|\eta| < 0.8$ [30]. For this range the track reconstruction efficiency is expected to be approximately 80 % [30]. The readout of the TPC is optimized to cope with the highest multiplicities in HI collisions and conducted with multi-wire proportional chambers which are located on the endplates of the TPC.

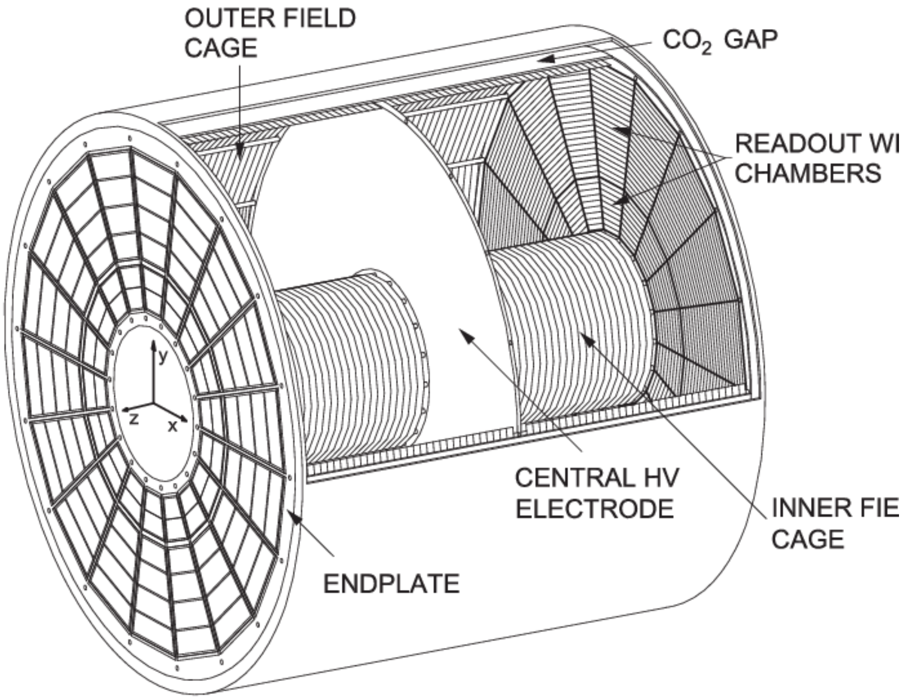

Figure 2.3: Time projection chamber of the ALICE detector, during RUN2, with pointers to the sub-modules taken from [32].

2.2.3 Time Of Flight Detector

With the Time Of Flight (TOF, 5 in Fig. 2.1) [33] the time of flight of the particle is measured allowing to determine the velocity $\beta = v/c$, of the particle. The TOF consists of 1593 glas Multi-gap Resistive Plate Chamber detectors, which in total provide 148149 read-out pads. The coverage of the azimuthal angle as well as the pseudo-rapidities is equivalent to the ranges covered by the TPC. The time resolution of the TOF is around 80 ps [33] which is vital in order to conduct precise PID and enables to remove out-of-bunch pile-up. Measurements of the ITS and TPC are complemented by the TOF, as a rigidity cut-off of $p_{\mathrm{T}} \approx 300\,\mathrm{MeV}/c$ is introduced by the magnetic field and only particles with an exceeding transverse momentum are able to reach the TOF.

2.3 Particle identification

For this work the PID capabilities of the TPC and TOF were used, and hence will be briefly explained. As particles can be differentiated by their corresponding rest mass m_0 particle identification can be realized by measuring β as well as the momentum p of the particle simultaneously. This can be seen by starting from $\beta = (\gamma m_0 v)/(\gamma m_0) = p/E$ and substituting the recovered expression for the energy E of the particle in the relativistic energy-momentum conservation:

$$m_0 = \sqrt{E^2 - p^2} = \sqrt{p^2(1/\beta^2 - 1)} = \frac{p}{\beta\gamma}, \tag{2.1}$$

in which the Lorentz-factor is denoted by $\gamma = 1/\sqrt{1-\beta^2}$, and c is set to unity for convenience.

The energy loss occurring due to ionization, is measured by the TPC and can be described by the Bethe-Bloch (BB) formula given below:

$$-\left\langle \frac{\mathrm{d}E}{\mathrm{d}x} \right\rangle = \frac{4\pi}{m_e c^2} \cdot \frac{n_{\mathrm{mat.}} z^2}{\beta^2} \cdot \left(\frac{e^2}{4\pi\epsilon_0}\right)^2 \cdot \left[\log\left(\frac{2m_e c^2 \beta^2 \gamma^2}{I_{\mathrm{mat.}}}\right) - \beta^2\right], \tag{2.2}$$

which describes the specific mean loss of energy per unit path length due to ionization $-\langle \mathrm{d}E/\mathrm{d}x \rangle$ for a particle with charge z moving with the velocity v in a material with electron density $n_{\mathrm{mat.}}$ and average ionization potential $I_{\mathrm{mat.}}$. It depends on the mass of electrons m_e and the vacuum permittivity ϵ_0. The dependence on $\beta\gamma$ of the BB is equal to a dependence on p/m_0, as can be seen from Eq. (2.1). As long as p is not much larger than m_0, this dependence induces well separated bands depending on the m_0 of the particle, see Fig. 2.5. In order to select the particle of interest the $n\sigma-$identification method can be employed. First the ideal BB curves for several different particle hypotheses are evaluated, by fixing the corresponding masses m_0 for each particle species and solving Eq. 2.2. Then the discrepancy of the measured signal to a certain particle hypothesis is quantified as multiples n of the detector resolution σ_{TPC}. By choosing sufficiently small values for n a reliable identification of the particle in question can be achieved.

For the PID with the TOF the following expression is exploited:

$$m_0 = \sqrt{E^2 - p^2} = \sqrt{p^2(1/\beta^2 - 1)} = p\sqrt{(\Delta t/\Delta x)^2 - 1}, \tag{2.3}$$

in which $\beta = \Delta x/\Delta t$ was used and c was set again to unity. The TOF provides a precise determination of β. Analogous to the case of energy loss, ideal curves for the β pertaining to certain particle hypotheses can be obtained by solving Eq. (2.3) (see Fig. 2.5) and the $n\sigma-$identification method can be applied again. Additionally, if the PID information of both the TPC and TOF detectors needs to be combined, the $n\sigma-$identification method can be used on the trivially combined resolution according to

$$\sigma_{\mathrm{comb.}} = \sqrt{\sigma^2_{\mathrm{TPC}} + \sigma^2_{\mathrm{TOF}}}. \tag{2.4}$$

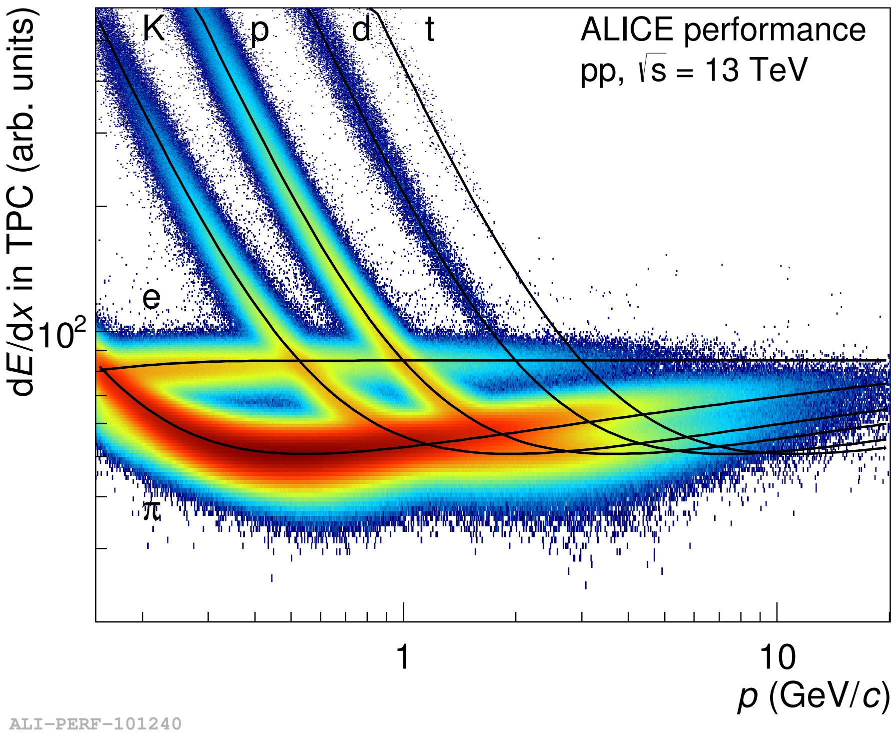

Figure 2.4: Specific mean loss of energy per unit path length, within the TPC, depending on the momentum p. For several particle hypotheses the ideal Bethe-Bloch curves are drawn, taken from [34].

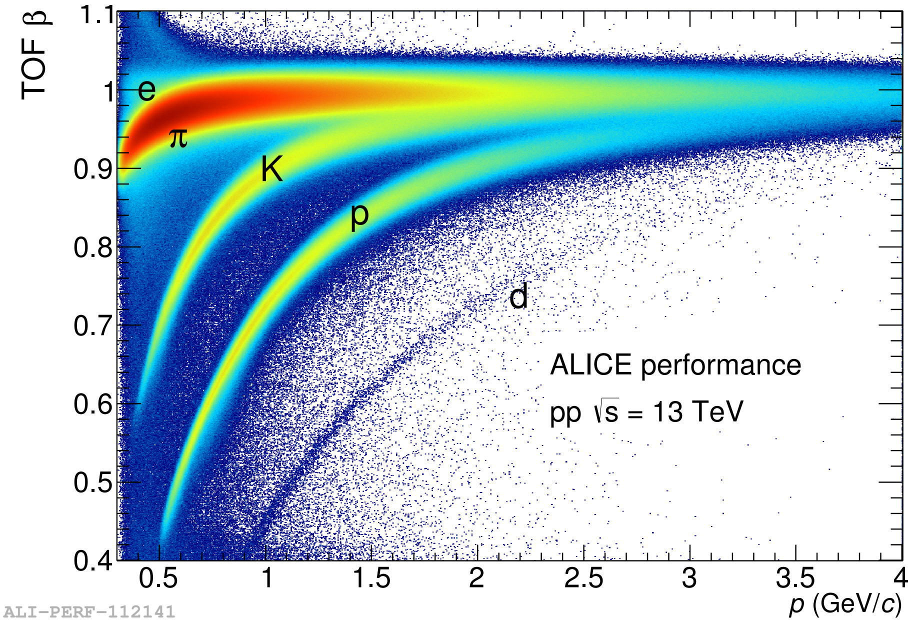

Figure 2.5: Distribution of β, measured with TOF, depending on the momentum p. For several particle hypotheses the ideal β curves are drawn, taken from [35].

Chapter 3

Data Analysis

The purpose of this chapter is to provide basic information about the analysed data sample as well as an explanation how the identification of charged pion tracks within the studied sample was achieved.

3.1 Data sample and event selection

The input data for the analysis consists of the pp collision data sample collected at $\sqrt{s}$ = 13 TeV by ALICE, using the minimum bias trigger (`AliVEvent::kINT7()`), during the LHC Run 2 campaign. In order to process only events, which have all the necessary information, the pre-filtered Analysis Object Data (AOD)[1] format was used. Additionally general purpose Monte Carlo simulations of events, which were filtered through the ALICE detector, tuned to the conditions during the LHC Run2 campaign, and the reconstruction algorithm [36], were used. These were generated with Pythia 8.1 [37].

Not every event can be used for analysis, especially in the case the post-processing of the data reveal unsatisfying quality or if the event is not suitable for physics analyses e.g. if the primary vertex is not centered around the nominal interaction point. In order to assure the quality of the processed events the event cuts summarized in Tab. 3.1 were employed. The Physics selection is needed in order to access the PID information of the sub-detector systems. If the Data Acquisition (DAQ) [38] for the event is incomplete, the event is discarded. For the pile-up rejection the SPD (which is a part of the ITS) detector is used and a minimum resolution of 0.25 cm for the z position of the primary vertex is required. Finally the z coordinate of the primary vertex is checked to be within 10 cm of the nominal interaction point. This selection guarantees a uniform detector acceptance for all processed events.

The impact of mini-jet background on the correlation function was already explored in several studies [9, 39]. This lead to the introduction of event shape variables [40], that allow to differentiate between events which are either dominated by soft or hard processes leading to a categorisation of jet-like and spherical events. For this analysis the same approach is adopted, hence, in order to select predominantly spherical events, the transverse sphericity cut is employed [41]. The transverse momentum matrix $\boldsymbol{S_T}$ is defined by

$$\boldsymbol{S_T} = \frac{1}{\sum_i p_T^i} \sum_i \frac{1}{p_T^i} \begin{pmatrix} (p_x^i)^2 & p_x^i \cdot p_y^i \\ p_x^i \cdot p_y^i & (p_y^i)^2 \end{pmatrix} \text{ with eigenvalues } \lambda_1, \lambda_2, \tag{3.1}$$

[1]Usually after data taking so-called Event Summary Data (ESD) are generated, however not every analysis requires the complete saved event information.

Selection criterion	Value
Trigger	`AliVEvent::kINT7()`
Spericity	S_T >0.7
Physics selection	default
Incomplete DAQ	check
z primary vertex	$\lvert vtx_z\rvert$<10 cm
Contributors to track vertex	$N_{\mathrm{contrib,track}}$ >1
Contributors to SPD vertex	$N_{\mathrm{contrib,SPD}}$>0
Distance between track and SPD vertex	$d_{\mathrm{vtx,track-SPD}}$<0.5 cm
SPD vertex z resolution	$\sigma_{\mathrm{SPD},\,z}$<0.25 cm
Pile-up rejection	`AliVEvent::IsPileUpFromSPD()` `AliEventUtils::IsSPDClusterVsTrackletBG()`

Table 3.1: Event selection criteria.

where $p_{\mathrm{T}}^i = \sqrt{(p_x^i)^2 + (p_y^i)^2}$ is the transverse momentum of a single particle. By calculating the corresponding eigenvalues (λ_1, λ_2) of the matrix and combining them to build S_T as

$$S_T = \frac{2min(\lambda_1, \lambda_2)}{\lambda_1 + \lambda_2}, \tag{3.2}$$

the geometry of the event, meaning the degree of isotropic emission, can be estimated. In order to calculate the transverse sphericity with good accuracy at least three tracks, each with a minimum p_{T} of 0.5 MeV/c, are required, else the event is discarded. Commonly the threshold for jet-like events is $S_T < 0.3$, whereas $S_T > 0.7$ is required for the spherical event classification [41]. In this work, to suppress the mini-jet background, only events with $S_T > 0.7$ have been selected. After the event selection around 2.4×10^8 events are available for further analysis.

3.2 Identification of charged pion tracks

A summary of all applied track cuts, which are employed to select primary charged pions, is compiled in Table 3.2. In addition, a cut for the close pair rejection (CPR) is included, the necessity of which is explained during the discussion of the detector effects in sec. 5.1. The quality of the tracks is ensured by requiring that each track lies within the pseudo-rapidity range of $|\eta| < 0.8$ while also demanding that a minimum of 75 clusters in the Time Projection Chamber (TPC) are assigned to each track. In order to suppress contributions stemming from weakly decaying resonances, a cut of 0.3 cm on the distance of closest approach (DCA) to the primary vertex, in the transverse x–y plane as well as of 0.1 cm along the beam axis in z direction, is used. The particle identification (PID) is conducted by the measurement of the mean energy loss per distance travelled $\langle \mathrm{d}E/\mathrm{d}x \rangle$ within the TPC and the velocity measurement provided by the Time Of Flight detector (TOF). In combination with a momentum measurement, which is possible due to the magnetic field permeating the detector, different mass hypotheses can be tested (see sec. 2.3). For this analysis the deviation of the measured TPC response to the Bethe-Bloch parameterization of $\langle \mathrm{d}E/\mathrm{d}x \rangle$ for the mass hypothesis of a charged pion, is expressed as multiples of the standard deviation nσ and only those tracks which satisfy $|n_{\sigma,\mathrm{TPC}}| < 3$ for $p < 0.5$ GeV/c are taken, as the $\langle \mathrm{d}E/\mathrm{d}x \rangle$ of the charged pions is well separated from other particle species. In the momentum range

Selection criterion	Value
Pseudorapidity	$\lvert\eta\rvert < 0.8$
Transverse momentum	$0.14 < p_{\mathrm{T}} < 4\,\mathrm{GeV}/c$
TPC cluster	$n_{\mathrm{TPC}} > 75$
Distance of closest approach xy	$\lvert\mathrm{DCA}_{xy}\rvert < 0.3\,\mathrm{cm}$
Distance of closest approach z	$\lvert\mathrm{DCA}_{z}\rvert < 0.3\,\mathrm{cm}$
Close pair rejection	$\sqrt{\Delta\eta^2 + \Delta\phi^{*2}} < 0.01$
Particle identification	$\lvert n_{\sigma,\mathrm{TPC}}\rvert < 3$ for $p < 0.5\,\mathrm{GeV}/c$ $n_{\sigma,\mathrm{combined}} < 3$ for $p > 0.5\,\mathrm{GeV}/c$

Table 3.2: Charged pion track selection criteria.

$p > 0.5$ GeV/c the pion band of the TPC is contaminated by particles of other species, hence up to $p < 4$ GeV/c also the TOF information is used. The difference between the measured TOF response and the velocity calculated for a charged pion as a function of the pions momentum is expressed as $n_{\sigma,\mathrm{TOF}}$, and combined with the TPC information into a combined $n_{\sigma,\mathrm{combined}} = \sqrt{n^2_{\sigma,\mathrm{TPC}} + n^2_{\sigma,\mathrm{TOF}}}$. The results of the PID cuts are shown in Fig. 3.1 for the TPC and TOF, the obtained p_{T}-spectra for the charged pions are shown in Fig. 3.2. The nσ distributions show clearly that most of the charged pion yield is concentrated at $p_{\mathrm{T}} < 0.5$ GeV/c, the visible structure comes from using the combined PID of TPC and TOF for $p > 0.5$ GeV/c. And is related to the degraded detector efficiency at $p > 0.5$ GeV/c, as the tracks must extend from the TPC to the TOF. As expected the shape of the p_{T}-spectra does not depend on the charge of the selected charged pion. In total around 1.15×10^9 positively (negatively) charged pions were identified. The purity of the charged pion sample is studied with the help of Monte Carlo simulations (see sec. 4.2) and the p_{T} weighted is determined to be 99 % independent of the charge. The tracking efficiency for charged pions was not evaluated in this work, however, studies carried out by the Light Flavour Spectra group within ALICE found that for $0.14 < p_{\mathrm{T}} < 4$ GeV/c the value is typically around 0.62 and increases up to 0.68 [42].

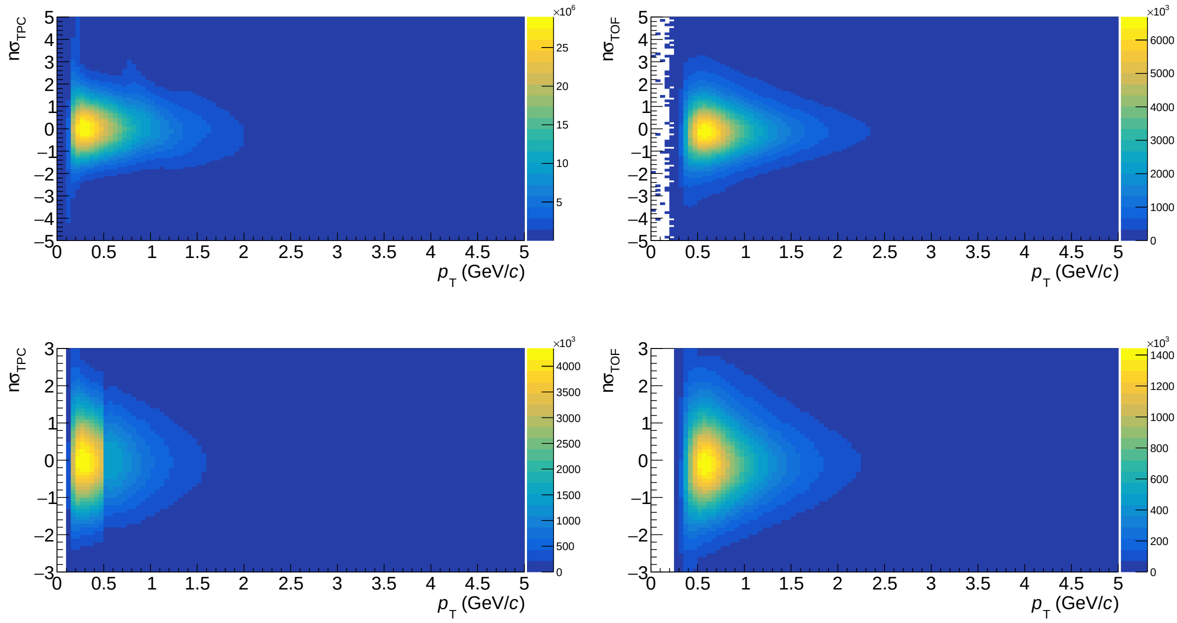

Figure 3.1: Experimental nσ before the application of the PID cuts (upper row) and nσ (lower row) after applied PID cuts. The structure of the plot in the lower row on the left comes from the fact that in addition to TPC the TOF information is used for $p > 0.5\,\mathrm{GeV}/c$.

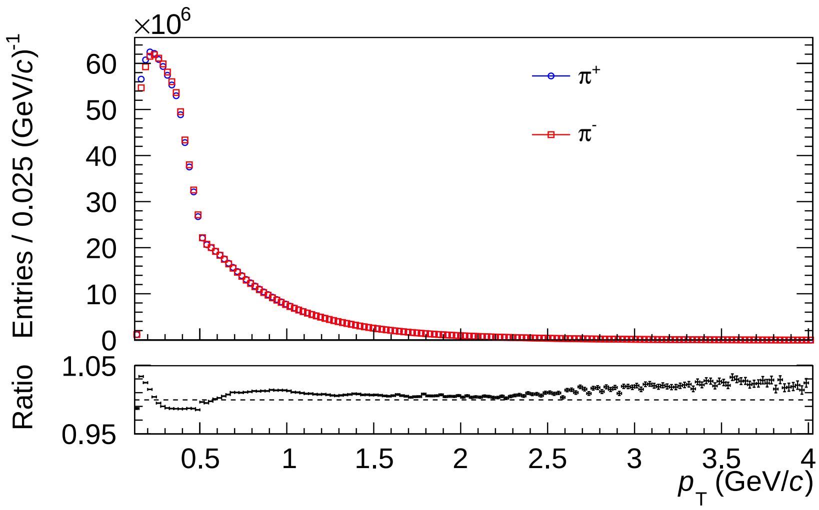

Figure 3.2: Experimental p_T-distributions of π^+ (π^-) in red (blue) after the application of the event and track cuts. The change of slope at $p > 0.5\,\mathrm{GeV}/c$ in the spectrum is caused by using the combined PID of TPC and TOF. The bottom panel shows the ratio of the two spectra.

Chapter 4

Study of the resonance feed-down

Charged pions are very light particles ($m_{\pi^{\pm}} \approx 139.57$ MeV/c[1]), hence they are abundantly produced by the strong decay of unstable heavier resonances. The feed-down to charged pions stemming from strong decays typically leads to a large enhancement at low transverse momenta in the measured p_{T} spectra. Previous studies [8, 43] demonstrated that the correlation functions as measured at ALICE in pp collisions are sensitive to several kinds of residual correlation signals. Contributions from strongly decaying resonances feeding to one or both particles in the measured pair can modify the source, depending on the lifetime (τ) of the resonance. Accounting for this kind of contributions is crucial, otherwise a bias of the apparent source size is introduced [44–46]. In total three origins of charged pions need to be taken into account: primordial pions, pions stemming from strong decays, and finally pions produced by weak decays. In the context of this work the term primordial will refer to charged pions originating from the initial collision. The particles produced by a weak decay typically reduce the measured correlation signal and can be accounted for by the λ-parameter prescription [43]. Special emphasis will be laid on quantifying the yield of the charged pions stemming from strong decays as the novelty in this study is the approach to fix this specific contribution using the statistical hadronization model to determine the yields of resonances and a transport model, namely EPOS [25], to constrain the decay kinematics. Following this approach the modification of the source, by strongly decaying resonances, is properly taken into account. This is an extension to the search of a common particle source, previously studied in baryon-baryon analyses [8, 11–13], to the meson-meson sector.

4.1 Composition of the strong decay component according to the statistical hadronization model

In order to assess the amount of primordial charged pions present in the yield of primary charged pions, the statistical hadronization model is employed. The definition of primary particles used is mostly in line with ALICE standards [47], including all particles which are either produced by the initial collision or originate from a short lived ($c\tau_{\mathrm{res}} < 1\,\mathrm{fm}$) strong or electromagnetic decay. For this study additionally every charged pion stemming from strongly decaying resonance, regardless of the lifetime, is considered primary. Details on this will be given later (see sec. 5.2). The Thermal-FIST package [24] is used to estimate the particle yields by means of calculations within the hadron resonance gas (HRG) model.

A brief summary of the important key aspects regarding the HRG model is presented in the following. Within the canonical statistical model an ideal (non interacting) gas of hadrons is assumed, which are emitted from a thermally and chemically equilibrated source. Under this assumption the canonical

[1]Value taken from the Particle Data Group summary tables.

ensemble can be employed to describe small sources, as is the case for pp collisions. Considering three conserved charges, the baryon-number B, the electric-charge Q and the strangeness S, which are exactly conserved within the correlation volume V_c, the partition function reads [24]

$$\mathcal{Z}(B,Q,S) = \int_{-\pi}^{\pi} \frac{\mathrm{d}\phi_B}{2\pi} \int_{-\pi}^{\pi} \frac{\mathrm{d}\phi_Q}{2\pi} \int_{-\pi}^{\pi} \frac{\mathrm{d}\phi_S}{2\pi} e^{-i(B\phi_B + Q\phi_Q + S\phi_S)} \times \exp\left[\sum_j \sum_{n=1}^{\infty} z_j^n e^{in(B_j\phi_B + Q_j\phi_Q + S_j\phi_S)}\right]. \tag{4.1}$$

The first sum over j includes the considered particle species while the last sum over n incorporates the effects of quantum statistics. The charges of particle species j are denoted by B_j, Q_j and S_j, while z_j^n refers to the corresponding single species partition function, namely,

$$z_j^n = (\mp 1)^{(n-1)} V_\mathrm{c} \int \mathrm{d}m\ \rho_j(m)\ d_j \frac{m^2 T}{2\pi^2 n^2}\ K_2\left(\frac{nm}{T}\right), \tag{4.2}$$

where the spin degeneracy (temperature) is denoted by d_j (T) and the +/- sign is used for bosons/fermions. The finite width of the particles is taken into account by considering a relativistic Breit-Wigner function $\rho_j(m)$. $K_2(nm/T)$ is a second order modified Bessel function. Finally the mean primary particle multiplicities can be calculated[2], resulting in

$$\langle N_j^{\text{prim.}} \rangle = \sum_{n=1}^{\infty} \frac{Z(B - nB_j, Q - nQ_j, S - nS_j)}{Z(B,Q,S)} n z_j^n, \tag{4.3}$$

which can be corrected by feed-down contributions to give the total expected yield of particle species j, namely $\langle N_j^{\text{total}} \rangle$. Details of the calculation are given in [48]. The performance of the model can be judged by inspecting Fig. 4.1 [49]. Shown are hadron-to-pion yield ratios as a function of the charged particle multiplicity at mid-rapidities, overall the data agrees well with the model predictions.

Before usage Thermal-FIST must be properly configured in order to provide reliable results. For the calculation the canonical ensemble was chosen, due to the small expected source sizes on the order of 1 fm. The appropriate quantum statistics was set to apply to all particles, which is especially important for the pions. The conserved abelian charges correspond to B, Q and S and the width of the resonances are modeled with relativistic energy dependant Breit-Wigner distributions. Finally, the temperature T, the canonical strangeness (flavour) suppression factor γ_S (γ_q) and the source (correlated) radius R (R_c) must be configured. The strangeness suppression factor is used in order to describe the suppressed production of strange hadrons observed in pp collisions [17]. Thermal-FIST additionally offers the option to consider a suppression factor γ_q for light flavours, but in this work no such suppression was considered. The total (correlated) volume V (V_c) is assumed to be a sphere with radius R (R_c). Within the correlated volume the exact conservation of B, Q and S is enforced.

The calculation of the parameters is performed as described in [49], however, fine tuned to match the 13 TeV pp environment, by using the information in [50] about the average multiplicity at mid-rapidities of $|y| < 0.5$. A compilation of the parameters used to perform the calculations with Thermal-FIST is shown in Tab. 4.1. Finally Thermal-FIST was configured to include all particles with their decay channels and associated branching ratios listed in the Particle Data Groups summary tables.

[2] For this computation so-called fictitious fugacities λ_j are introduced to the partition function given in Eq. (4.1) and the derivative with respect to λ_j is calculated: $\langle N_j^{\text{prim.}} \rangle = \partial_{\lambda_j} \log \mathcal{Z}(\lambda_j)\big|_{\lambda_j = 1}$.

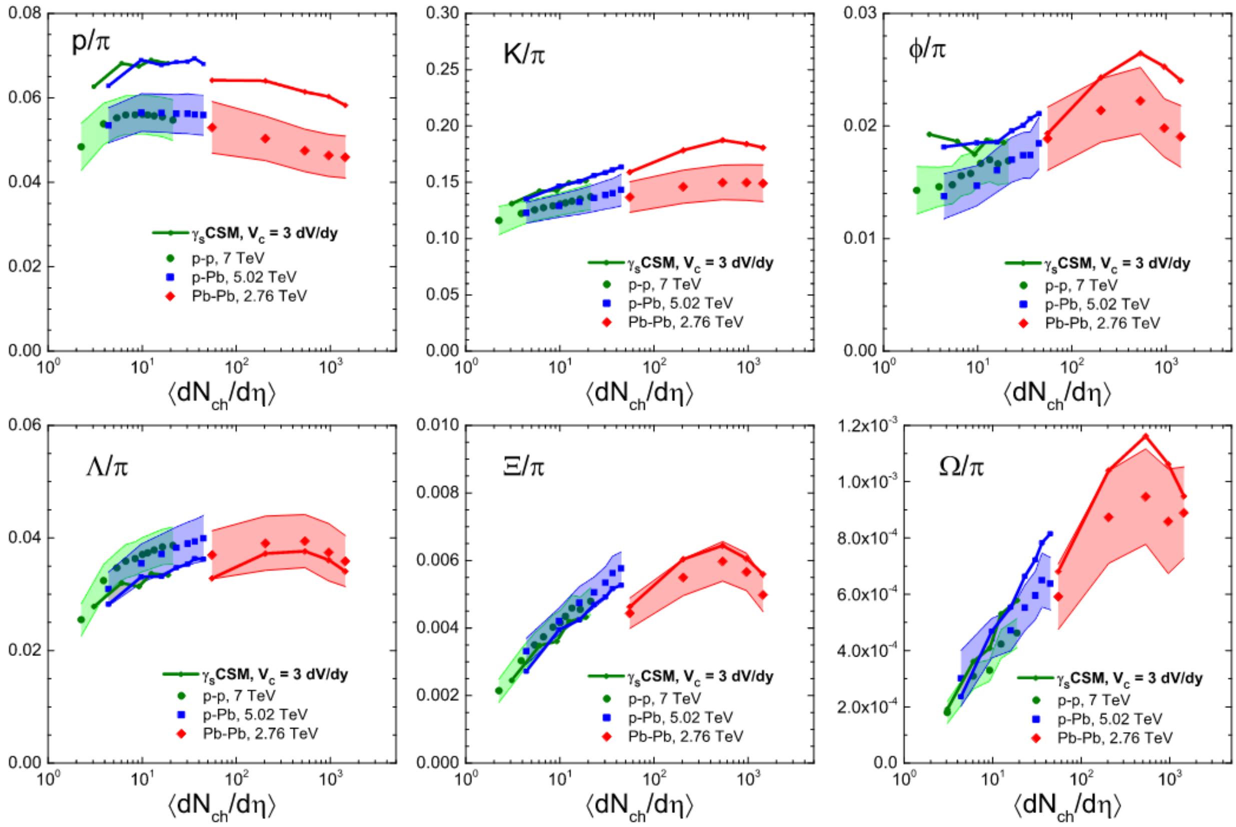

Figure 4.1: The ratios of various final hadron-to-pion yields are plotted versus charged the pion multiplicity as evaluated in the γ_SCSM with $V_c = 3dV/dy$, exact conservation of baryon number, electric charge, and incomplete equilibration of strangeness. The green circles, blue squares, and red diamonds depict the corresponding ratios as measured by the ALICE collaboration at the LHC in pp (7 TeV), p–Pb (5.02 TeV), and Pb–Pb (2.76 TeV) collisions, respectively. Taken from [49].

Ideal HRG model specifications	used
Ensemble	Canonical
Statistics	Quantum statistics for all particles
Resonance width	E dependent Breit-Wigner distr.
Breit-Wigner shape	Relativistic
Conservation laws	Canonical treatment of Baryon number (B), Charge (Q) and Strangeness (S)
Parameter	**Value**
Temperature (MeV)	171.0
Strangeness suppression factor	$\gamma_S = 0.78$
Flavour suppression factor	$\gamma_q = 1.0$
Source radius for one unit of rapidity (fm)	$R = 1.58$
Canonical correlated radius (fm)	$R_c = 2.28$
B, Q, S	0

Table 4.1: Model specifications and values of parameters used for the yield calculations.

Resonances	$c\tau_{\mathrm{res}}$ (fm)	Fraction (%)
ρ^0	1.3	9.01
ρ^+	1.3	8.71
$\omega(782)$	23.4	7.67
K*(892)+	3.9	2.29
$\bar{\mathrm{K}}$*(892)0	3.9	2.25
b1(1235)+	1.4	1.90
a2(1320)+	1.8	1.48
η	150 631.3	1.45
a1(1260)+	0.5	1.37
f2(1270)	1.1	1.36
a0(980)+	2.6	1.36
h1(1170)	0.5	1.18

Table 4.2: Resonances contributing at least 1 % to the charged pion yield, stemming from strong and electro-magnetic decays.

Lifetime $c\tau$ (fm)	Fraction $\mathcal{F}$ (%)	$\langle m_{\mathrm{res}}^{\mathrm{eff}} \rangle$ (GeV/c)
Primordial	28.0	–
$c\tau_{\mathrm{res}} < 1$	14.8	0.308
$1 < c\tau_{\mathrm{res}} < 2$	34.8	0.526
$2 < c\tau_{\mathrm{res}} < 5$	10.2	0.151
$c\tau_{\mathrm{res}} > 5$	12.2	0.146

Table 4.3: Lifetime table for the charged pion yield.

The result for the composition of the yield of primary charged pions ($\pi_{primary}$) contains every contribution to the charged pion production from the initial pp collision, via an electro-magnetic decay or strongly decaying resonances, regardless of the lifetime. In total 334 resonances were found to contribute to the yield of $\pi_{primary}$. The origin of $\pi_{primary}$ for all resonances which feed at least 1 % to the overall yield is shown in Tab. 4.2 together with their corresponding lifetime $c\tau_{\mathrm{res}}$. Approximately 25 % of the yield comes from the combined contributions of ρ^0, ρ^+ and $\omega(782)$. Differential information about the lifetimes of the resonances feeding into the yield is provided in Tab. 4.3 together with the fraction weighted averaged mass for the resonances within the lifetime bin. It is evident that while most contributions are rather short lived ($c\tau_{\mathrm{res}} < 5\,\mathrm{fm}$), a sizeable 12.2 % of all contributions to $\pi_{primary}$ have a $c\tau_{\mathrm{res}} > 5\,\mathrm{fm}$.

The two key parameters which drive the modification of the particle emitting source stemming from resonances are the average effective mass $\langle m_{\mathrm{res}}^{\mathrm{eff}} \rangle$ and the average effective proper lifetime $\langle c\tau_{\mathrm{res}}^{\mathrm{eff}} \rangle$. Both quantities are calculated according to

$$\langle \mathcal{X}_{\mathrm{res}}^{\mathrm{eff}} \rangle = \frac{1}{\alpha} \left[\sum_j f_j \mathcal{X}_j \right] , \tag{4.4}$$

by taking the weighted average of each respective quantity $\mathcal{X}$, where the weight f is given by contribution of the resonance j to the yield. For the calculation it is important to exclude resonances with $c\tau_{\mathrm{res}} > 5\,\mathrm{fm}$ e.g. $\omega(782)$ ($c\tau_{\mathrm{res}} = 23\,\mathrm{fm}$), since it is expected that such long-lived resonances[3] produce an exclusively

[3]The details how these are treated are explained in sec. 5.2.

flat contribution to the correlation function. Consequently the contributions predicted by Thermal-FIST must be re-normalized by a factor of $\alpha = \left(1 - \mathcal{F}_{c\tau_{\mathrm{res}}} > 5\,\mathrm{fm}\right)$, where $\mathcal{F}_{c\tau_{\mathrm{res}}} > 5\,\mathrm{fm}$ denotes the fraction of strongly decaying resonances with $c\tau_{\mathrm{res}} > 5\,\mathrm{fm}$ and is equal to 12.2 %. The obtained results are $\langle m_{\mathrm{res}}^{\mathrm{eff}} \rangle = 1.124\,\mathrm{GeV}/c$ and $\langle c\tau_{\mathrm{res}}^{\mathrm{eff}} \rangle = 1.5\,\mathrm{fm}$.

4.2 Constraining the weak feed-down by DCA_{xy} fits to MC simulations

The contribution to the correlation function related to charged pions stemming from the feed-down of weakly decaying resonances is evaluated in a data-driven manner and explained in the following.

Particles with this type of origin are referred to as secondary particles, hence this contribution is denoted as $\pi_{secondary}$. The ALICE collaboration has general purpose Monte Carlo (MC) simulations, which were generated using Pythia 8.1 [37]. They are filtered to include a full simulation of the detector response using GEANT4 [51], and are further treated as experimental data by the track reconstruction algorithm [36]. In this way the final output contains both the detected signal and the original (true) MC information. This enables to trace back the origin of each simulated pion, e.g. whether it is of primary origin, stemming from feed-down or from the interactions with the detector material.

To reduce the model-dependence on the extraction of $\pi_{secondary}$, an appropriate method is to use the MC to generate template fits to the DCA_{xy}[4] distribution of the charged pions, based on their origin. The MC generated templates are fitted to the experimental DCA_{xy} distribution to extract the amount of primary and secondary particles. This procedure is required as neither Pythia 8.1 nor other MC generators are tuned to reproduce the yield of the particles. In order to study the contribution differentially in p_{T}, the MC templates and experimental DCA_{xy} distributions are obtained for the following p_{T}-bins[5] 0.1–0.9, 0.9–1.7, 1.7–2.5, 2.5–3.2, 3.2–4.0 GeV/c, by using the same cuts as for the anaylsis of data (see Tab. 3.2) but imposing no cut on $|\mathrm{DCA}_{xy}|$. The considered contributions are $\mathrm{K}^0_{\mathrm{S}}$, K^+, Λ and Σ^0 combined (since their respective DCA_{xy} is indistinguishable in the MC templates), Σ^+ and $\overline{\Sigma}^-$, these are shown exemplary in Fig. 4.3 and Fig. 4.4 for π^+ and π^- respectively. All templates are centered around $|\mathrm{DCA}_{xy}| = 0\,\mathrm{cm}$ and show a peak, mostly related to the red primary template. The reason to apply no $|\mathrm{DCA}_{xy}|$ cut becomes apparent by inspecting the region of $|\mathrm{DCA}_{xy}| > 0.5\,\mathrm{cm}$ in Fig. 4.3 and Fig. 4.4, as by widening the range the difference in the shape of the tails of the templates can be used to estimate the total contribution to the experimental DCA_{xy} distribution. The remaining fits are presented in the appendix B. The reduced χ^2 divided by the numbers of degree of freedom for Fig. 4.3 and Fig. 4.4 are 5.1 and 5.2 respectively. These values are calculated only in approximation by calculating the reduced χ^2 for the complete fit with respect to the data and hence is most certaintly an overestimation. The reduced χ^2 given by the TFractionFitter class of ROOT could not be used due to a falsely implemented calculation method, the issue is reported in [52] and is the reason why in the case of a domineering template the program returns reduced χ^2 values of $\mathcal{O}(1000) - \mathcal{O}(10000)$.

For each p_{T}-bin a fit was performed using the TFractionFitter class of ROOT, however, instead of leaving all the weights of the templates free, initial values for the relative contributions were obtained from Thermal-FIST, which was tuned according to Tab. 4.1. The raw Thermal-FIST output is corrected by the branching ratios of the mother particles for the decay into a charged pion. The summary Table 4.4 provides an overview of the Thermal-FIST predicted fractions f_j, normalized to the positively charged

[4] DCA_{xy}: Distance of closest approach form the reconstructed particle track to the primary vertex in the transverse plane.

[5] The upper edge is always included in the bin.

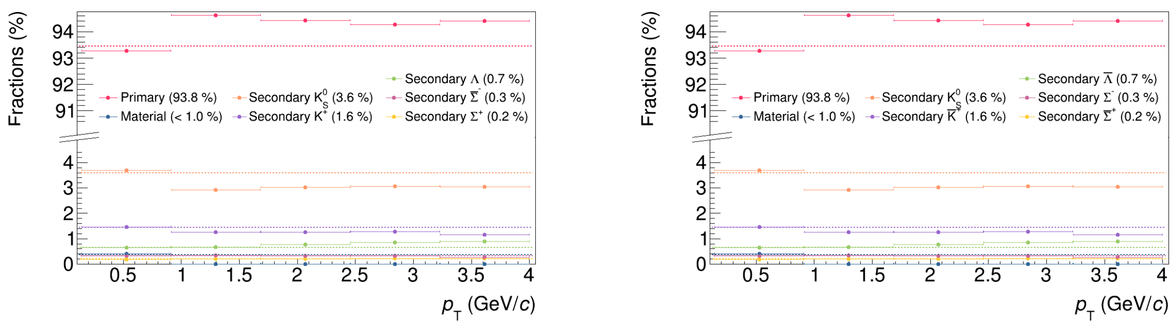

Figure 4.2: *Left:* The percentage of the contribution from $\pi_{primary}$, $\pi_{secondary}$ and positively charged pions stemming from the interaction with the detector material, which is seen to be below 1 %, are shown. The dotted lines correspond to the averaged p_T weighted value of all the p_T-bins. *Right:* The same decomposition of the negatively charged pions is displayed. For both the ordering of the feed-down contributions is consistent with the estimation from Thermal-FIST.

pion yield $N_{\mathrm{tot}}^{\pi^+}$, and the weights ω_j calculated for every source of $\pi_{secondary}$. The contributions due to decays into three charged pions were found to be negligible and are hence not listed. The resulting fractions of the fits are summarized in Fig. 4.2 and shown for positively and negatively charged pions. As the extraced fractions show, the sample is dominated by primary particles, however, around 6-7 % of pions stem from a weakly decaying resonance. Within the studied p_T resolution all considered contributions exhibit no dependence on the p_T.

Finally the extracted values for the fractions are averaged over p_T within the applied selection criterion of $|\mathrm{DCA}_{xy}| < 0.3\,\mathrm{cm}$ and weighted using the measured yield $\mathrm{d}N_{\mathrm{ch}}/\mathrm{d}p_T$ (see. Fig. 3.2), in each individual bin. The final averaged and weighted results are shown in Table 4.5, alongside with a comparison to the prediction of the Thermal-FIST model calculations. As expected the absolute values are different, but the relative ordering of the contributions matches the Thermal-FIST prediction.

In addition, the amount of misidentified (misid) charged pions can be determined from MC, by calculating the p_T dependent purity. The purity $\mathcal{P}$ is obtained by using the following relation

$$\mathcal{P} = \frac{Y_{\mathrm{identified}}^{\mathrm{MC-true}}}{Y_{\mathrm{identified}}}, \tag{4.5}$$

where $Y_{\mathrm{identified}}$ refers to the yield of particles identified as charged pions, applying the same event and track selection as to data, and $Y_{\mathrm{identified}}^{\mathrm{MC-true}}$ denotes the yield of particles for which additionally the PID is verified by accessing the MC information. The dropping of the purity within the first 5 bins is due to a contamination of electrons (positrons). However, comparing the yield in Fig. 3.2 within these bins shows that only the first bin, which contains nearly one order of magnitude less yield then the other bins, is affected. The extracted purity as a function of p_T is shown in Fig. 4.5 and yields a p_T weighted value of 99 % for both π^+ and π^-. The presented result is for π^+.

Table for π^+ [%]	π^+	K^0_s	K^+	$\Lambda+\Sigma^0$	Σ^+	$\overline{\Sigma}^-$
Total frac.: $f^j_{\mathrm{tot}} = N^j_{\mathrm{tot}}/N^{\pi^+}_{\mathrm{tot}}$	100	12.3	12.6	2.8	0.8	0.8
Prim. frac.: $f^{\pi^+}_{\mathrm{prim}} = N^{\pi^+}_{\mathrm{prim}}/f^{\pi^+}_{\mathrm{tot}}$	87.8	-	-	-	-	-
Branching ratios (B.R.)	-	69.20	22.43	64.09	48.31	99.85
$f^{j\to\pi^+}_{\mathrm{sec}} = B.R._j \times f^j_{\mathrm{tot}}$	-	8.5	2.8	1.8	0.4	0.8
$\omega_j = \mathcal{N} \times f^{j\to\pi^+}_{\mathrm{sec}}$	-	7.3	2.4	1.5	0.4	0.6

Table 4.4: Estimation of the weights for each MC template. Since the electro-magnetic decay of $\Sigma^0 \to \Lambda\gamma$ is very fast it is included in the template for Λ. The normalisation $\mathcal{N}$ ensures that the sum of the weights is equal to unity. The table for negatively charged pions can be derived by taking the corresponding antiparticles in the first row, since the numbers as well as their calculation do not differ with respect to the positively charged pions.

Origin	TF [%]	DCA [%]
$\omega_{\pi^+_{primary}}$	87.8	93.8
$\omega_{K^0_s}$	7.3	3.6
ω_{K^+}	2.4	1.5
$\omega_{\Lambda+\Sigma^0}$	1.5	0.7
$\omega_{\overline{\Sigma}^-}$	0.6	0.3
ω_{Σ^+}	0.4	0.2

Table 4.5: Compilation of the possible origin for the π^+. The first column shows the prediction from Thermal-FIST, while the second column is the p_{T} averaged and $\mathrm{d}N_{\mathrm{ch}}/\mathrm{d}p_{\mathrm{T}}$ weighted fit result of the MC DCA templates to the experimental data.

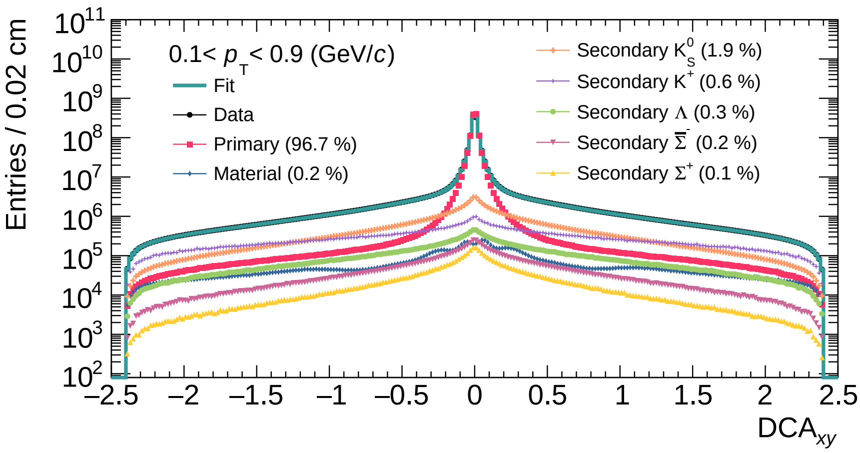

Figure 4.3: DCA fit of π^+ with MC templates using the TFractionFitter. For the smallest p_{T}-bin. Shown is the full fit in the region of [-2.4, 2.4] due to the difference in shape of the templates the single contributions can be separated. The template of Λ entails the contributions of Σ^0.

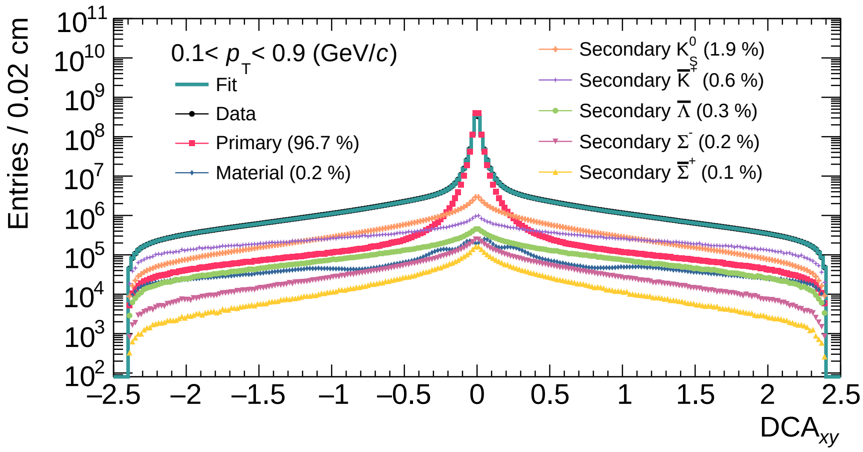

Figure 4.4: DCA fit of π^- with MC templates using the TFractionFitter. For the smallest p_{T}-bin. Shown is the full fit in the region of [-2.4, 2.4] due to the difference in shape of the templates the single contributions can be separated. The template of Λ entails the contributions of Σ^0.

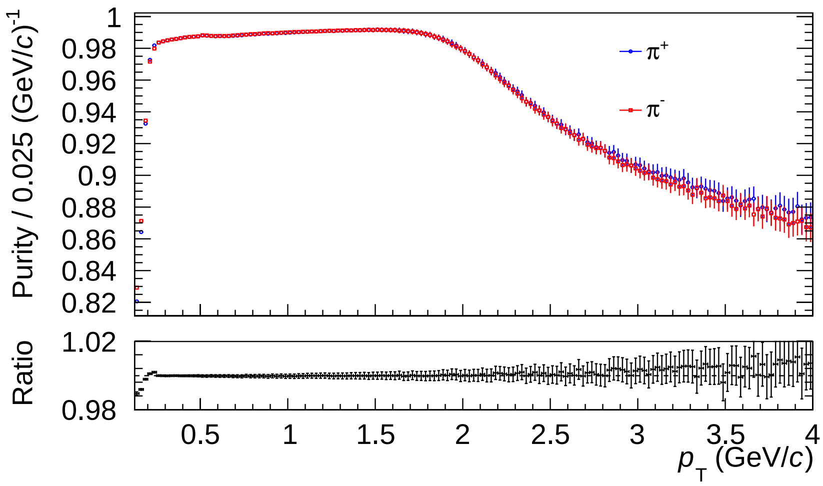

Figure 4.5: Purities of the charged pions determined from MC simulations. With π^- on the left and π^+ on the right, as a function of p_{T}.

Chapter 5

Femtoscopic analysis

This chapter describes how the same charge pion correlation functions were modeled and puts special emphasis on the applied corrections as well as giving details about the source treatment.

5.1 Detector effects

5.1.1 Finite momentum resolution

Although ALICE has excellent tracking capabilities the momentum resolution for the measured particles can impact the shape of the theoretical correlation function fitted to the data. However, by applying momentum smearing at the level of the correlation function this effect can be accurately taken into account. In order to quantitatively model this effect MC studies based on Pythia 8.1 are employed [53–55].

The momentum smearing is primarily related to the single particle detection. However, since the correlation is studied in terms of the relative momentum k^*, one needs to study the probability of measuring k^*_{meas} given the true momentum k^*_{true}. This information is commonly embedded in a transformation matrix $T(k^*_{\mathrm{meas}}, k^*_{\mathrm{true}})$, which can be obtained by making use of the available general purpose MC simulations. Finally, the numerically generated detector signal is used to generate MC tracks, by treating the simulated data as experimental one and following the procedures described in sec. 3.2. This allows to build same- and mixed-event particle pairs, as well as the correlation function. The true correlation function $C(k^*_{\mathrm{true}})$ is transformed by the relation

$$C(k^*_{\mathrm{true}}) = \int\limits_{k^*_{\mathrm{meas}}} T(k^*_{\mathrm{meas}}, k^*_{\mathrm{true}}) * C(k^*_{\mathrm{meas}}). \tag{5.1}$$

The formula given in Eq. (5.1) needs to be adapted in the case of binned data, replacing the integration with a summation over the single k^*_{meas}-bins. In Fig. 5.1 the unnormalized smearing matrix for the same event in case of π^+–π^+ is shown. The response of the detector is approximately linear and relatively narrow, resulting in only minor corrections to the overall shape of the correlation function. The smearing matrix obtained from the same event of π^-–π^- was found to be in very good agreement compared to the one obtained for π^+–π^+, hence all correlation functions were smeared with the smearing matrix of π^+–π^+.

5.1.2 Finite track resolution

In the case of highly correlated pairs of particles, the momenta are nearly collinear and correspondingly carry a very small k^*. While these pairs are the most interesting to analyze, the track reconstruction

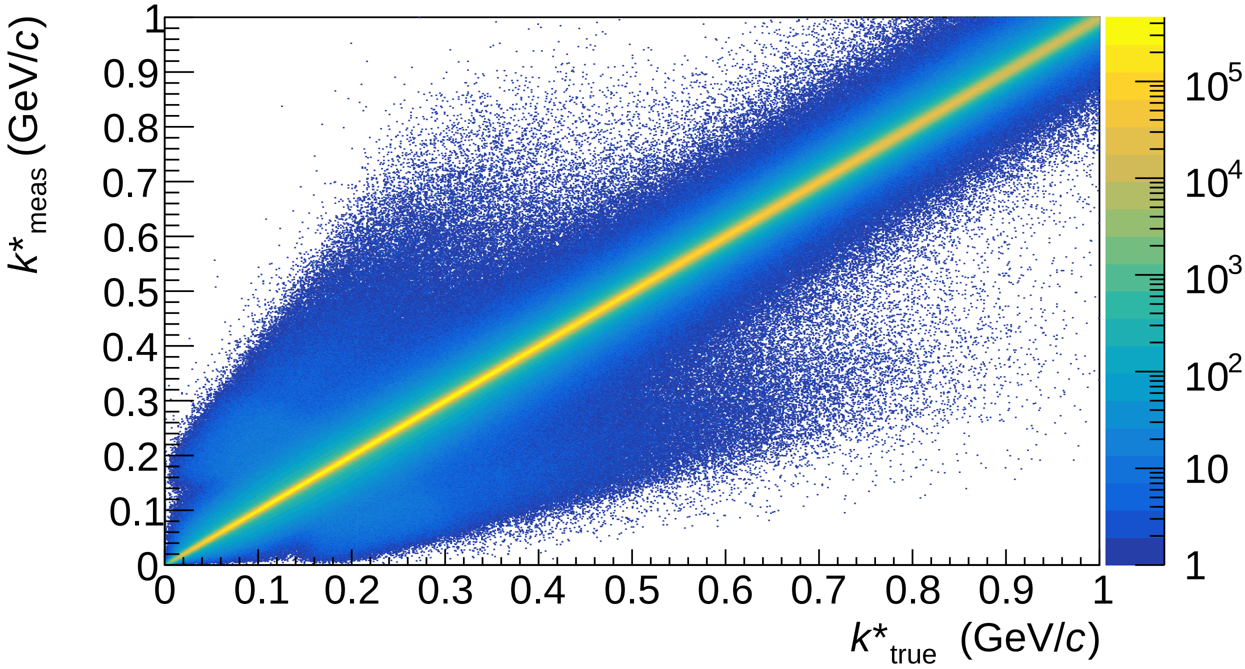

Figure 5.1: Momentum resolution matrices for same event of π^+–π^+ obtained in MC simulation.

algorithm employed may fail to handle them properly. Two effects need to be addressed, firstly the case of track-merging, in which two in reality distinct tracks may be reconstructed as only one track, and secondly the case of track-splitting, where the inverse occurs. In either case fake correlations are introduced impacting the very region of interest, which lies below $0.2\,\mathrm{GeV}/c$ in k^*, due to a depletion (enhancement) of pairs seen in case of track-merging (track-splitting). Those effects are investigated with the help of MC studies based on Pythia 8.1, by studying the difference in the angular separation of the tracks.

The separation between a pair of tracks is parameterized in the longitudinal direction by the difference in pseudorapidites $\Delta\eta$ and in the transverse plane by the difference in the azimuthal angle $\Delta\varphi^*$, defined as

$$\varphi^* = \varphi + \arcsin\left(\frac{0.3r \cdot e \cdot B}{2p_{\mathrm{T}}} \cdot \frac{1}{\mathrm{mT}}\right), \tag{5.2}$$

and takes the curvature of the track within the TPC volume due to the Lorentz force into account. For the analysis $\Delta\varphi^*$ is evaluated for nine different radii r within the TPC, namely at 85, 105, 125, 145, 165, 185, 205, 225, 245 cm and averaged. In Fig. 5.2 the distribution of $\Delta\eta$ versus $\langle\Delta\varphi^*\rangle$ is shown for same and mixed event at r equal to 85 cm. As expected, in the mixed event sample no structure is observed, since the tracks stem from different events, whereas for the same event sample a clear enhancement close to the origin at (0,0) is apparent.

In the absence of any correction the correlation function may be biased due to the reconstruction inefficiency, hence a circular cut within the $\langle\Delta\varphi^*\rangle$-$\Delta\eta$ plane of $\sqrt{\langle\Delta\varphi^*\rangle^2 + \Delta\eta^2} < 0.01$ is applied.

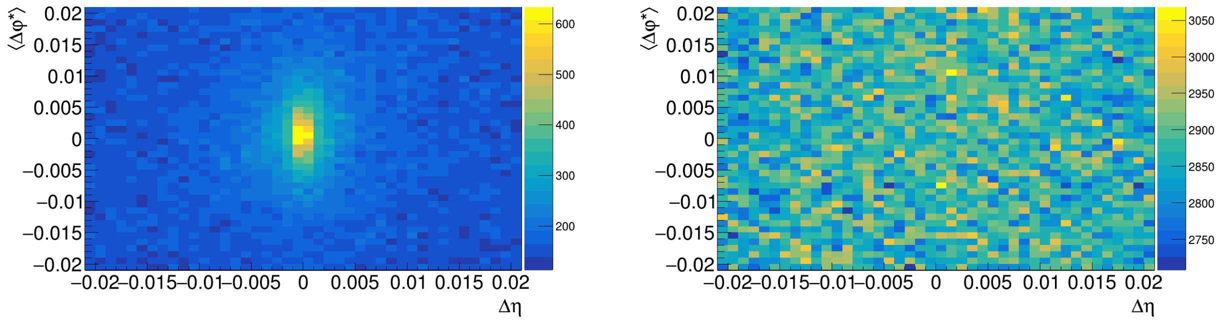

Figure 5.2: The two-dimensional $\langle \Delta\varphi^* \rangle$-$\Delta\eta$ distribution (at r equal to 85 cm) for the same (*left*) and mixed (*right*) event distributions without any modification obtained from MC. The enhancement of the same event is clearly visible and due to track splitting.

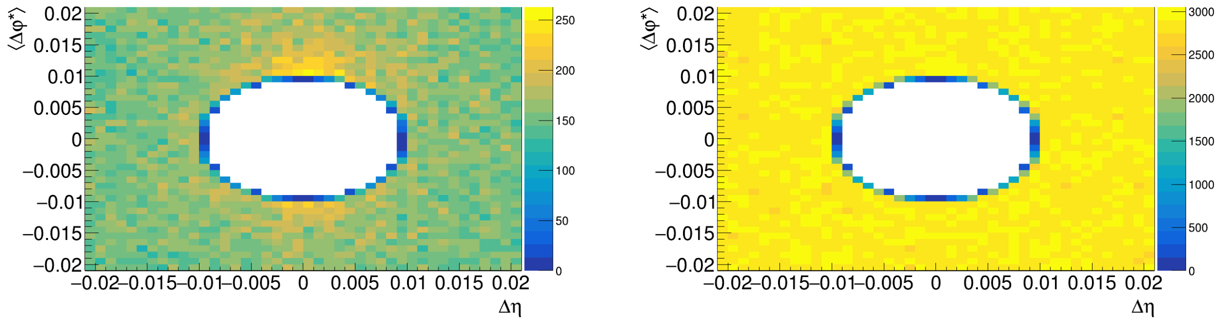

Figure 5.3: The two-dimensional $\langle \Delta\varphi^* \rangle$-$\Delta\eta$ distribution for the same (*left*) and mixed (*right*) event distributions with cuts obtained from MC. The deficiency of the same event is cut away from the sample.

With this choice the full reconstruction inefficiency in $\langle \Delta\varphi^* \rangle$ is removed from the sample, although no variations of the cut were included in the estimation of the systematic uncertainties associated with this particular choice for the cut value, it was checked that the obtained correlations are not influenced by lowering the cut value by 20 %. The impact on the $\langle \Delta\varphi^* \rangle$-$\Delta\eta$ distribution is presented in Fig. 5.3 , where no longer any enhancement due to track-splitting is visible.

5.1.3 Event Mixing

It is vital that the prepared mixed event sample is subject to the same detector acceptance as the same event sample, since these effects cancel when the ratio is built. To ensure this the mixing procedure is conducted only between particle pairs stemming from events with similar z position of the primary vertex[1] and multiplicity[2] [23]. The bin width for the z vertex position is 2 cm and ranges from -10 up to 10 cm with respect to the nominal interaction point. The multiplicity is grouped in the following equivalence-classes: 0–4, 5–8, 9–12, 13–16, 17–20, ..., 93–96, 97–100, >100. In order to estimate

[1]The primary vertex corresponds to the point at which the inelastic pp collision took place. Details are given in ch. 2.
[2]Multiplicity refers to the amount of detected charged particles. Details are given in ch. 2.

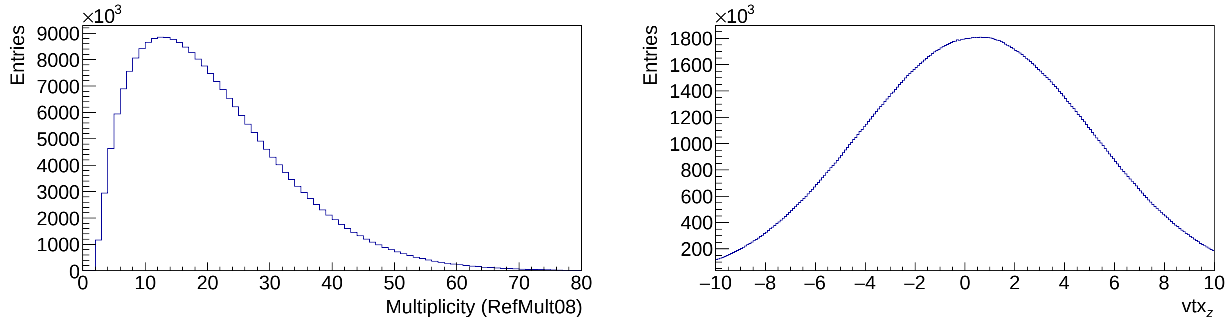

Figure 5.4: *Left*: Reference multiplicity Ref08 in $|\eta|<0.8$. *Right*: z-vertex distribution for pp collisions. Both observables are used for event mixing.

the multiplicity the reference multiplicity RefMult08[3], within a pseudorapidity interval of $|\eta|<0.8$, is employed. The distribution of the z-vertex and the number of global tracks per event is shown in Fig. 5.4. The asymmetry observed in the z-vertex distribution is due to differences in the trigger efficiencies caused by the asymmetric placement of the V0 detectors.

5.1.4 Multiplicity re-weighting of mixed event distributions

Since the mixed event distribution is build by pairing single particles from different events, the selected particles do not need to be paired within the same event sample. The mixed pairs are created using 10 different events within the same z vertex position and multiplicity bin. Although the generated sample gives conceptually exactly the k^* for uncorrelated particles (see Eq. (1.3)), and hence properly reflects the single particle properties, the amount of single particle and pair of particles scales differently with multiplicity.

In order to suppress this effect the mixed event can be re-weighted multiplicity-bin-wise. This procedure ensures that the statistical weight with which the mixed event sample contributes to the correlation function equals the contribution from the same event for a k^* range of 0.2–0.9 GeV/c. In Fig. 5.5 an example of the re-weighting is shown for the multiplicity integrated π^+–π^+ correlation function. The rise of the correlation function starting at k^* larger than $0.8\,\mathrm{GeV}/c$ in k^* is partially suppressed. The remaining components of the correlation signal in this region constitute the background for this analysis and will be discussed in sec. 5.3.

5.2 Decomposition of the correlation function

The correlation signal of the measured pairs, can be affected by non-genuine contributions. Such contributions include both misidentified and feed-down particles from either weak or strong decays of resonances. Hence the measured correlation function is a superimposed signal of all these processes. How to treat each component of the correlation function is shown in [53, 56]. In the following the same

[3]This is a function from the ALICE Software package and an inherent part of multiplicity estimation process used within the ALICE collaboration. The function is well maintained by the Data preparation group (DPG) of ALICE.

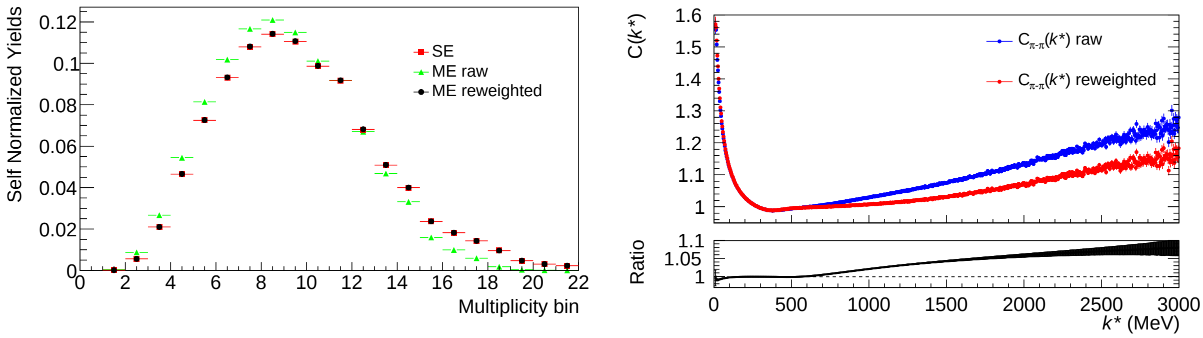

Figure 5.5: (*Left*) same event and re-weighted ME for the π^+–π^+ correlation function, (*Right*) the resulting π^+–π^+ correlation function before and after the re-weighting and (*Bottom panel*) the ratio of the two correlation functions, zoomed in to the region of 0–0.4 GeV/c in k^*.

strategy is employed. The correlation function is written as:

$$C_{\mathrm{model}}(k^*) = 1 + \sum_{i,j} \lambda_{i,j}(C_{i,j}(k^*) - 1). \tag{5.3}$$

The distinct contributions are labeled by the subscript and the relative weight is denoted by λ. Using this notation, the correlation function is decomposed into the genuine and residual signal. For the genuine component the particles of the pair originate from the initial pp collisions or a short-lived strongly decaying resonance. For the residual (feed-down), at least one particle of the pair originates from either the weak or long-lived strong decay of a resonance or a misidentification.

In accordance with [53, 56] the λ parameters are obtained in a data-driven approach by employing exclusively single particle properties namely the purity $\mathcal{P}$ and the channel specific fractions f

$$\lambda_{i,j} = \mathcal{P}_i f_i \mathcal{P}_j f_j, \tag{5.4}$$

where the i, j denote the origin of the particles.

As demonstrated in sec. 4.2 a large portion of the yield of charged pions stems from feed-down of either strongly or weakly decaying resonances. For this work all possible sources of charged pions are taken into account and grouped in one of the following five main categories:

1. $\lambda_{\mathrm{primordial}}$, composed of the particles produced directly in the pp collision, and are not a decay of product of any resonance.
2. $\lambda_{c\tau<5\ \mathrm{fm}}$, all the particles stemming from the strong decay of a resonance with $c\tau_{\mathrm{res}} < 5\,\mathrm{fm}$.
3. $\lambda_{c\tau>5\ \mathrm{fm}}$, all the particles stemming from the strong decay of a resonance with $c\tau_{\mathrm{res}} > 5\,\mathrm{fm}$.
4. λ_{weak}, entails all pairs where at least one particle originated from a long-lived weak decay.
5. λ_{misid}, the signal from misidentifications and particles which were produced by an interaction with the detector material, this contribution is highly suppressed due to the high purity of the sample.

Typically, the genuine correlation signal is associated with the sum of the primordial particles and those produced via strong decays. These particles are defined as »primary«, and correspondingly

$$\lambda_{\mathrm{primary}} = \lambda_{\mathrm{primordial}} + \lambda_{c\tau<5\ \mathrm{fm}} + \lambda_{c\tau>5\ \mathrm{fm}} \tag{5.5}$$

For reasons that will become apparent later (see sec. 5.5.3), in this work the genuine signal is defined as

$$\lambda_{\text{genuine}} = \lambda_{\text{primordial}} + \lambda_{c\tau<5\text{ fm}} = \lambda_{\text{primary}} - \lambda_{c\tau>5\text{ fm}} \tag{5.6}$$

while the remaining feed-down is grouped together as

$$\lambda_{\text{feed}} = \lambda_{c\tau>5\text{ fm}} + \lambda_{\text{weak}}. \tag{5.7}$$

These λ-parameters can be calculated using Eq. (5.4). In fact, the fraction f_{primary} was already extracted from the MC templates fit of DCA_{xy} distributions (see sec. 4.2), while the relative amount of resonances with $c\tau_{\text{res}} > 5\,\text{fm}$, denoted by $\mathcal{F}_{c\tau>5\text{ fm}}$, is evaluated using Thermal-FIST (see sec. 4.1).

The final decomposition of the correlation function reads

$$\begin{aligned} C_{\text{model}}(k^*) = 1 &+ \lambda_{\text{genuine}} \cdot (C_{\text{genuine}}(k^*) - 1) \\ &+ \lambda_{\text{feed}} \cdot (C_{\text{feed}}(k^*) - 1) + \lambda_{\text{misid}} \cdot (C_{\text{misid}}(k^*) - 1). \end{aligned} \tag{5.8}$$

This correlation function can be used to fit the measured correlation function and test models for the interaction or study the functional form of the particle emitting source.

5.2.1 Calculation of λ parameters

The detailed explanation on how the fraction of charged pions stemming from strong resonance decays was estimated has been reported in sec. 4.1. The main result important for the calculation of the λ_{genuine} is $\mathcal{F}_{c\tau>5\text{ fm}} = 12.2\,\%$. Additionally, using the p_{T} weighted value of 99 % for the purity $\mathcal{P}$ of the charges pions (see. sec. 4.2) and the fraction of primaries f_{primary} of 93.8 % from Tab. 4.5 all ingredients in order to calculate λ_{genuine} are fixed:

$$\lambda_{\text{genuine}} = (f_{\text{primary}}(1 - \mathcal{F}_{c\tau>5\text{ fm}}))^2 \cdot \mathcal{P}^2 \tag{5.9}$$

$$\lambda_{\text{genuine}} = (0.938(1 - 0.122))^2 \cdot 0.99^2 = 0.664. \tag{5.10}$$

The value for λ_{misid} was estimated to be 0.02 since this contribution is heavily suppressed due to the high purity and the low amount of charged pions stemming from interaction with the detector material (also called materials).

Finally the λ_{feed} is calculated by using the normalization condition for the relative weights, which is given by the fact that the sum overall all weights must be equal to unity.

$$\lambda_{\text{feed}} = 1 - \lambda_{\text{genuine}} - \lambda_{\text{misid}} = 0.316. \tag{5.11}$$

Summarizing the findings for the λ parameters, the genuine λ_{genuine} is 66.4 %, the feeddown λ_{feed} is 31.6 % and the misidentified (or materials) λ_{misid} is 2.0 %.

5.3 Non-femtoscopic background

The sphericity cut was already introduced in sec. 3.1 and is needed in order to suppress the mini-jet background. As in the case of jet-like events particles will be emitted predominantly within a jet-cone and hence are strongly correlated in momentum space, introducing a bias to the correlation function. This effect is most pronounced for small particle multiplicities as back-to-back emission is favoured due to energy-momentum conservation. Further, a rise of the correlation function is observed for large k^* which is also attributed to energy-momentum conservation [40] and can be parametrized by a polynomial.

In order to get an estimate of the shape for the background within the region of small k^* ($< 250\,\mathrm{MeV}/c$), the correlation function is computed from MC simulations, employing identical cuts (described in sec. 3.2) as to the data. Since in Pythia 8.1 no femtoscopic effects are implemented, the correlation function is expected to be driven purely by non-femtoscopic correlations. As the multiplicity and k_T integrated correlation function of π^+–π^+ and π^-–π^- are consistent within the respective uncertainties, the sum of both denoted by π–π will always be shown, the ratio between π^+–π^+ and π^-–π^- is shown in the appendix C. The π–π correlation functions were obtained in five k_T-bins, namely 0.15–0.30, 0.30–0.50, 0.50–0.70, 0.70–1.5 GeV/c, for the multiplicity classes of $N_\mathrm{Ch} \in [0-18]$, $N_\mathrm{Ch} \in [19-30]$ and $N_\mathrm{Ch} > 30$ and are displayed in Fig. 5.6. In most of the k_T bins a flat behaviour at low k^* values is observed, although in some cases a depletion is visible. The agreement between simulation and data, at k^* values above $250\,\mathrm{MeV}/c$, where no final state interaction is present, becomes better with increasing multiplicity and increasing values for k_T. The largest deviation is found in the last three k_T bins in the first multiplicity bin.

A very similar behaviour of Pythia was observed in a study of identical charge kaon and pion femtoscopic correlations [39]. In order to account for the background, $C(k^*)$ computed from data are divided by the $C(k^*)$ from the simulation. This ratio will from now on be referred to as corrected correlation function. Due to the non-perfect description of the background provided by Pythia, the remaining discrepancy is modeled by assuming either a linear or a quadratic baseline. The parameters of the baseline will be left free during the subsequent fitting procedure.

Due to the highly non-monotonic behaviour of the MC correlation at small k^* values, additional systematic checks have been performed regarding the sphericity determination, which could influence the correlation shape in that region. In particular, the condition of requiring events containing at least 3 tracks with a minimum p_T of $0.5\,\mathrm{GeV}/c$ has been varied to $0.4\,\mathrm{GeV}/c$ and $0.6\,\mathrm{GeV}/c$ (see Fig. 5.7 and Fig. 5.8). It was found that the ratio at small k^* between the correlation functions computed from data and MC simulation is not strongly sensitive to this criterion. Hence using the corrected correlation functions does not introduce any bias to the analysis. Changing the parameters for the sphericity calculation modifies the sub-sample of analysed events. Therefore for the sphericity no contribution to the systematic uncertainty is considered. For all following correlation functions the default value for the p_T resolution of $0.5\,\mathrm{GeV}/c$ is used.

5.4 Modeling of the correlation function

For the π–π correlation function the Coulomb interaction and symmetrization of the wave-function are considered and the theoretical modelling is performed using CATS [57]. The range of the strong π–π interaction is expected to be around 0.2 fm [58], therefore for typical source sizes in pp collisions of 1 fm, the imprint of the interaction on the correlation function should be in approximation negligible. Furthermore the scattering length [59] $a_0^{I=2} = -0.0444\,\mathrm{fm}$ is very small, hence only a subtle modification of the momenta is due to the interaction is expected. Fig. 5.9 shows the theoretical correlation function where a Gaussian source with a radius $r_0 = 1.5\,\mathrm{fm}$[4] was assumed. The functional form of a Gaussian

[4] This value for the radius is chosen arbitrary, and only serves for demonstration purposes.

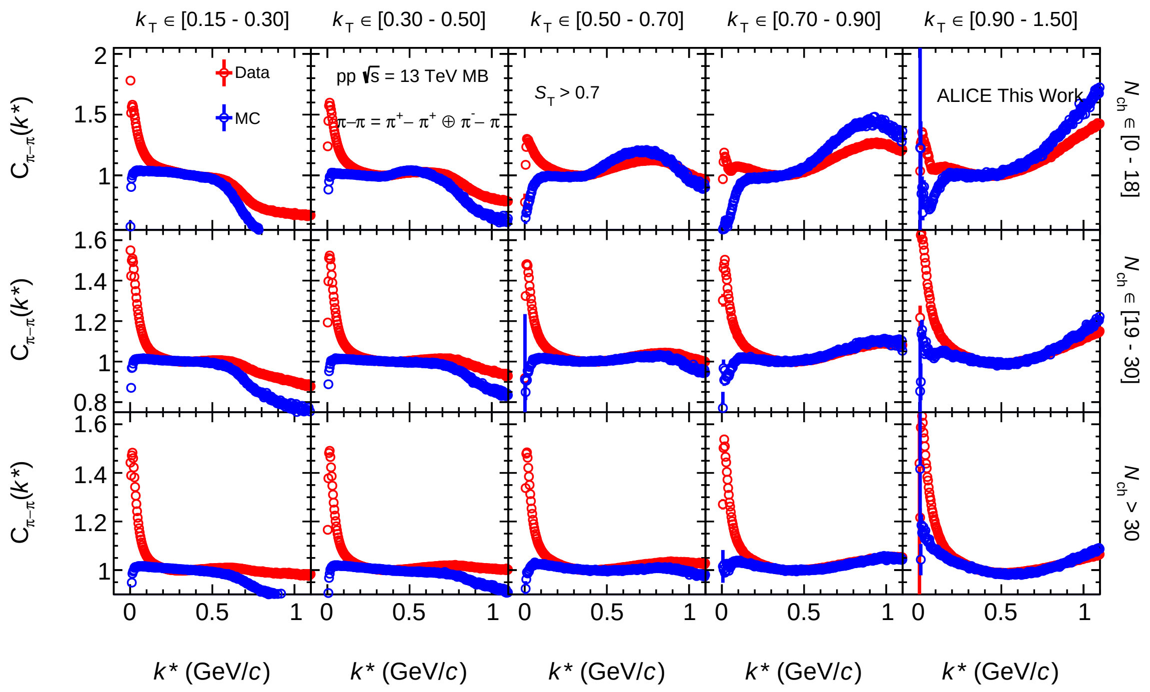

Figure 5.6: Display of all the correlation function obtained from data and MC in all the considered multiplicity and k_T bins.

source reads

$$S(r^*) = \frac{1}{(4\pi r_0^2)^{3/2}} \exp\left\{\left(-\frac{r^{*2}}{4r_0^2}\right)\right\}, \tag{5.12}$$

where r_0 is the size of the source. The correlation function is above unity due to the effect of the Bose-Einstein statistics, except at $k^* < 20\,\mathrm{MeV}/c$, which shows a strong depletion due the now dominant Coulomb interaction, which is repulsive for a pair of same charge pions. The width of the correlation function strongly depends on the source size.

As already shown in sec. 5.2, for the $C(k^*)$ the final decomposition is given by:

$$C_\mathrm{model}(k^*) = 1 + \lambda_\mathrm{genuine} \cdot (C_\mathrm{genuine}(k^*) - 1) \\ + \lambda_\mathrm{feed} \cdot (C_\mathrm{feed}(k^*) - 1) + \lambda_\mathrm{misid} \cdot (C_\mathrm{misid}(k^*) - 1). \tag{5.8}$$

The residual correlations are $C_\mathrm{feed}(k^*)$ and $C_\mathrm{misid}(k^*)$. Due to the large $c\tau_\mathrm{res}$ of the weak components and the usage of misidentified particles, the correlations associated with C_feed and C_misid are assumed to be flat and thus equal to unity. This simplifies the above relation to

$$C_\mathrm{model}(k^*) = 1 + \lambda_\mathrm{genuine} \cdot (C_\mathrm{genuine}(k^*) - 1), \tag{5.13}$$

where the only remaining contribution is due to genuine charged pions.

The study of the non-femtoscopic background was described in sec. 5.3, where it was concluded that building the ratio of correlation functions computed from data and MC simulations can partially remove

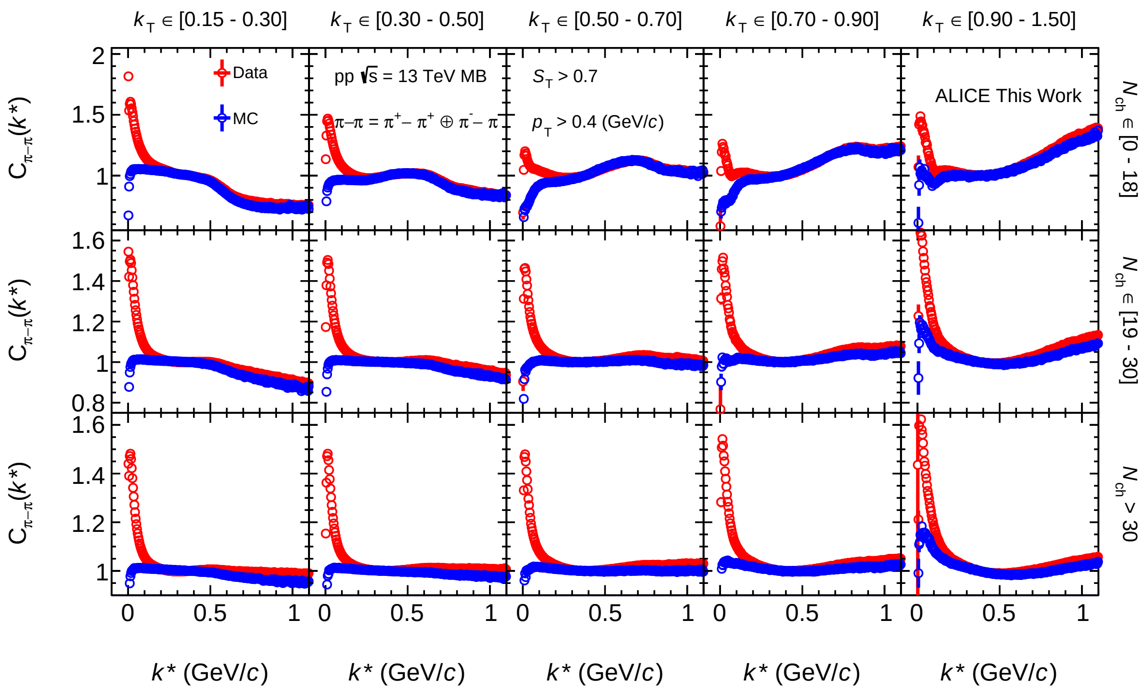

Figure 5.7: Display of all the correlation function obtained from data and MC in all the considered multiplicity and k_{T} bins with a p_{T} resolution cut of 0.4 GeV/c.

the mini-jet background. However, as the description of the long-range correlations present in the data is imperfect, it is expected that even after this correction a residual non-femtoscopic background is still persistent in the ratio. In order to account for the remaining contamination, a polynomial baseline is introduced. As a conservative approach, and to study the associated systematic uncertainty, either a linear or quadratic polynomial is assumed. The fitting function reads

$$C_{\mathrm{Fit}}(k^*) = (a + b \cdot k^* + c \cdot k^{*2}) \cdot C_{\mathrm{model}}(k^*), \tag{5.14}$$

where $C_{\mathrm{model}}(k^*)$ incorporates the theoretical model, which includes the effects of Coulomb and quantum statistics, and is scaled with the corresponding λ parameter as discussed in sec. 5.2. The free fit parameters are the polynomial factors a, b, c and the radius of the Gaussian source, which is included in the computation of $C_{\mathrm{model}}(k^*)$. Details on the emitting source are given in the next section.

5.5 Modeling of the femtoscopic source

5.5.1 Overview

One of the main motivations for studying the particle emitting source in small systems, e.g. pp collisions, is to test the hypothesis of an universal spatio–temporal hadronisation for all hadrons. On one hand, this would help to understand the QCD related properties of the hadronisation process. On the other hand, constraining the emission can be used to employ femtoscopy as a tool to study the

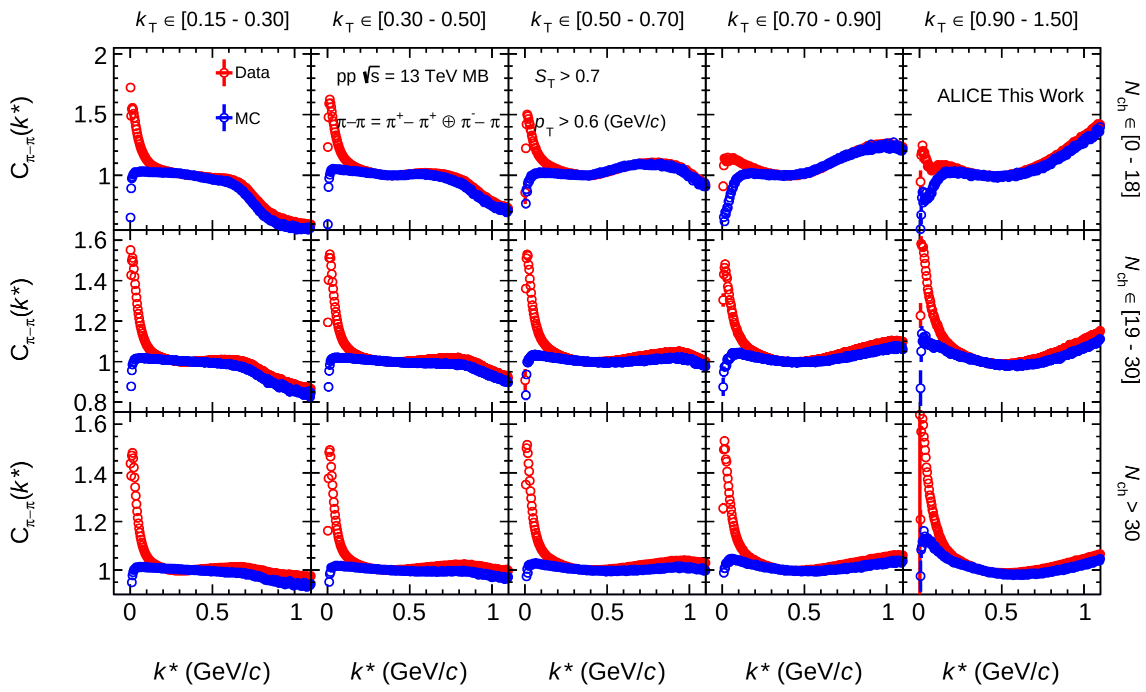

Figure 5.8: Display of all the correlation function obtained from data and MC in all the considered multiplicity and k_{T} bins with a p_{T} resolution cut of 0.6 GeV$/c$.

strong interaction among exotic particle pairs, such as p–Ξ or p–Ω, that are otherwise experimentally inaccessible [13].

The Koonin-Pratt equation has two main ingredients: the source and the interaction. Since the correlation function is an integrated quantity, to test either of the two with a good precision requires the knowledge of the other. Hence, studying the interaction potential, requires the source to be fixed from a system where the interaction is better constrained, such as p-p. In [8] it was demonstrated that the p–p and p–Λ systems have essentially an identical source function, when studied as a function of m_{T} and explicitly correcting for particle production via the decays of strong lived resonances. This study is seen as a solid proof for the common source hypothesis, if applied to the baryon-baryon sector, which corresponds to large m_{T} values between 1 and 2.5 GeV$/c^2$.

After the successful application of the method in the baryon-baryon sector the question arises whether this prescription is valid for all types of particles, and in particular for light mesons, such as charged pions, which can probe the m_{T} region below 1 GeV$/c^2$. It is well established that a Gaussian emission profile fails to describe the $C(k^*)$ of identical pions in small collision systems, and that the best fits to the available data are provided by an exponential source [5, 6, 60]. This observation is often attributed to the large fraction of charged pions originating from strongly decaying short-lived resonances. However, while this claim is widely accepted, it was never quantitatively tested, and this work aims at elaborating on the subject.

In accordance to the baryon-baryon analysis, a Gaussian emission profile for all primordial particles and resonances is assumed. The amount and composition of the feed-down into charged pions from strong

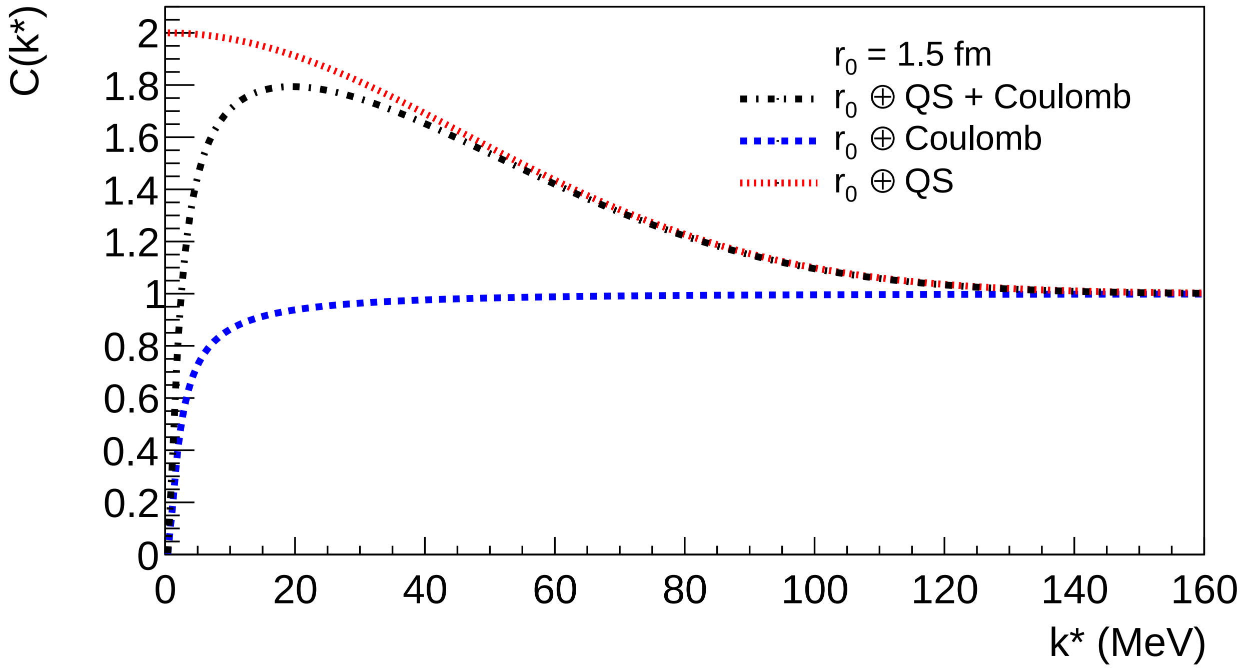

Figure 5.9: Theoretical correlation function for π–π obtained with CATS, The source radius is $r_0 = 1.5\,\mathrm{fm}$. The red correlation function exclusively includes the symmetrization of the wave-function for bosons, while the blue one only the repulsive Coulomb interaction between same charge particles. The black correlation function incorporates both effects and is the result of the interplay between the symmetrization of the wave-function and the repulsive Coulomb interaction.

decays are determined from Thermal-FIST, while the kinematics are fixed from the EPOS transport model [25, 49], as stated in ch. 4. The modification of the source size is computed by the already existing Monte-Carlo procedure [8], which is explained in the next section.

5.5.2 Non-gaussian contributions to the source function

As demonstrated in [8], strongly decaying short-lived resonances can significantly distort the Gaussian profile of the source. According to the work of U. Wiedemann and U. Heinz [61] all resonances of width smaller then 1 MeV ($c\tau > 200$ fm) can safely be considered as long-lived, leading to an essentially flat correlation signal. This allows to describe these resonances by using the formalism of the λ-parameters (see ch. 5.2). However, pions are also affected by resonances with intermediate lifetimes, in particular $\omega(782)$ with a $c\tau_{\mathrm{res}} = 23\,\mathrm{fm}$.

Quantifying the effect of the resonances analytically is challenging, even if the angular dependence in the emission is ignored. For this reason using a Monte-Carlo procedure is a more practical choice, as already demonstrated for baryon-baryon pairs [8]. This procedure has now been extended to the pion-pion analysis, and it relies on the input from Thermal-FIST regarding the yields of the resonances and on the EPOS model to fix the kinematics of the primordial emission. The latter is sketched in Fig. 5.10.

The ansatz is that all primordial particles or resonances are emitted at an initial distance r^*_{core}. In case

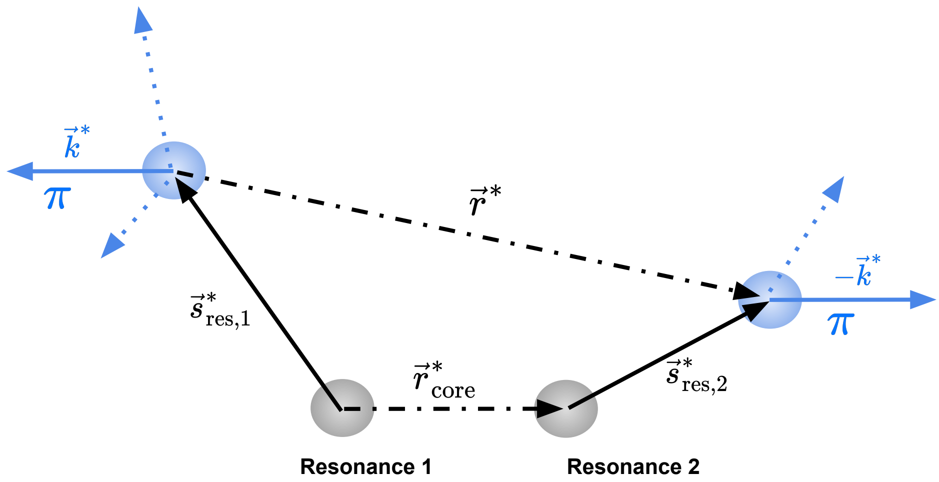

Figure 5.10: Depiction showcasing the propagation of resonances from an initial relative emission $\boldsymbol{r}^*_{\mathrm{core}}$ to the final separation $\boldsymbol{r}^*$. All computations are performed in the rest frame of the daughters. If one of the initial state particles is not a resonance but a primordial particle of the investigated species, the corresponding $\boldsymbol{s}^*_{\mathrm{res}}$ is set to zero. Shown is a reproduction from [8].

a resonance is emitted, before decaying into a charged pion it will travel an average decay-length ($\boldsymbol{s}^*_{\mathrm{res}}$) given by

$$\boldsymbol{s}^*_{\mathrm{res}} = \boldsymbol{\beta}^*_{\mathrm{res}}\gamma^*_{\mathrm{res}}\tau_{\mathrm{res}} = \frac{\boldsymbol{p}^*_{\mathrm{res}}}{m_{\mathrm{res}}}\tau_{\mathrm{res}}, \tag{5.15}$$

leading to a modification of the relative distance r^* between the measured pair of charged pions. In Eq. (5.15) $\boldsymbol{p}^*_{\mathrm{res}}$ is the momentum, m_{res} is the mass and τ_{res} is the lifetime of the corresponding resonance.

The modification of the source function can be expressed with the following vector relation:

$$\boldsymbol{r}^* = \boldsymbol{r}^*_{\mathrm{core}} - \boldsymbol{s}_{\mathrm{res},1} + \boldsymbol{s}_{\mathrm{res},2}, \tag{5.16}$$

where $\boldsymbol{r}^*$ is the distance between the final pair of interest, after their two mother resonances have been propagated by $\boldsymbol{s}_{\mathrm{res},1}$ and $\boldsymbol{s}_{\mathrm{res},2}$ respectively. The minus sign in front of $\boldsymbol{s}_{\mathrm{res},1}$ is chosen in accordance with the geometrical definition of the process presented in Fig. 5.10. The source function is described by the distribution of the magnitude of $\boldsymbol{r}^*$, which can only be evaluated by knowing the relative orientation of all vectors. This non-trivial task requires the usage of a transport model. In the presented work this has been achieved by using the EPOS model. Using the dot-product of $(\boldsymbol{r}^* \cdot \boldsymbol{r}^*)$ (Eq. (5.16)) the corresponding magnitude can be evaluated:

$$\begin{aligned}
(r^*)^2 = r^{*2}_{\text{core}} &+ \frac{p^{*2}_{\text{res},1}}{M^2_{\text{res},1}}\tau^2_{\text{res},1} + \frac{p^{*2}_{\text{res},2}}{M^2_{\text{res},2}}\tau^2_{\text{res},2} \\
&- 2r^*_{\text{core}}\frac{p^*_{\text{res},1}}{M_{\text{res},1}}\tau_{\text{res},1}\cos(\angle \boldsymbol{r}^*_{\text{core}}, \boldsymbol{p}^*_{\text{res},1}) \\
&+ 2r^*_{\text{core}}\frac{p^*_{\text{res},2}}{M_{\text{res},2}}\tau_{\text{res},2}\cos(\angle \boldsymbol{r}^*_{\text{core}}, \boldsymbol{p}^*_{\text{res},2}) \\
&- 2\frac{p^*_{\text{res},1}p^*_{\text{res},2}}{M_{\text{res},1}M_{\text{res},2}}\tau_{\text{res},1}\tau_{\text{res},2}\cos(\angle \boldsymbol{p}^*_{\text{res},1}, \boldsymbol{p}^*_{\text{res},2})
\end{aligned} \tag{5.17}$$

Three different scenarios regarding the origin of the pair of charged pions need to be taken into account: primordial-primordial, primordial-resonance, and resonance-resonance pairs. The probability of each scenario is given by PP, $P\tilde{P}$, and $\tilde{P}\tilde{P}$, where P is the fraction of primordial charged pions and $\tilde{P} = 1 - P$ is the fraction of charged pions originating from short-lived resonances. These fractions are evaluated using Thermal-FIST[5] (see sec. 4.1) to be $P = 0.318$ and $\tilde{P} = 0.682$. The total source can hence be decomposed to

$$S(r^*) = PP \times S_{PP}(r^*) + P\tilde{P} \times S_{P\tilde{P}}(r^*) + \tilde{P}\tilde{P} \times S_{\tilde{P}\tilde{P}}(r^*). \tag{5.18}$$

The full Monte-Carlo procedure used to generate the source function is summarized as follows:

1. The amount of resonances and primordial yields for charged pions are estimated using Thermal-FIST. This information allows to evaluate the average mass $\langle m^{\text{eff}}_{\text{res}} \rangle$ and lifetime $\langle c\tau^{\text{eff}}_{\text{res}} \rangle$ of the contributing resonances.
2. Primordial charged pions and resonances are selected from EPOS events, with the constraint to reproduce $\langle m^{\text{eff}}_{\text{res}} \rangle$ and $\langle c\tau^{\text{eff}}_{\text{res}} \rangle$. For the selection 21×10^6 events were produced, for which EPOS was tuned to pp collisions at $\sqrt{s} = 13\,\text{TeV}$. An acceptance cut of $|\eta| < 0.5$ was applied in order to match the region to which Thermal-FIST is fine tuned.
3. The selected EPOS particles are paired according to two scenarios: primordial-resonance and resonance-resonance pairs. As $\boldsymbol{r}^*$ coincides with $\boldsymbol{r}^*_{\text{core}}$ in the case of primordial-primordial pair this case is excluded from further processing.
4. Each generated pair is processed further, by propagating and decaying the resonances using TGenPhaseSpace[1]. This has been performed by using the averaged values $\langle m^{\text{eff}}_{\text{res}} \rangle$ and $\langle c\tau^{\text{eff}}_{\text{res}} \rangle$ computed above.
5. The system is boosted into the pair rest frame of the final-state charged pions.
6. Only particles that are subject to the femtoscopic analysis ($k^*_{\text{cutoff}} = 200\,\text{MeV}/c$) are concidered for the description of the source function.
7. The separation between the final particles is evaluated following Eq. (5.17), where r^*_{core} is sampled from a Gaussian emission of width r_{core} (see Eq. (5.12)), the masses and lifetimes are fixed to $\langle m^{\text{eff}}_{\text{res}} \rangle$ and $\langle c\tau^{\text{eff}}_{\text{res}} \rangle$ and the angles are taken from EPOS.

[5] As previously the fractions are properly re-normalized in order to exclude contributions from long-lived strongly decaying resonances.

[1] ROOT functionality for simulating n-body decays: https://root.cern.ch/doc/master/classTGenPhaseSpace.html

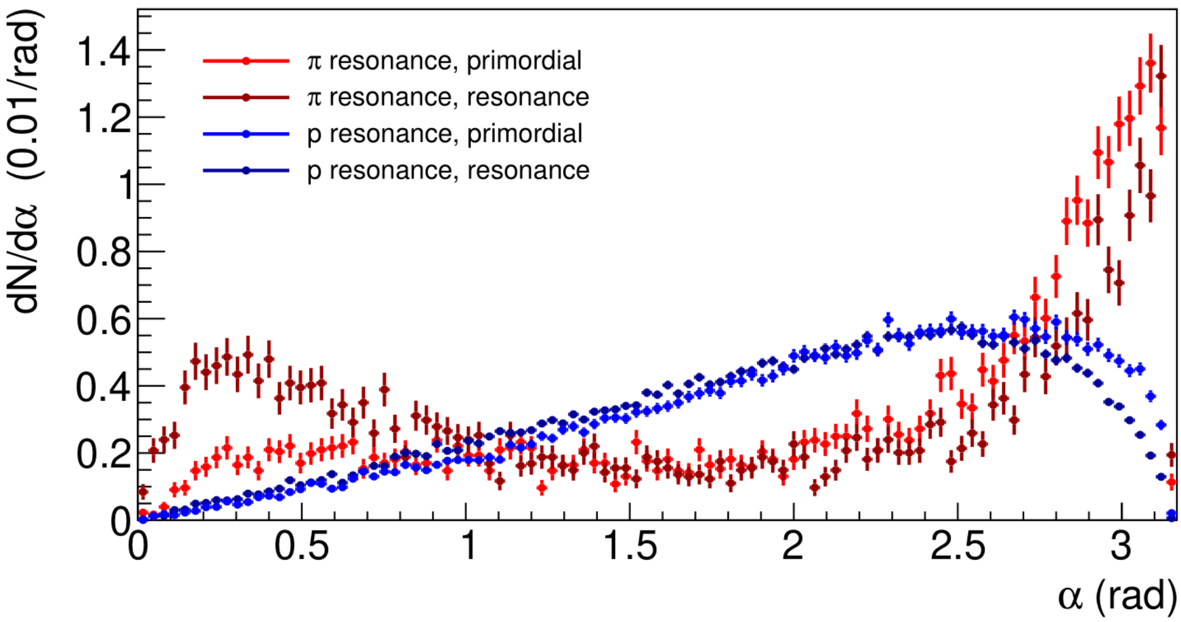

Figure 5.11: The distribution of $\alpha = \angle(r^*_{\mathrm{core}}, p^*_{\mathrm{res},1})$ for pairs of charged pions and protons. The light red (blue) represents α in the case only one of the charged pions (protons) originated from a resonance while the other one is primordial, the dark red (blue) represents the case if both charged pions (protons) originated from resonances. Both distributions are peaked at a preferred back-to-back emission of the resonances, although for the case of two charged pions originating from resonances there is a significant amount of resonances emitted back towards the origin of primordial emission.

8. This procedure is repeated iteratively starting from step nr. 3 until a sufficiently fine distribution for the source function $S(r^*)$ is obtained. Each iteration is performed only for one of the three possible scenarios in Eq. 5.18. The scenario is chosen according to the associated probability calculated from the fractions predicted by Thermal-FIST.

5.5.3 Effect of resonances on the pion source

The angular distribution of $\alpha = \angle(r^*_{\mathrm{core}}, p^*_{\mathrm{res},1})$ as seen in Fig. 5.11 is different for π–π compared to the baryon-baryon pairs [8]. The differences arise due to the involved kinematics of the emitted resonances, in the case of charged pions the $\langle m^{\mathrm{eff}}_{\mathrm{res}} \rangle$ is lighter by 200 MeV/c^2, which facilitates very different kinematics for daughter pions compared to daughter baryons. These kinematic disparities result in much larger boost parameters to the center of mass system of the daughters, causing some daughter charged pions to be emitted in the direction of origin.

In the following, the effect of the resonance yield and composition on the source distribution as well as the resulting correlation function will be investigated using a Monte Carlo toy simulation. The goal is to understand how resonances with intermediate τ_{res} are deforming the source and explain the reason for including the long-lived ($c\tau_{\mathrm{res}} > 5\,\mathrm{fm}$) strongly decaying resonances in the λ-parameter of the weak-component (see sec. 5.2).

The correlation functions are modeled by CATS, where correlations due to Bose-Einstein statistics as well as the Coulomb interaction are included and a Gaussian emission source of 1.5 fm[6] is set-up. The angular distribution from EPOS (Fig. 5.11) is used in all cases, while the effect of the resonances is studied in a step-wise procedure. For each step the resulting source distribution as well as correlation function are shown. The steps are summarized below, the relevant figures are Fig. 5.12-5.18.

1. No contribution from resonances, only a Gaussian source with radius $r_0 = 1.5$ fm (Fig. 5.12).

2. Adding the effect of all short lived resonances with $c\tau_{\mathrm{res}} < 1$ fm, which account for 15% of the charged pion yield (Fig. 5.13). The effect on the source function is only minor, but interestingly it results in a preferred emission of the particles at even closer distances then the core. The reason is related to the angular distributions shown in Fig. 5.11, which allows for a certain fraction of the particles to propagate towards the emission source. The very small lifetime of these resonances means that they decay before reaching the "opposite" side of the origin, leading (on average) to $r^* < r^*_{\mathrm{core}}$. This effect is reflected to the correlation function by a slight increase in the long-range k^* correlation.

3. Adding the effect of the ρ resonances with $c\tau_{\mathrm{res}} = 1.3$ fm, accounting for an additional (total) 17.5% (32.5%) of the charged pion yield (Fig. 5.14). The $c\tau_{\mathrm{res}}$ of this resonance is large enough to see some enhancement of the tail of the source, however it is still small enough so that some particles end up at $r^* < r^*_{\mathrm{core}}$. In terms of the correlation function, the latter results in a further increase in the long-range correlation, while the former translates into a shift of the maximum in $C(k^*)$ towards lower k^*. This already resembles the features of an exponential source.

4. Adding the effect of all resonances with $c\tau_{\mathrm{res}} < 5$ fm, accounting for an additional (total) 27.5% (60%) of the charged pion yield (Fig. 5.15). The additional resonances are longer lived compared to r_{core}, for this reason even if some resonances propagate inwards to the origin of the source, they will most likely decay a few fermi on the opposite side of the origin, resulting in an effective increase of r^* and a significant increase in the tail of the source function. For the correlation function this implies only a modification of the low k^* region, in which the maximum strength of the correlation signal is shifted towards even lower k^*.

5. Adding the effect of $\omega(782)$ with $c\tau_{\mathrm{res}} = 23$ fm, accounting for an additional (total) 7.5% (67.5%) of the charged pion yield (Fig. 5.16). Due to the long lifetime of the $\omega(782)$, the net effect is an overall dampening of the source function, with a large amount of the yield shifted towards the tail of the distribution. The shape of the correlation function is determined by the shape of the source function at distances comparable to r_{core}, while the long tail of the source results in an approximately flat correlation. For this reason, if the source is suppressed by a constant factor at low r^*, the effect on $C(k^*)$ should be identical and can be modeled by an additional λ parameter, leading to $C^{\lambda}(k^*) = 1 + \lambda(C(k^*) - 1)$. The gray line in Fig. 5.16 represents the correlation function from the previous step, scaled down by the appropriate amount (based on the yield of $\omega(782)$), while the green line treats the $\omega(782)$ properly by including it in the source function. There is a small difference, however in a good approximation it can be neglected, implying that the leading order effect of the $\omega(782)$ is a reduction the strength of the correlation signal, without modifying the shape. This is the same effect as in the case of a weak decay.

6. Adding the effect of all remaining long lived resonances with $c\tau_{\mathrm{res}} > 23$ fm, accounting for an additional (total) 5.5% (73%) of the charged pion yield (Fig. 5.17). Here the expectation is to see no significant modifications to the shape $S(r^*)$ at small distances, and correspondingly no

[6] This value for the radius is chosen arbitrary, and only serves for demonstration purposes.

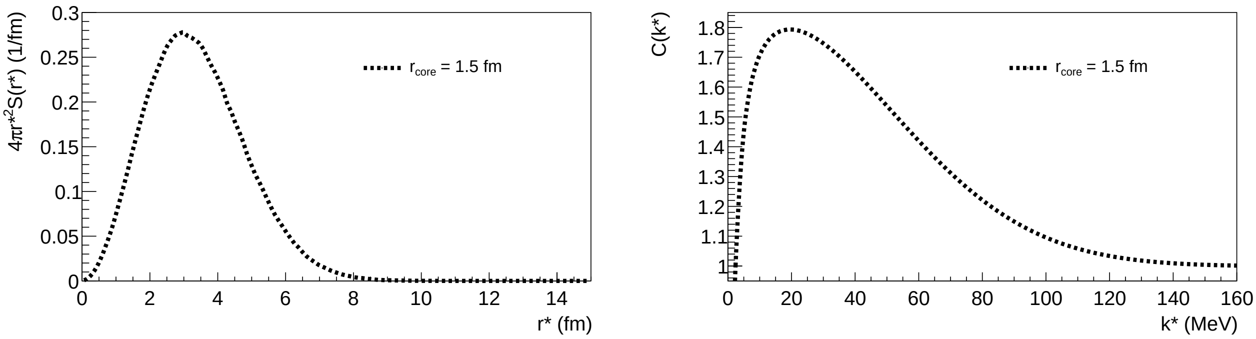

Figure 5.12: The pure Gaussian source (left) and the corresponding correlation function (right).

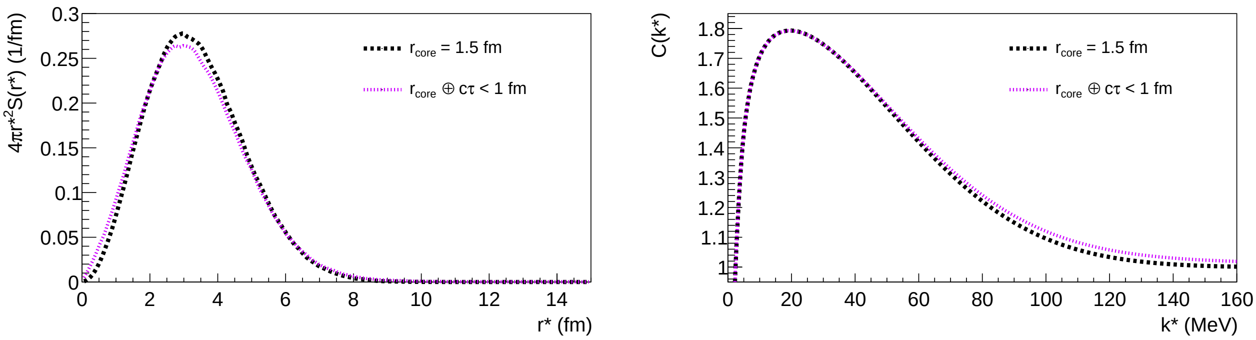

Figure 5.13: The inclusion of resonances with $c\tau_{\mathrm{res}} < 1\,\mathrm{fm}$ leads to a marginal change in the source (left), due to the short lifetime. The resulting correlation function (right) shows only minor modifications in the long-range part.

difference in the shape of $C(k^*)$. The only difference is a reduction of the overall amplitude of both, which as before can be modeled by an effective λ parameter. This is confirmed by Fig. 5.17.

7. Finally the result is compared to an exponential source (Fig. 5.18). The latter is known to provide a good modeling for the π–π source, which within the hypothesis adopted for this work can be interpreted as the effect of strongly decaying resonances on top of a Gaussian core source.

The investigation above provides two important qualitative insights. The first is that including the resonances with $c\tau_{\mathrm{res}} > 5\,\mathrm{fm}$ into the λ_{feed} is well motivated. The second is an understanding why charged pions are well modeled using an exponential source, namely the resonances with $c\tau_{\mathrm{res}} < 5\,\mathrm{fm}$ enhance the long-range correlations, leading to a shift of the maximum of the correlation function towards lower k^*.

5.6 Fitting the correlation function

In this work the evaluation of the theoretical correlation functions has been performed using the CATS framework [57]. The main functionalities of the framework are outlined in this section.

The evaluation of correlation functions is problematic within analytical models. The main limitation is

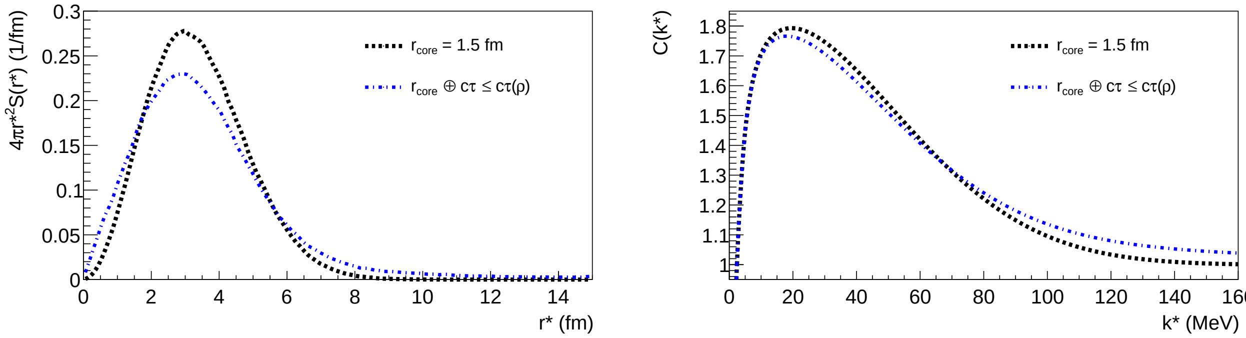

Figure 5.14: The inclusion of the ρ meson leads to a more visible modification to the source (left), as the lifetime of $c\tau_{\mathrm{res}} = 1.3\,\mathrm{fm}$ is comparable to r_{core}. The associated correlation function (right) shows slight modifications as long-range correlation increase and the maximum shifts towards lower r^*. This feature resembles exponential sources.

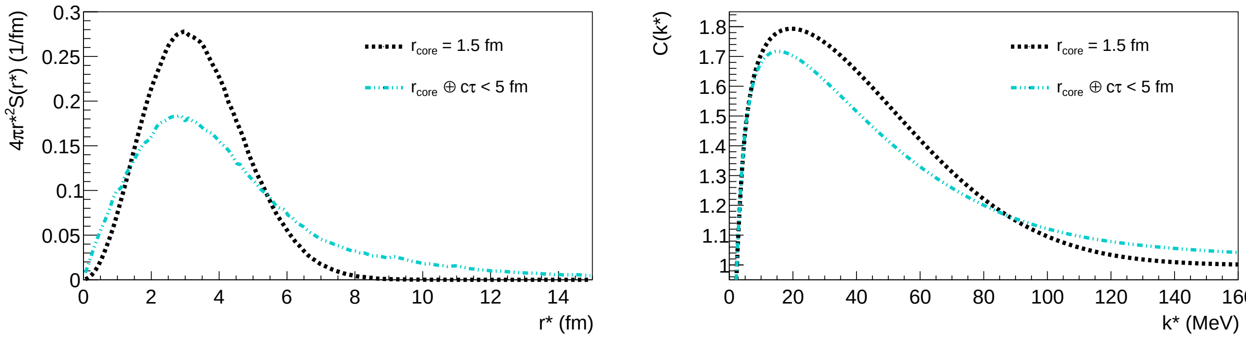

Figure 5.15: The inclusion of longer lived resonances with $c\tau_{\mathrm{res}} < 5\,\mathrm{fm}$ has a large impact on the shape of the correlation (right) at smaller k^*, with the maximum in $C(k^*)$ shifted towards lower values. This is related to the appearance of large exponential tail in the source distribution (left), that is non-flat in the region of r_{core}. This is a similar effect as in the case of an exponential source (Fig. 5.18).

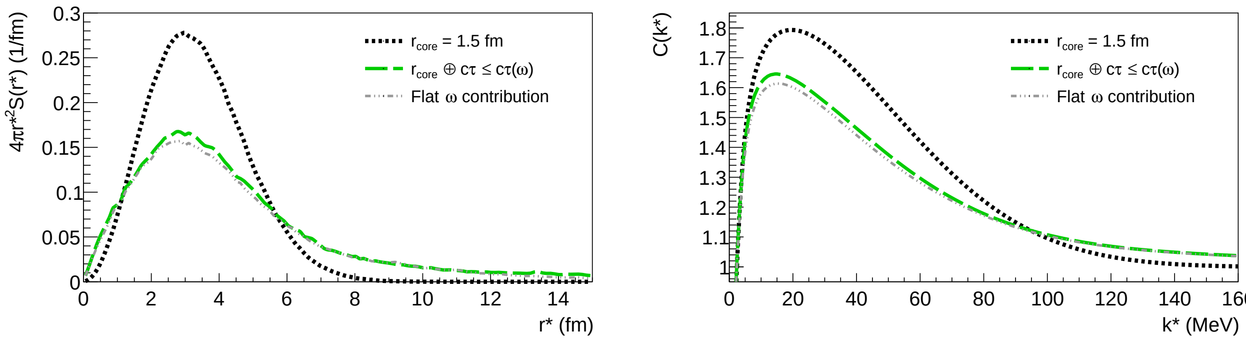

Figure 5.16: The inclusion of the $\omega(782)$ with $c\tau_{\mathrm{res}} = 23\,\mathrm{fm}$ mostly results in a decrease in the amplitude in the source (left) by a constant factor. The rest of the yield is shifted towards a very long exponential tail. The gray lines represent $S(r^*)$ and $C(k^*)$ from Fig. 5.15 scaled down by a factor (λ parameter) reflecting the amount of pion pairs, for which at least one of the particles stems from a ω. It provides a fairly good description of the true (green) result (right).

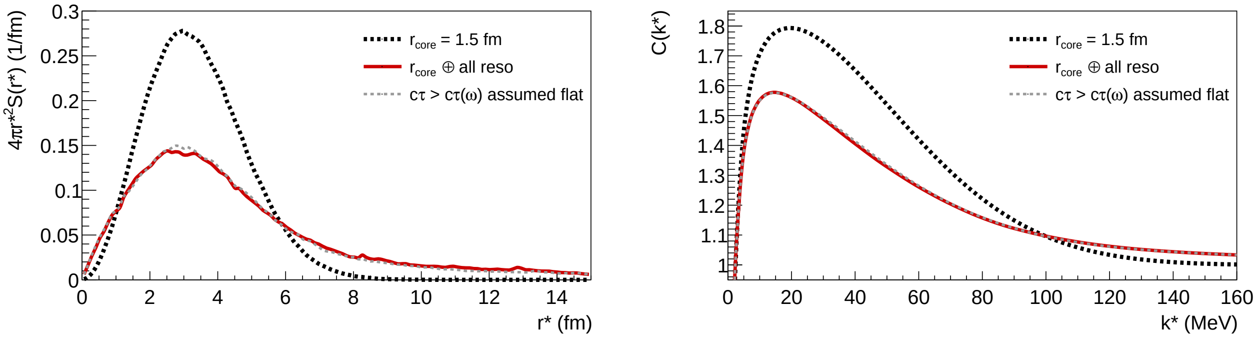

Figure 5.17: The inclusion of even longer lived resonances with $c\tau_{\mathrm{res}} > 23\,\mathrm{fm}$ into the source (left) can be perfectly described by absorbing them into the flat feed-down contribution. Leading to a dampening of the correlation function (right).

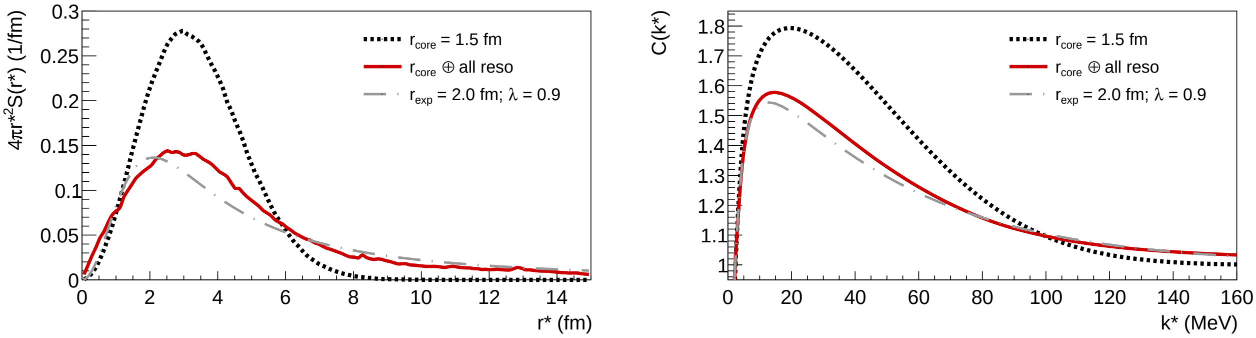

Figure 5.18: A comparison between the Gaussian core with resonances included (red line) to a exponential source (left). The resulting correlation functions (right) are in good agreement with each other.

the source profile, denoted by $S(r^*)$ in

$$C(k^*) = \int d^3r^* S(r^*)|\psi(r^*, k^*)|^2, \tag{1.1}$$

which has to be analytical, and in case the particles interact strongly, the wave function becomes non-trivial to model. In case of the latter, the best approach is to solve the two-particle stationary Schrödinger equation, which reads

$$\mathcal{H}\psi = \left[-\frac{\hbar^2}{2\mu}\Delta + V\right]\psi = E\psi, \tag{5.19}$$

where $\mu = m_1 m_2/(m_1 + m_2)$ is the reduced mass of the pair, for an arbitrary provided Hamiltonian $\mathcal{H}$, which contains every desired potential V of the interaction one is interested in. If necessary, symmetrization conditions for the wave function can be imposed, and the Coulomb interaction term can be added to the potential.

The main advantage of CATS for this work is the ability to include any source distribution to evaluate the correlation function, thus allowing to work with the non-analytical source model presented in sec. 5.5.

The fitting consists of two steps. The first is the generation of the source function via a dedicated Monte Carlo procedure, where the effect of all strongly decaying resonances with a $c\tau_{\mathrm{res}} < 5\,\mathrm{fm}$ is added on-top of the Gaussian core (details are given in sec. 5.5.2). The second is the evaluation of the correlation function based on the Koonin-Pratt Eq. (1.1). The final fit function is

$$C_{\mathrm{Fit}}(k^*) = (a + b \cdot k^* + c \cdot k^{*2}) \cdot C_{\mathrm{model}}(k^*). \tag{5.14}$$

Multiplying the baseline with the correlation function accounts for possible deformations of the correlation signal, as pairs of charged pions can be influenced by background and genuine sources of correlations at the same time. If the baseline is treated as additive the underlying assumption would be that correlations carried by the pair are either exclusively induced by the background or the genuine interaction. The structure of $C_{\mathrm{model}}(k^*)$, is described in sec. 5.4. A detailed description of the relevant λ-parameters is given in sec. 5.2. Finally the fit is performed with the assumption of a linear or a quadratic baseline.

Chapter 6

Evaluation of uncertainties

In the following the treatment of uncertainties for this work will be discussed. The statistical uncertainties are straightforward to handle, nevertheless there are multiple sources of systematic uncertainties that need to be considered in addition. They are divided into two main categories: related to the data reconstruction or related to the fit procedure.

6.1 Uncertainties of the data

The relevant sources of uncertainty for the data are the reconstruction of the tracks, and the corresponding topological and kinematic cuts. Hence, the previously reported selection criteria of the charged pions, see sec. 3.2, are modified according to Tab. 6.1, where all cuts are varied simultaneously within their specified ranges, by sampling from flat underlying distributions. For each such randomly generated set of cuts the resulting corrected correlation function is evaluated. The distribution of $C(k^*)$ values for each k^*-bin are assumed to follow a uniform distribution, and the uncertainty is assigned to the corresponding standard deviation. The latter is defined as $\mid \min - \max \mid /\sqrt{12}$, where min(max) is the minimum(maximum) value of the distribution of all the extracted ratios of correlation functions in the examined bin.

Only correlation functions for which the pair yield of charged pions is within $\pm 20\,\%$ with respect to the pair yield extracted by using the default values were considered for the calculation of the systematic uncertainty. This has the advantage that the statistical uncertainty of the variations will not be significantly altered. Moreover, the λ-parameters are evaluated for the default values, thus the systematic variations have to be small enough as to not to introduce a large bias. In total 38 correlation functions were obtained using this procedure.

Variable	Default	Variation
p_{T} (GeV/c)	0.14-4.0	0.11-5.0
$\lvert\eta\rvert$	0.8	0.6-0.9
$n_{\mathrm{TPCCluster}}$	75	75-90
DCA$_{xy,z}$ (cm)	0.3	0.25-0.35
CPR $\Delta\eta$	0.1	0.08-0.14
CPR $\Delta\phi$	0.1	0.08-0.14

Table 6.1: Variation ranges of different selection criteria of pions candidates used for the π–π correlation function. For each derived variation all the cuts were varied within their respective bounds shown above.

Fig. 6.1 shows the relative systematic uncertainty for the first k_{T}-bin (0.15–0.30 GeV/c) of the second multiplicity bin ($N_{\mathrm{Ch}} \in [19-30]$). The remaining plots are shown in the appendix D. In general the uncertainties are found to be largest in the first k^*-bins, about 3.0 % but overall for k^* larger then 10 MeV/c they are below 1 %.

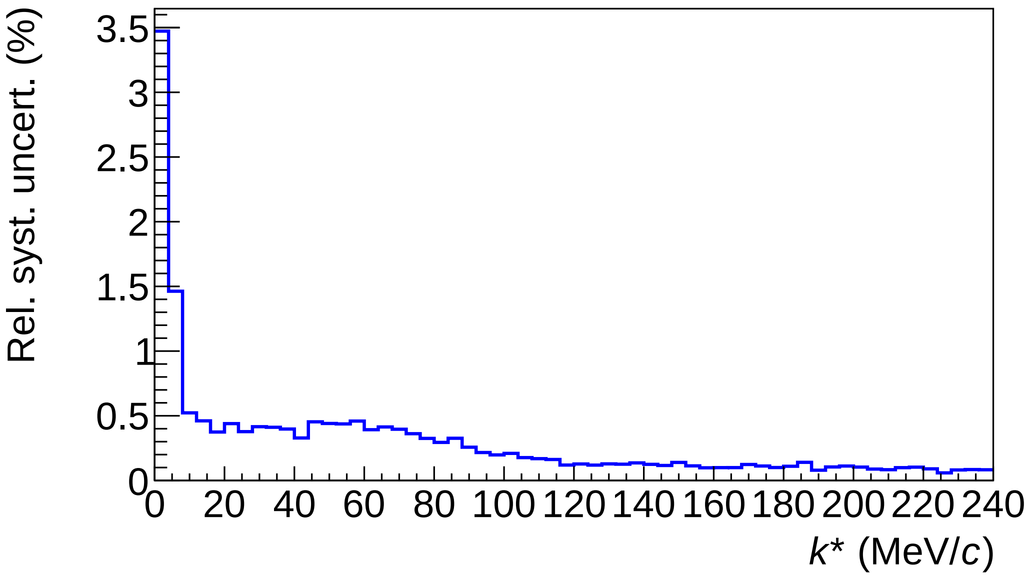

Figure 6.1: The relative systematic uncertainty for π–π correlation functions in the first k_{T}-bin (0.15–0.30) of the second multiplicity bin ($N_{\mathrm{Ch}} \in [19-30]$).

6.2 Uncertainties of the fitting procedure

Assuming that the statistical and systematic uncertainties are independent from one another, the systematic uncertainty can be expressed as Eq. 6.1,

$$\Delta x_{\mathrm{syst}} = \sqrt{\Delta x_{\mathrm{tot}}^2 - \Delta x_{\mathrm{stat}}^2}, \tag{6.1}$$

where Δx_{tot} is the total uncertainty, and Δx_{stat} is the statistical one. They can be separately evaluated, by employing the Bootstrap method [62]. This is an iterative numerical procedure, that randomly samples, bin-by-bin, the correlation function according to the experimental mean value and uncertainty. The random sampled correlation can than be fitted again, obtaining slightly different model parameters, e.g. r_{core}. Repeating the procedure multiple times allows to extract the corresponding r_{core} distribution, the standard deviation of which corresponds to the statistical uncertainty (Δx_{stat}). Obtaining Δx_{tot} is similar, however it contains additional sampling steps related to the systematic uncertainties. In particular, the correlation function is first randomly sampled from the pool of 38 variations obtained in sec. 6.1. In addition, the λ_{feed} is sampled randomly within 10 % of the default value, while the upper fit ranged is sampled from the region [327.6, 400.4] MeV/c. After that the standard Bootstrap method (e.g. resampling of the correlation function) is applied, leading to the determination of Δx_{tot}. Finally, Δx_{syst} is obtained from Eq. 6.1. Both the statistical and total uncertainties are obtained based on 45 iterations within the above described Bootstrap procedure. In general the Bootstrap method is employed to resample gathered data in order to effectively increase the amount of samples available to perform statistical analysis.

Chapter 7

Results and Discussion

The corrected same charge pion correlation functions are obtained from MB pp collision at $\sqrt{s}$ = 13 TeV. The fit results, differentially presented for each k_{T}-multiplicity bin, using the linear background assumption are shown in Figs. 7.1-7.3, while the fits using a quadratic polynomial are shown in Figs. 7.4-7.6. Every extracted corrected correlation function lies above unity indicating the attractive interaction expected to occur between two bosons such as pions. The decreasing of the correlation signal within the first few k^* bins is due to the repulsive Coulomb interaction. It should be noted that due to missing entries in the same event distribution the first few k^* bins are not filled for every correlation, e.g. for $N_{\mathrm{Ch}} \in [0-18]$ in k_{T}-bin 0.15–0.30 GeV/c the first bin is missing.

In general the fits with a linear background seem to underestimate the data for $k^* < 30\,\mathrm{MeV}/c$, while the quadratic baseline better reproduces the data. For values of k^* above $100\,\mathrm{MeV}/c$, the data are well described by the fit independently on the baseline assumption. For the highest k_{T}-bin the correlation signal is slightly suppressed for the $N_{\mathrm{Ch}} \in [0-18]$ as well as for the $N_{\mathrm{Ch}} \in [19-30]$, while for the highest multiplicity class of $N_{\mathrm{Ch}} > 30$ this effect is not observed. This behaviour might be explained in part by the fact that the production of high k_{T} charged pion pairs in low multiplicity events is, due to energy-momentum conservation, highly suppressed. In addition, even for high k_{T} and low multiplicity events, the resolution criteria for the sphericity calculation is employed, which only selects events if at least 3 tracks with $p_{\mathrm{T}} > 0.5\,\mathrm{GeV}/c$ are available. Hence the resolution criteria poses a constraint on the phase space.

7.1 Extracted m_{T} scaling behaviour of the source size

The average transverse mass is determined, from the average values $\langle k_{\mathrm{T}} \rangle$ in the selected k_{T}-bins, since $\langle m_{\mathrm{T}} \rangle = \sqrt{m_{\pi^\pm}^2 + \langle k_{\mathrm{T}} \rangle^2}$. The average values $\langle k_{\mathrm{T}} \rangle$ are calculated by evaluating the weighted average of the k_{T} distribution of the pairs from the same event and are obtained for each k_{T}-bin. In Fig. 7.7 the values of the core radius r_{core}, obtained from the fits using the linear and quadratic baseline, are shown as a function of $\langle m_{\mathrm{T}} \rangle$. In the bottom panel the corresponding reduced chi square χ^2/NDF are presented. The reported values of χ^2/NDF represent the mean of the distribution of reduced chi square obtained from the bootstrap fit procedure. The range for the calculation of χ^2/NDF was restricted to $6 < k^* < 100$ MeV/c in order to be more sensitive to the source size, while any deviations at larger k* values are most likely related to the non-femtoscopic effects. The first bin which corresponds to $k^* < 6$ MeV/c is excluded from the calculation as this data-point shows very large uncertainties.

For every multiplicity class the extracted r_{core} is decreasing for increasing $\langle m_{\mathrm{T}} \rangle$. A similar trend has been observed in the extracted r_{core} obtained from analysing baryon-baryon pairs as p–p and p–Λ [8], suggesting a common emitting source for baryons in ultra relativistic pp collisions. For the highest

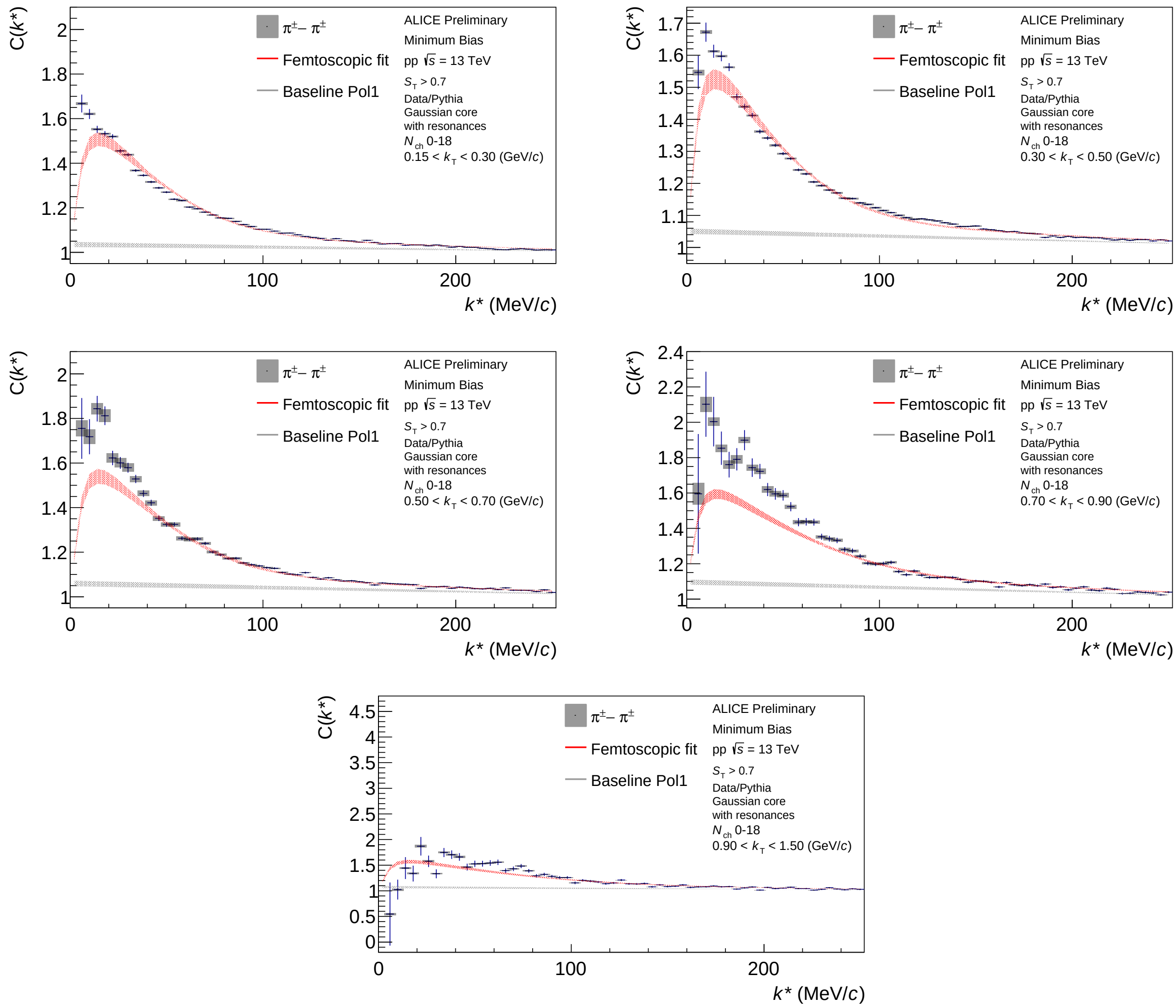

Figure 7.1: Results of the femtoscopic fit with a linear baseline in the first multiplicity bin $N_{\mathrm{Ch}} \in [0{-}18]$.

k_{T}-bin (0.90–1.5 GeV/c) and the largest multiplicity classes ($N_{\mathrm{Ch}} > 30$), a value for r_{core} between, 0.98 $\pm$ 0.02(stat.) $\pm$ 0.08(syst.) fm and 1.45 $\pm$ 0.01(stat.) $\pm$ 0.09(syst.) fm was extracted. This is remarkably close to the value of 1.31 $\pm$ 0.01(stat.) $\pm$ 0.03(syst.) fm for r_{core} found in baryon-baryon femtoscopy[1] (see Fig. 7.8). A coinciding of the extracted r_{core} values indicates a common emission source for baryons and mesons as well as possible feed down resonances. A direct comparison between the r_{core}, which are obtained in the pair rest frame, of meson and baryon pairs might be hampered by the very different transverse boosts($\gamma_{\mathrm{T}} = k_{\mathrm{T}}/m_{\mathrm{T}}$) for the pairs. In [63] this effect was investigated and a simple rescaling by $1/f$, with $f = \sqrt{(\sqrt{\gamma_{\mathrm{T}}} + 2)/3}$ was proposed in order to account for the kinematic differences. Applying the pair dependant rescaling to the central values for the r_{core}, obtained from the largest m_{T} and multiplicity bin as well as for the lowest m_{T} bin available in the baryon–baryon analysis yields, a r_{core} between 1.14 fm and 1.69 fm for the charged pions and 1.35 fm for the protons. Hence, even if r_{core} is corrected for possible kinematic differences the obtained values remain remarkably close to

[1] One should note that for the baryon-baryon femtoscopy high-multiplicity events were analysed, and hence only have a comparable N_{Ch} value in the $N_{\mathrm{Ch}} > 30$ class of this work.

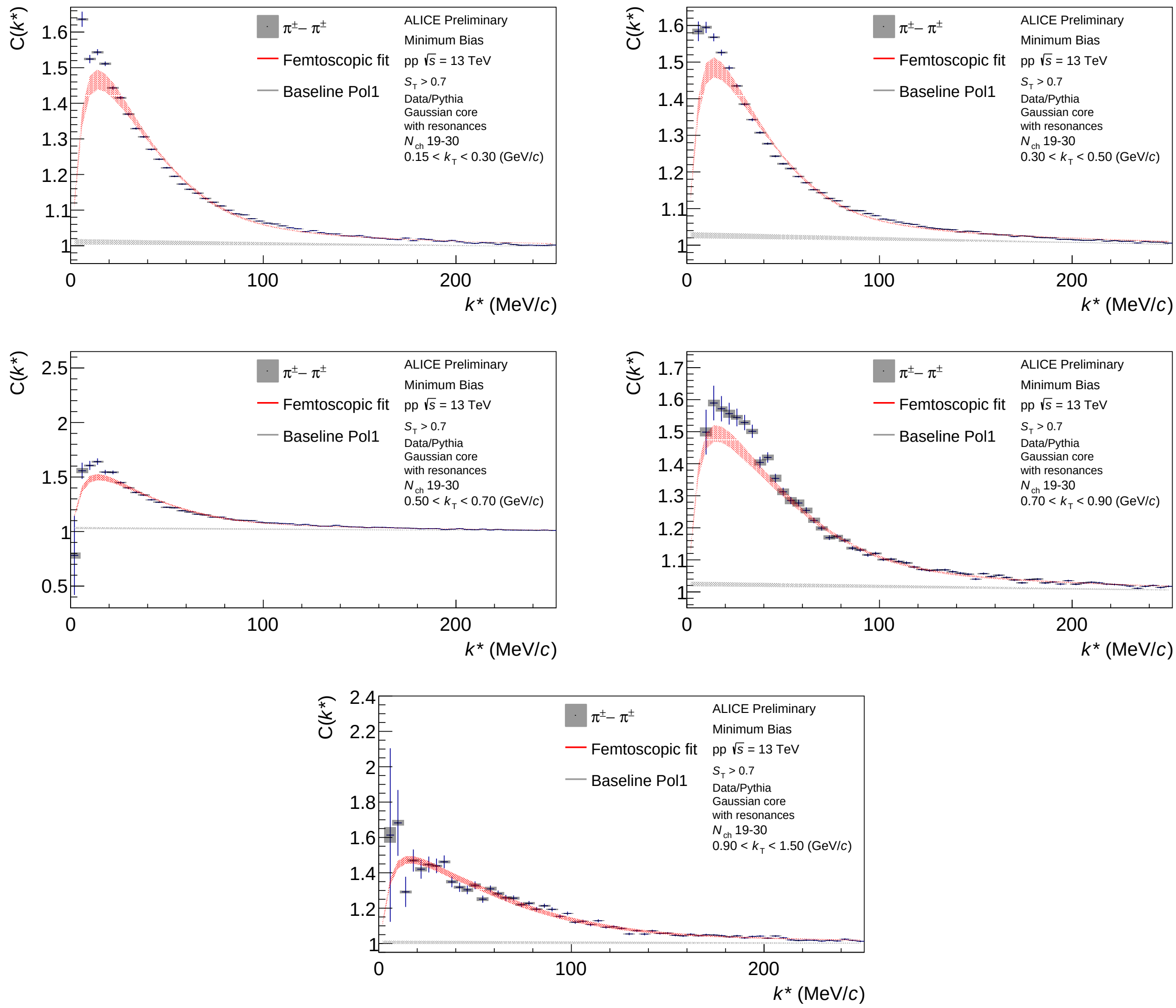

Figure 7.2: Results of the femtoscopic fit with a linear baseline in the second multiplicity bin $N_{\mathrm{Ch}} \in [19-30]$.

each other. Although definite conclusions on the exact trend of the $\langle m_{\mathrm{T}} \rangle$-scaling are due to the sizeable systematic uncertainties currently not possible, the result builds confidence that the universal source model may indeed be applied to the whole hadron–hadron sector and therefore constitute a meaning contribution to our understanding of hadronization in small systems.

The scaling behaviour is well described in heavy-ion collisions by means of hydrodynamic models with negligible transverse flow and common freeze-out [63–65]. Recent measurements performed in pp collisions of non-vanishing ν_2 coefficients in multi-particle cumulants [66, 67], observations of double-ridge structures on the near and away side in two-particle correlations [14, 15] and enhanced strangeness production [16, 17] indicate a possible presence of collective effects, as radial flow, also in small systems. The results presented in this thesis on the scaling of the emitting source provide an additional support for such a scenario. Within the picture of radial flow the plateau of extracted core radii for the first two $\langle m_{\mathrm{T}} \rangle$-bins is expected.

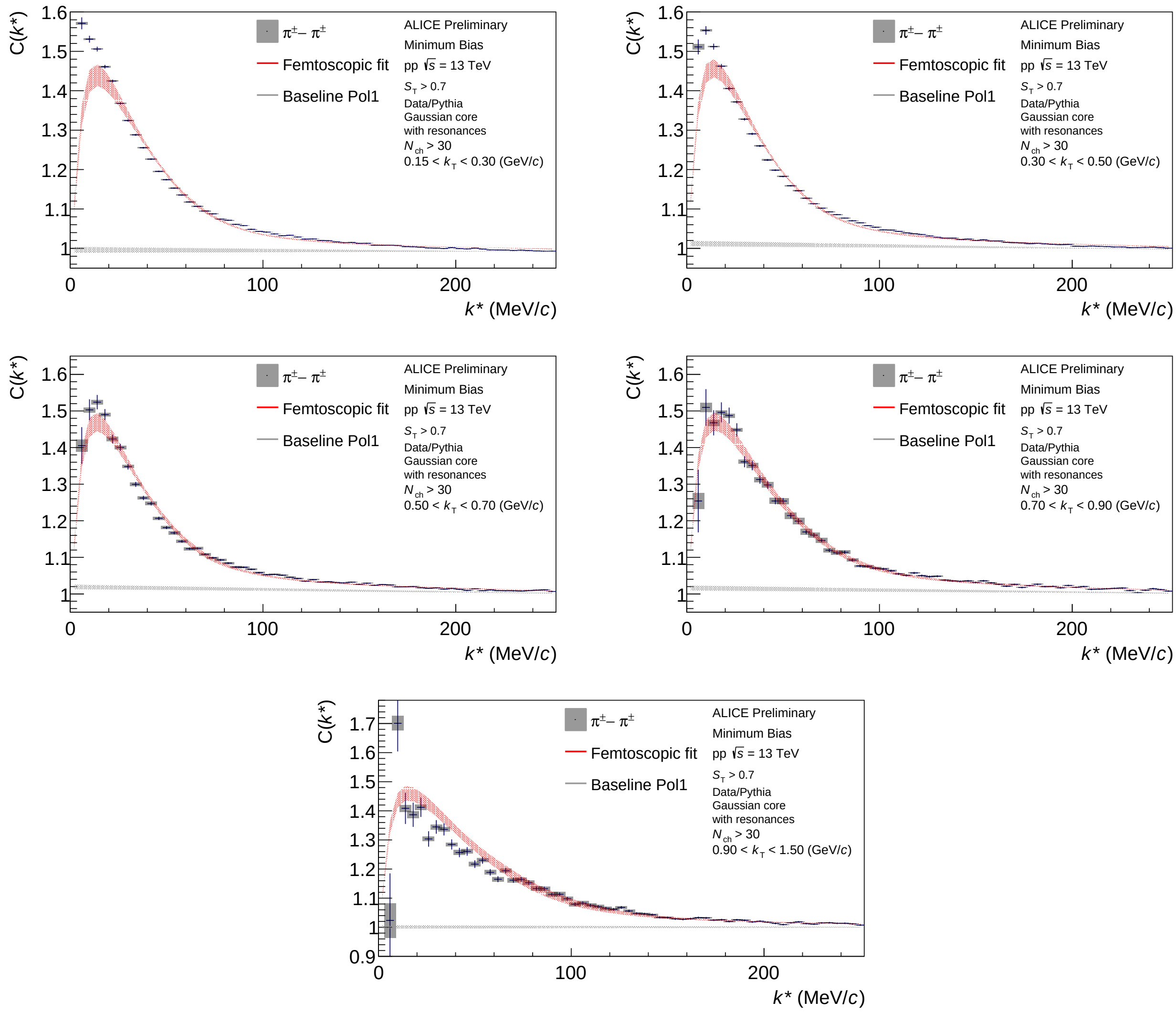

Figure 7.3: Results of the femtoscopic fit with a linear baseline in the third multiplicity bin $N_{\mathrm{Ch}} > 30$.

As an additional cross-check the data was also fitted with an exponential source, typically used in π–π femtoscopic analyses [18–20]. The fact that the m_{T} scaling behaviour is observed regardless of the assumption of the source function as well as the polynomial for the parametrization of the residual non-femtoscopic background, points to the conclusion that the observed trend is a physical feature of the data and not an artifact introduced in the fitting procedure.

The data seem to favour a quadratic baseline, as for each radii the corresponding χ^2/NDF (lower panels in the Fig. 7.7) is lower or comparable with respect to the examined case of a linear baseline. In general the quality of the fit improves with larger k_{T} values, however, especially for the low k_{T}-bins, the deviation from unity is striking, suggesting that the employed model for the fit is not optimal. Improvements can be achieved either by changing the strategy of assessing the mini-jet background present in the sample or trying to understand possible differences in the source for different k_{T}-bins. The former might be achieved by studying the mixed charge pion correlations, as the Bose-Einstein correlations are absent while the same shape for the mini-jet background is expected, although in this case the contamination introduced into the correlation due to resonances must be taken into account.

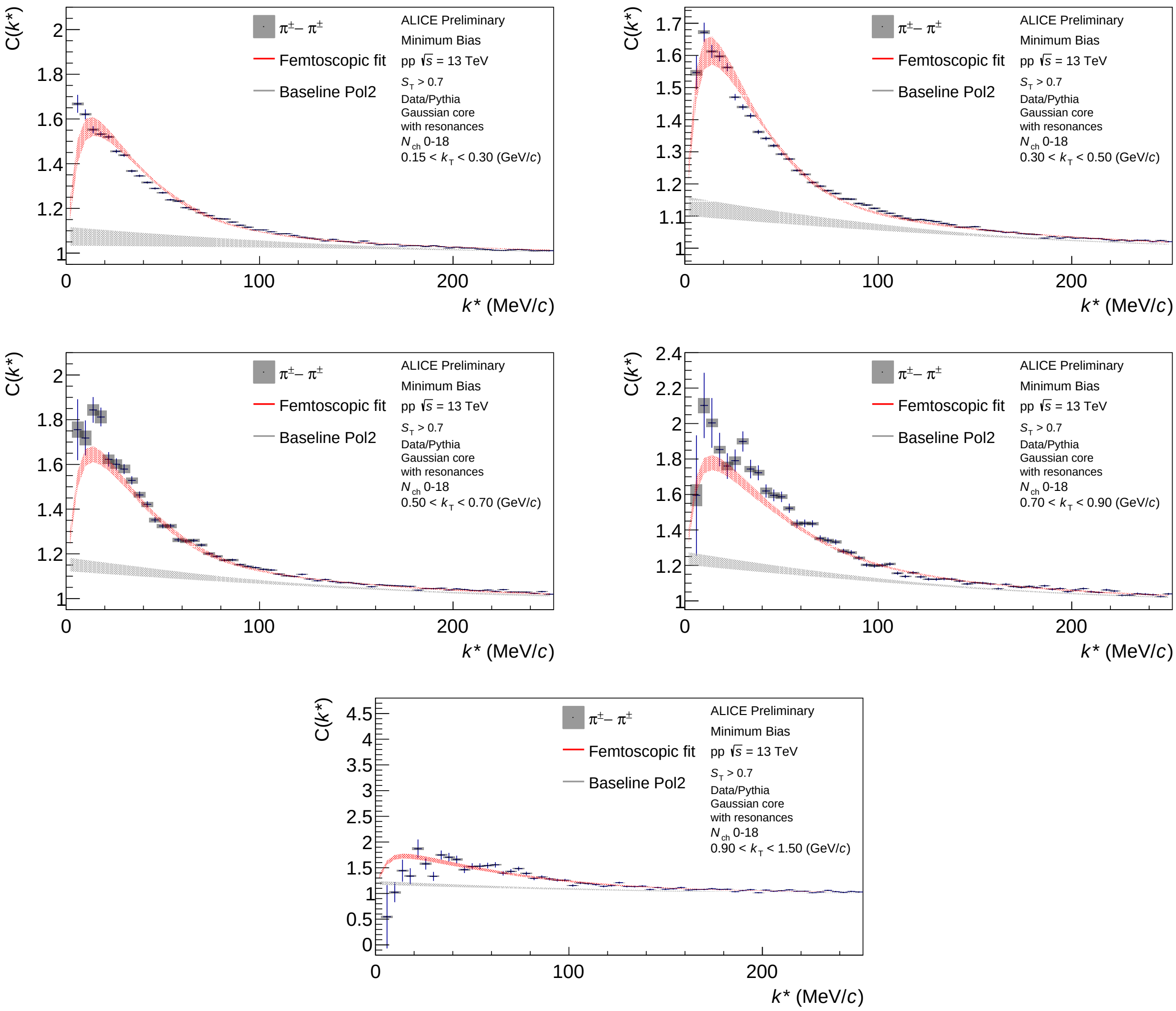

Figure 7.4: Results of the femtoscopic fit with a quadratic baseline in the first multiplicity bin $N_{\mathrm{Ch}} \in [0\text{–}18]$.

The contributions of resonances to the correlation signal are peak structures. The k^* in which the resonance contributes can be estimated by calculating the corresponding two-body decay, which gives the threshold at which k^* the resonance feeds into the k^*-bins. The width of the peak depends on the width of the feeding resonance.

For the first time a qualitative description of π–π correlations was achieved using a Gaussian distribution, modified by resonances, instead of defaulting to a traditional exponential source. This was possible by utilizing a novel technique introduced in previous femtoscopic studies [8], which allows via the use of statistic hadronization model calculations and transport models to explicitly account for the source deformation caused by the feed down of resonances. This work represents the first application of this technique to the meson–meson sector and allowed to extract the m_{T} scaling for the core radius.

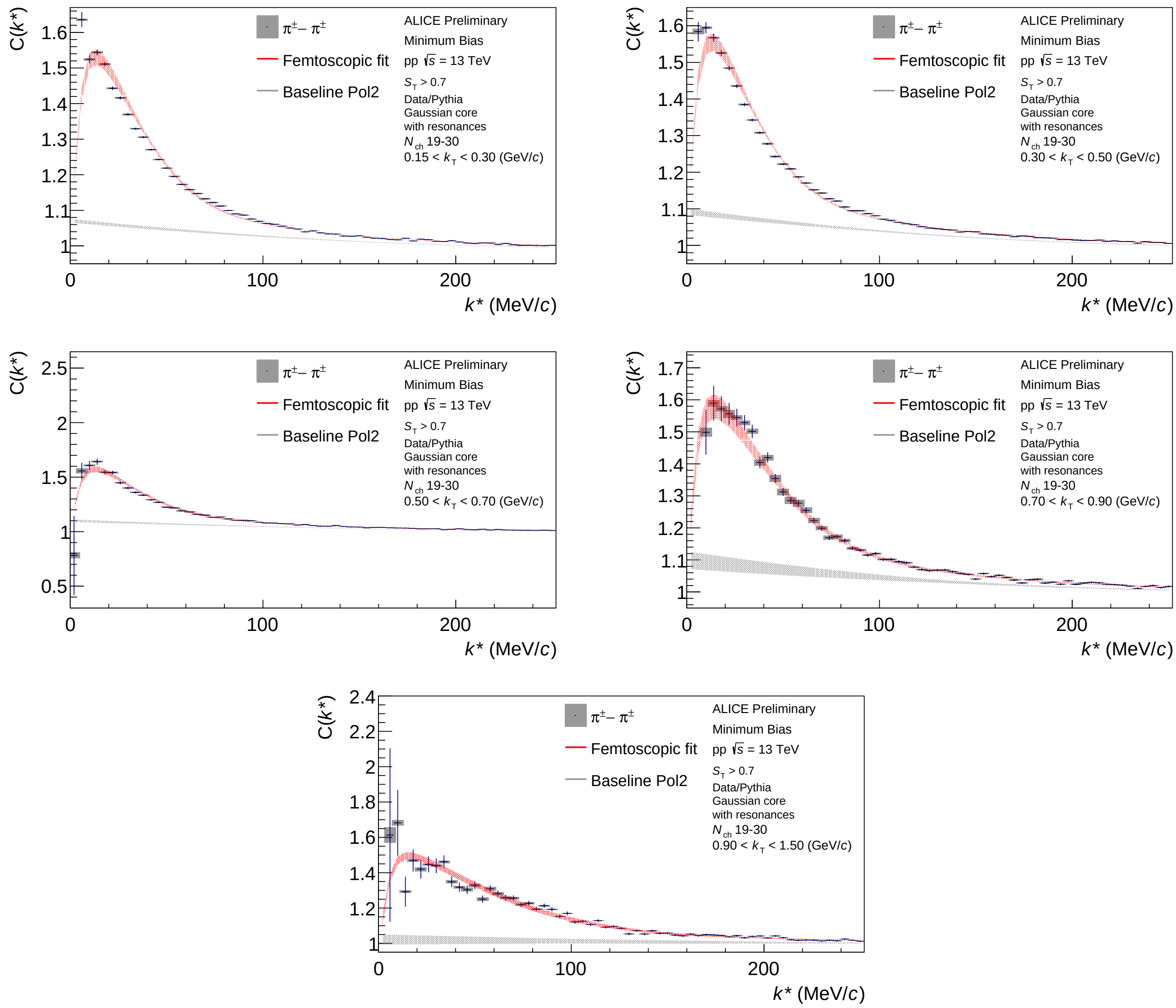

Figure 7.5: Results of the femtoscopic fit with a quadratic baseline in the second multiplicity bin $N_{\mathrm{Ch}} \in [19-30]$.

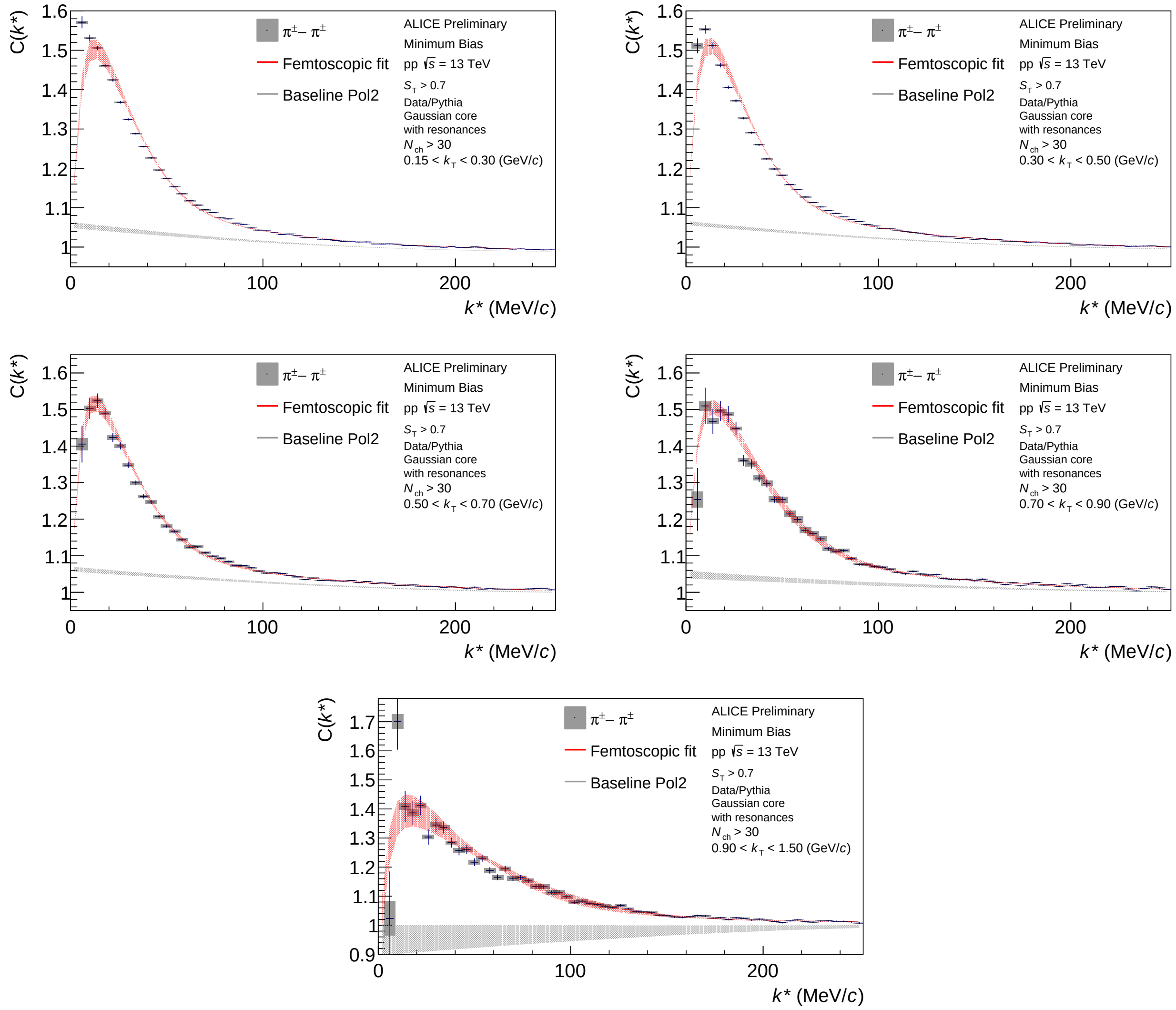

Figure 7.6: Results of the femtoscopic fit with a quadratic baseline in the third multiplicity bin $N_{\mathrm{Ch}} > 30$.

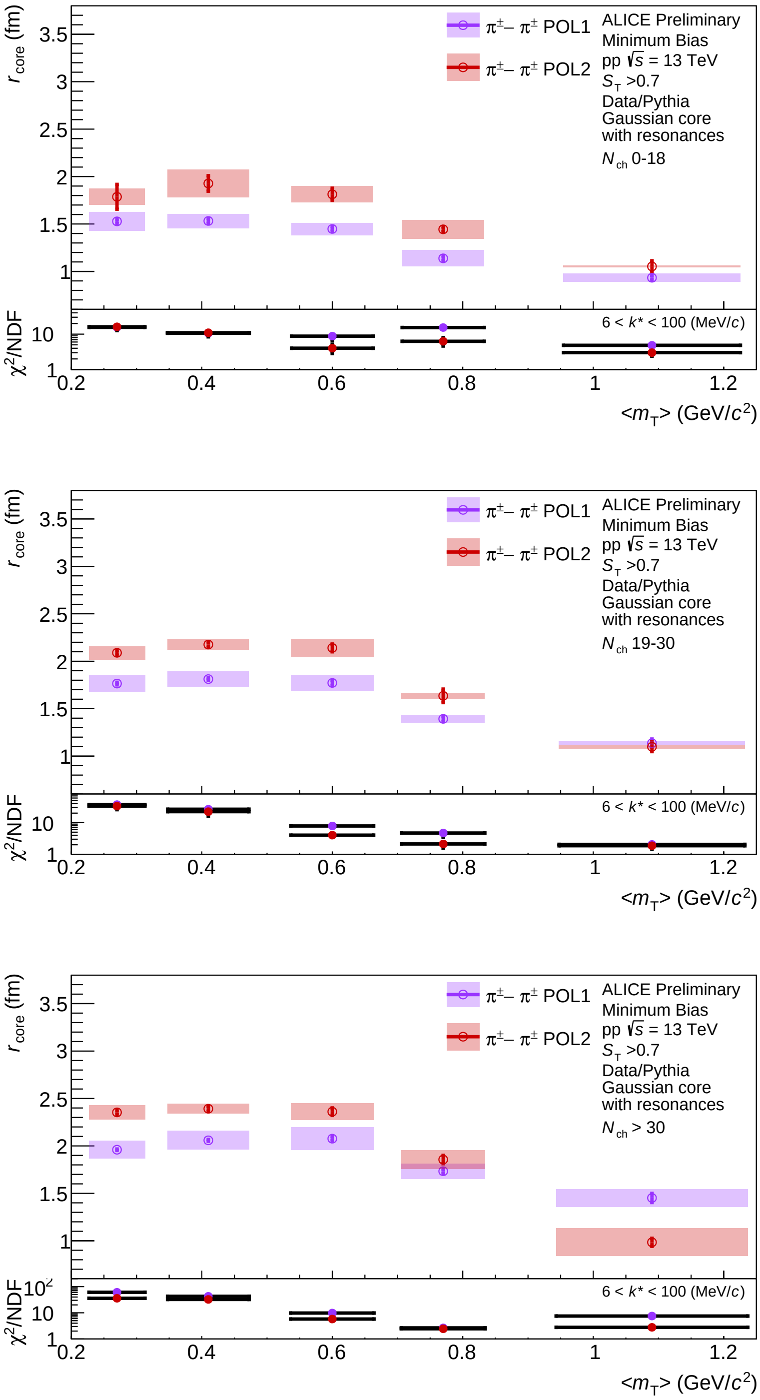

Figure 7.7: Extracted radii from the fit as a function of m_T for the three different multiplicity bins. The bottom panel shows the χ^2/NDF values for each $\langle m_T \rangle$-bin, these prefer the Pol2 baseline. From top to bottom: $N_{Ch} \in [0-18]$, $N_{Ch} \in [19-30]$ and $N_{Ch} > 30$. The systematic uncertainties are represented by colored boxes in the r_{core} vs. $\langle m_T \rangle$ plots.

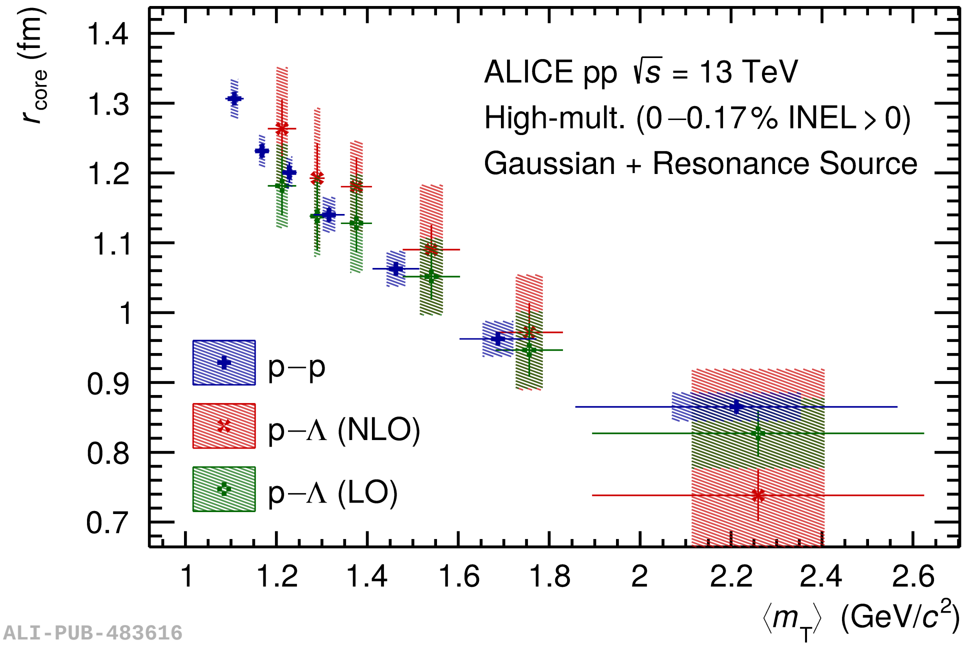

Figure 7.8: Source scaling extracted from baryon-baryon femtoscopy taken from [8].

Chapter 8

Summary and Outlook

Within this work, for the first time a qualitative description of the charged pion source is presented employing a Gaussian source, which incorporates the effect of strongly decaying resonances. It has been verified, that the source of charged pions carries significant exponential tails and hence can be parametrized by Cauchy or Levy-Stable distributions. This was achieved by extracting π–π correlation functions from minimum bias pp collisions at $\sqrt{s}$ of 13 TeV from ALICE data. It was further investigated, how resonances with intermediate lifetimes should be treated. An m_{T} scaling consistent with measurements of the baryon-baryon system [8] was found, providing further hints for a common emission source for all hadrons. As emphasized in the introduction the understanding of the mechanisms of hadronization is still incomplete and this study is important to understand how pions are produced within our current understanding. In principle this work could prove useful in improving and refining transport models as most are currently neglecting the importance of space coordinates for the production of the particles. Furthermore, since now the pion source is well understood and the modelling of the source has proven to be useful even within the meson-meson sector, the pathway is opened to study even more complicated particle pairings which include a pion. A prominent example would be the anti-kaon proton system [26], both particles are copiously produced, however, cannot be fully understood without accounting for coupled channels. Specifically for this system the driving coupled channels dynamics are due to π–Σ and π–Λ correlations, for which a precise knowledge about the pion source is needed.

Lastly a short outlook how the source model can further refined will be given. In this work the composition of the feed-down to the charged pions was assumed to be the same for each k_{T}-bin. This might prove to be a too crude approximation, as the k_{T}-intervals probe different parts of the p_{T} spectrum of the charged pions. This means that especially for low k_{T} values the softer part of the charged pion spectra is included, most likely resulting in a higher contribution of short-lived strong resonances. This could potentially modify the resonance contribution in the different k_{T}-bins, and would hence necessitate a source for each k_{T}-bin separately. The reason why this effect may not play a role in the case of the previously conducted baryon-baryon femtoscopic studies lies within the fact that only the p_{T} spectrum of the pions shows a large enhancement in the soft part of the spectrum due to the copious feed-down from resonances, whereas e.g. the p_{T} spectrum for the protons or Λ's does not. Taking this effect into account the χ^2/NDF for the fits might improve. Investigations regarding the p_{T} differential feed-down of resonances to the charged pion spectra are currently ongoing.

Appendix A

Software packages

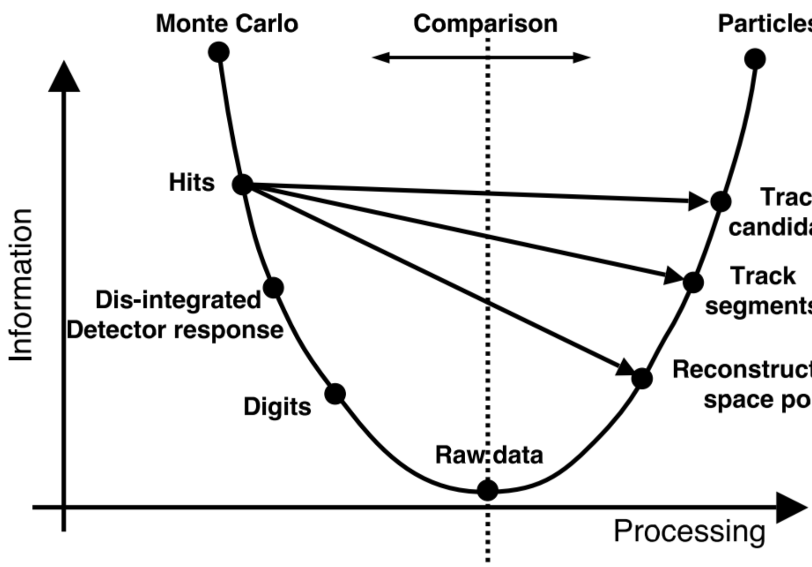

Figure A.1: Graphical representation of the usage of AliRoot taken from [68].

The processing of the gathered data is performed within the AliRoot[1] framework [69], which itself is derived from ROOT [70]. AliRoot provides all necessary base functionalities, which are needed to calculate basic physics observables and furthermore is used for the calibration of the detector, the reconstruction of events and finally data visualization. Additionally AliRoot is compatible with Monte Carlo event generators and also allows for the processing of simulated event data. Another important part of the ALICE software is AliPhysics, in which each user implements their own specific analysis task. For this work the code of the analysis was developed within the FemtoDream framework for correlation functions, which is part of AliPhysics.

[1]The software can be found at: https://github.com/alisw/AliPhysics.

Appendix B

DCA template fits: Plots for p_{T}-bins

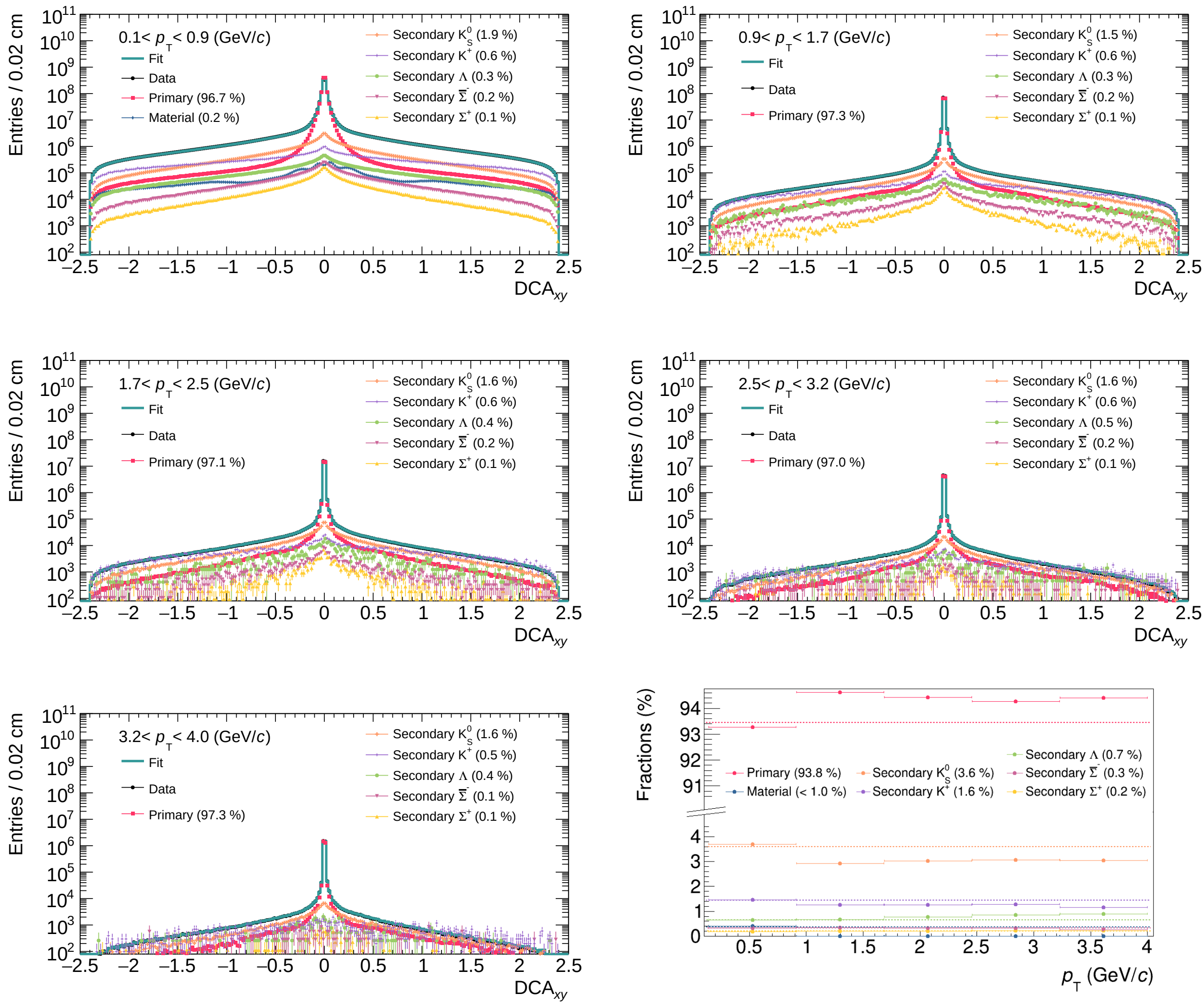

Figure B.1: DCA template fit to the experimental π^+ distributions for several p_{T} bins. A summary of the extracted fractions is presented in the lower right plot, the p_{T} weighted values are indicated by dotted lines. The results are obtained by performing a template fit with from Monte Carlo generated templates to the experimental DCA distributions of charged pions, which contain primary and secondary particles.

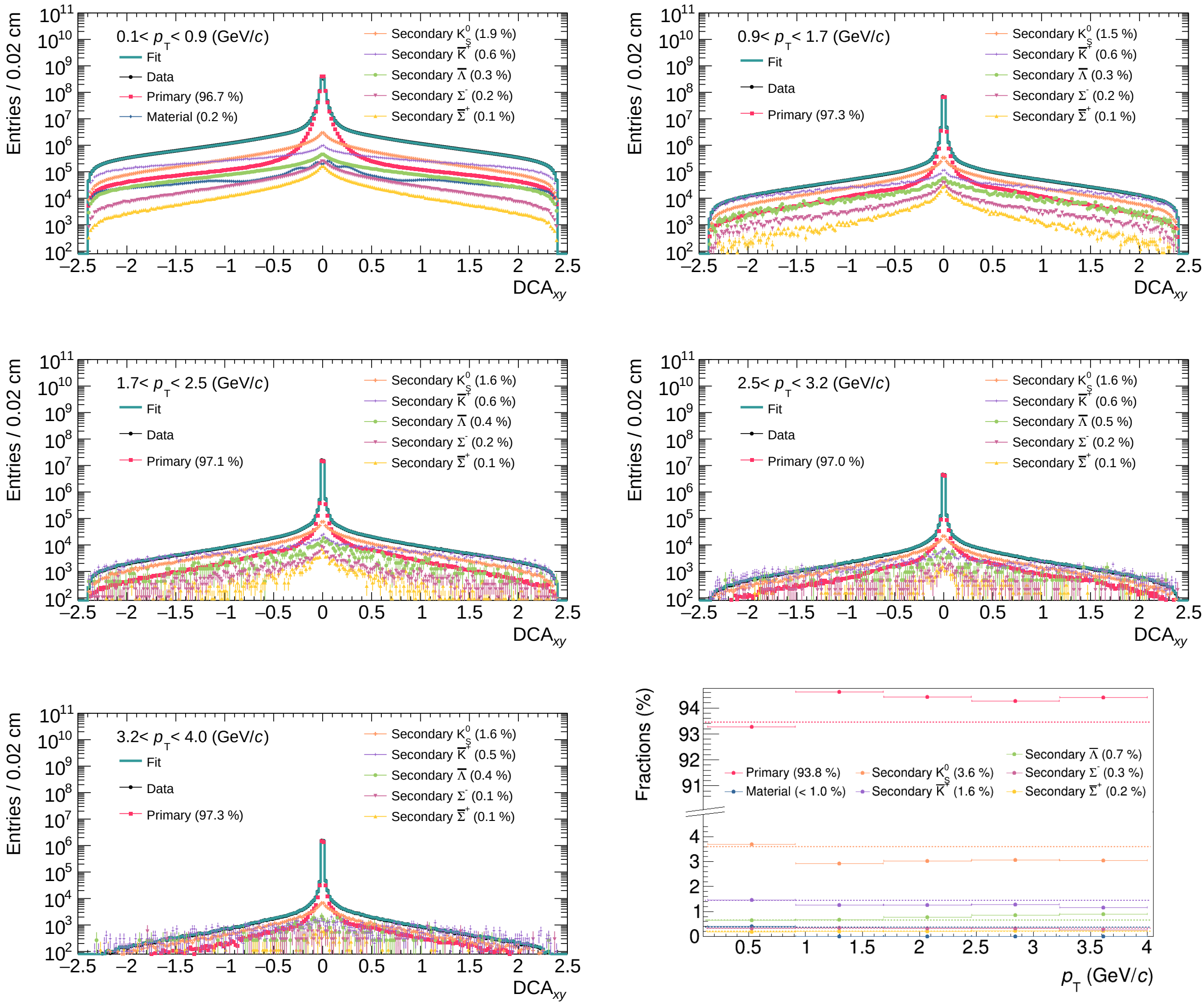

Figure B.2: DCA template fit to the experimental π^- distributions for several p_T bins. A summary of the extracted fractions is presented in the lower right plot, the p_T weighted values are indicated by dotted lines. The results are obtained by performing a template fit with from Monte Carlo generated templates to the experimental DCA distributions of charged pions, which contain primary and secondary particles.

Appendix C

Correlation functions: Plots for π^+–π^+ and π^-–π^-

The correlation function for π^+–π^+ and π^-–π^- as well as the belonging ratio is shown.

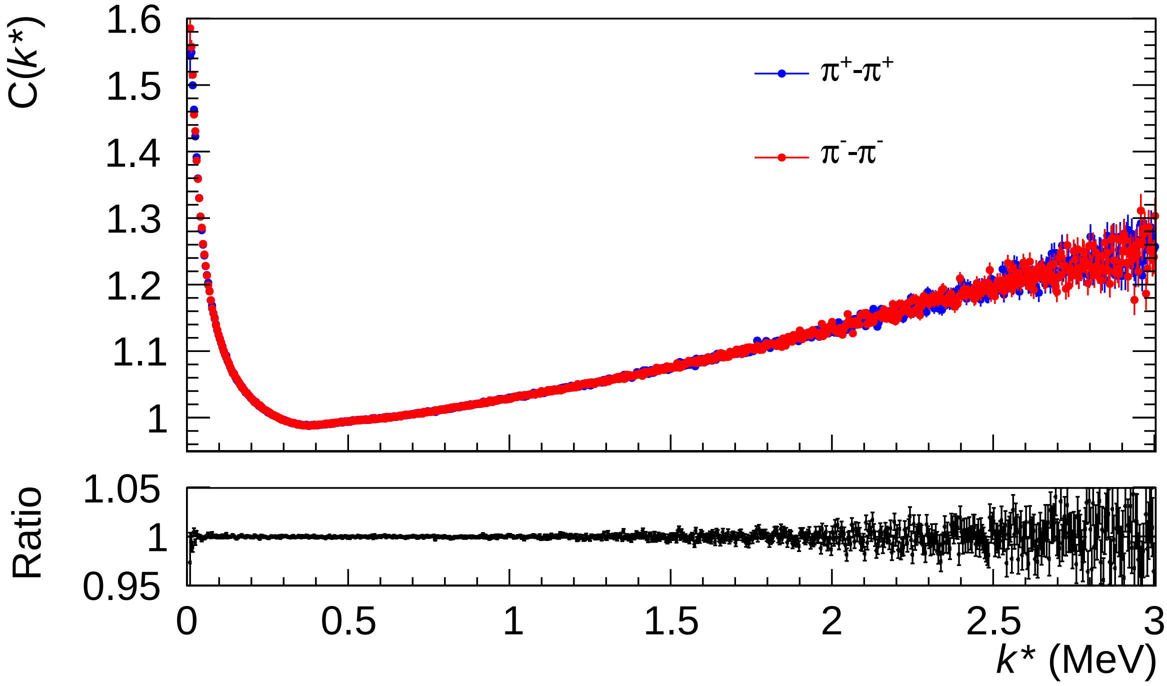

Figure C.1: The k_{T} and minimum bias multiplicity integrated correlation functions for π^+–π^+ and π^-–π^- . The ratio is shown below and is consistent with unity.

Appendix D

Uncertainty of the data: Plots for k_{T}-bins per multiplicity bin

In this appendix the relative systematic uncertainties for all k_T bins in all multiplicity bins are reported. From left to right the k_T bin increases.

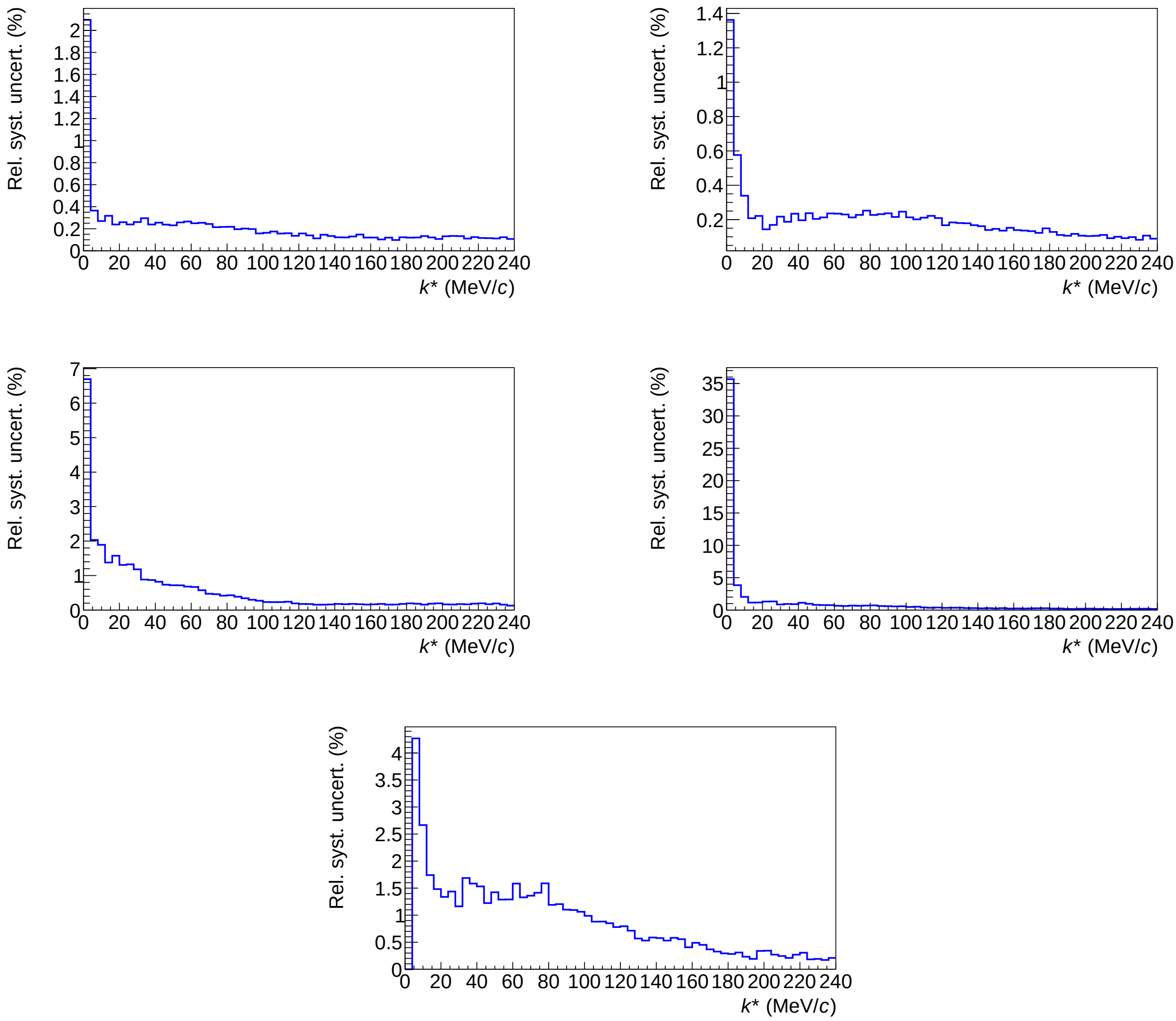

Figure D.1: The relative systematic error for π^{+}–π^{+} correlation functions in the first multiplicity bin $N_{\mathrm{Ch}} \in [1 - 18]$.

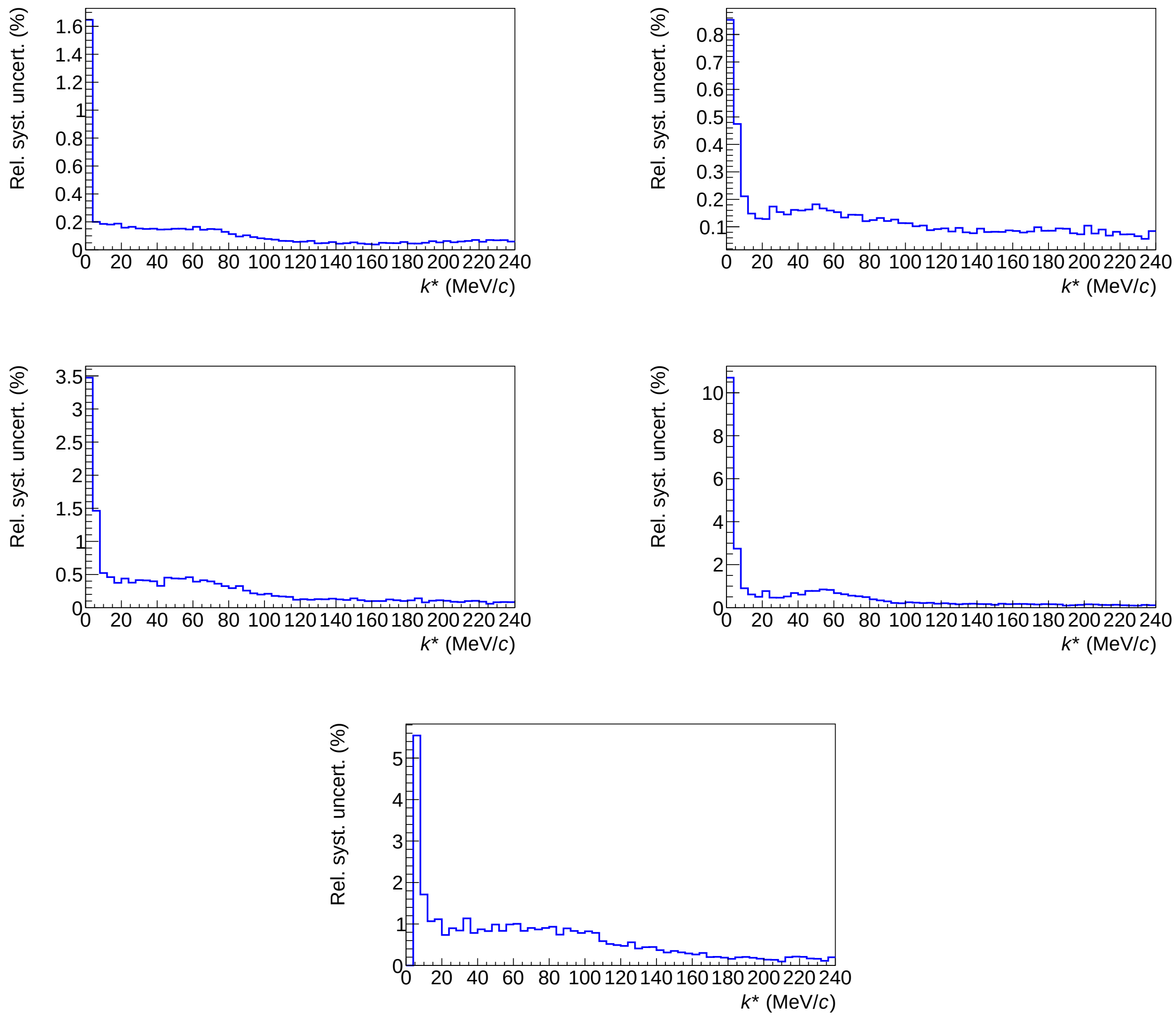

Figure D.2: The relative systematic error for π^+–π^+ correlation functions in the second multiplicity bin $N_{\mathrm{Ch}} \in [19 - 30]$.

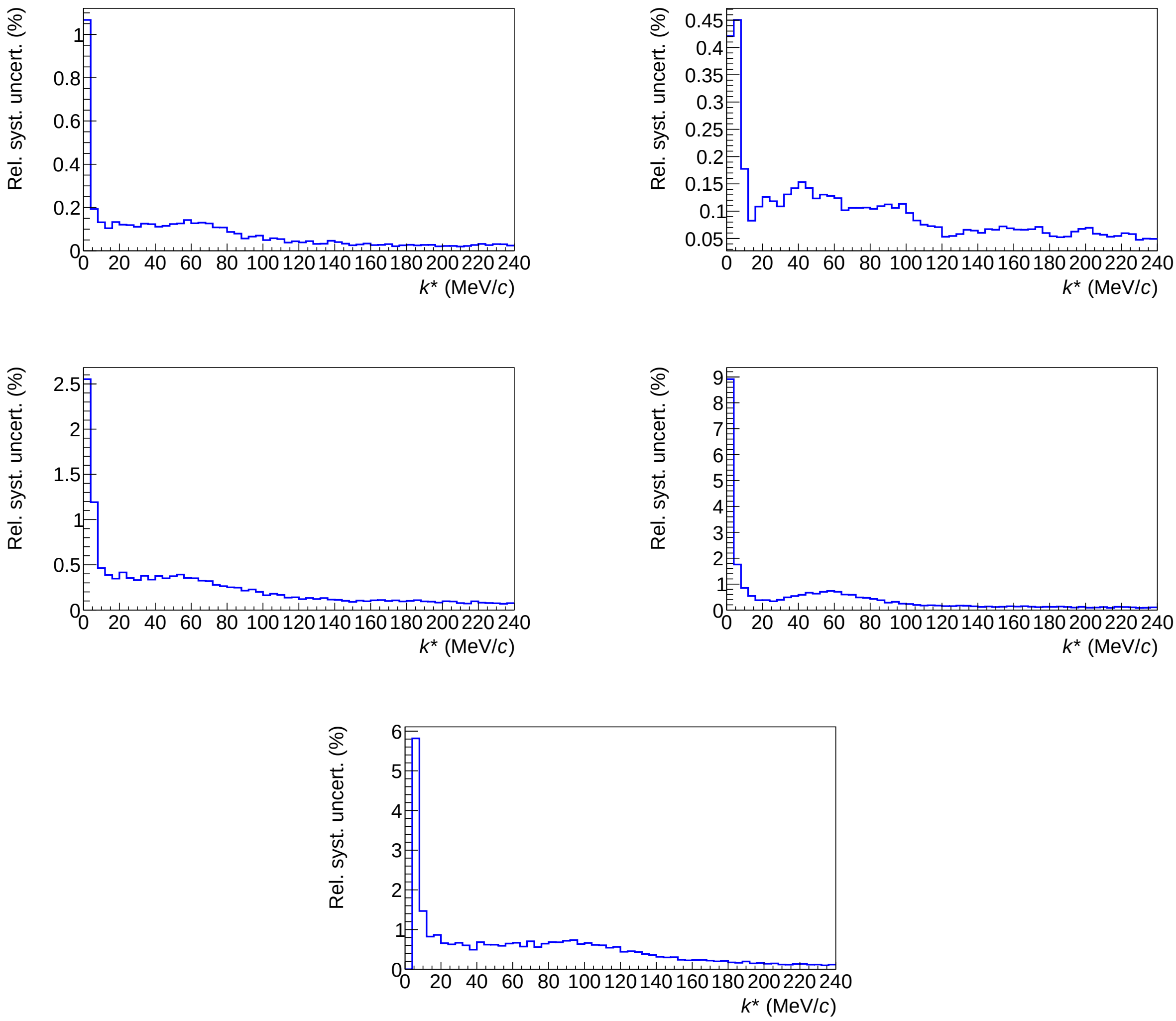

Figure D.3: The relative systematic error for π^+–π^+ correlation functions in the third multiplicity bin $N_{\mathrm{Ch}} > 30$.

Bibliography

[1] Particle Data Group. »Review of Particle Physics«. In: *Progress of Theoretical and Experimental Physics* 2020.8 (Aug. 2020). 083C01. ISSN: 2050-3911. DOI: 10.1093/ptep/ptaa104. eprint: https://academic.oup.com/ptep/article-pdf/2020/8/083C01/34673722/ptaa104.pdf. URL: https://doi.org/10.1093/ptep/ptaa104.

[2] Roman Pasechnik and Michal Šumbera. »Phenomenological Review on Quark–Gluon Plasma: Concepts vs. Observations«. In: *Universe* 3.1 (2017), p. 7. DOI: 10.3390/universe3010007. arXiv: 1611.01533 [hep-ph].

[3] Kari Eskola. »Nearly perfect quark–gluon fluid«. In: *Nature Physics* 15 (Aug. 2019). DOI: 10.1038/s41567-019-0643-0.

[4] Panagiota Foka and Małgorzata Anna Janik. »An overview of experimental results from ultra-relativistic heavy-ion collisions at the CERN LHC: Hard probes«. In: *Rev. Phys.* 1 (2016), pp. 172–194. DOI: 10.1016/j.revip.2016.11.001. arXiv: 1702.07231 [hep-ex].

[5] G. Aad et al. »Two-particle Bose–Einstein correlations in pp collisions at $\sqrt{s}$=0.9 and 7 TeV measured with the ATLAS detector«. In: *Eur. Phys. J. C* 75 (2015), p. 466. ISSN: 1434-6052. DOI: 10.1140/epjc/s10052-015-3644-x.

[6] Albert M Sirunyan et al. »Bose-Einstein correlations of charged hadrons in proton-proton collisions at $\sqrt{s} = 13$ TeV«. In: *JHEP* 03 (2020), p. 014. DOI: 10.1007/JHEP03(2020)014.

[7] Jaroslav Adam et al. »One-dimensional pion, kaon, and proton femtoscopy in Pb-Pb collisions at $\sqrt{s_{\mathrm{NN}}}$ =2.76 TeV«. In: *Phys. Rev. C* 92 (2015), p. 054908. DOI: 10.1103/PhysRevC.92.054908.

[8] S. Acharya et al. »Search for a common baryon source in high-multiplicity pp collisions at the LHC«. In: *Physics Letters B* 811 (2020), p. 135849. ISSN: 0370-2693. DOI: https://doi.org/10.1016/j.physletb.2020.135849. URL: https://www.sciencedirect.com/science/article/pii/S0370269320306523.

[9] ALICE. »Scattering Studies with Low-Energy Kaon-Proton Femtoscopy in Proton-Proton Collisions at the LHC«. In: *Phys. Rev. Lett.* 124 (9 Mar. 2020), p. 092301. DOI: 10.1103/PhysRevLett.124.092301. URL: https://link.aps.org/doi/10.1103/PhysRevLett.124.092301.

[10] »Constraining the KN coupled channel dynamics using femtoscopic correlations at the LHC«. In: (May 2022). arXiv: 2205.15176 [nucl-ex].

[11] Shreyasi Acharya et al. »Exploring the $\mathrm{N}\Lambda$-$\mathrm{N}\Sigma$ coupled system with high precision correlation techniques at the LHC«. In: (Apr. 2021). arXiv: 2104.04427 [nucl-ex].

[12] Shreyasi Acharya et al. »Investigation of the p-Σ^0 interaction via femtoscopy in pp collisions«. In: *Phys. Lett. B* 805 (2020), p. 135419. DOI: 10.1016/j.physletb.2020.135419. arXiv: 1910.14407 [nucl-ex].

[13] Alice Collaboration and Aydan Garibli. »Unveiling the strong interaction among hadrons at the LHC«. In: *Nature* (Dec. 2020), pp. 232–238.

[14] Alice Ohlson. »Correlations, multiplicity distributions, and the ridge in pp and p-Pb collisions«. In: *EPJ Web of Conferences* 141 (Jan. 2017), p. 01006. DOI: 10.1051/epjconf/201714101006.

[15] Vardan Khachatryan et al. »Observation of Long-Range Near-Side Angular Correlations in Proton-Proton Collisions at the LHC«. In: *JHEP* 09 (2010), p. 091. DOI: 10.1007/JHEP09(2010)091. arXiv: 1009.4122 [hep-ex].

[16] Shreyasi Acharya et al. »Multiplicity dependence of (multi-)strange hadron production in proton-proton collisions at $\sqrt{s} = 13$ TeV«. In: *Eur. Phys. J. C* 80.2 (2020), p. 167. DOI: 10.1140/epjc/s10052-020-7673-8. arXiv: 1908.01861 [nucl-ex].

[17] Jaroslav Adam et al. »Enhanced production of multi-strange hadrons in high-multiplicity proton-proton collisions«. In: *Nature Phys.* 13 (2017), pp. 535–539. DOI: 10.1038/nphys4111. arXiv: 1606.07424 [nucl-ex].

[18] CMS Collaboration. »Bose-Einstein correlations of charged hadrons in proton-proton collisions at $\sqrt{s} = 13$ TeV«. In: (Oct. 2019).

[19] LHCb Collaboration. »Bose–Einstein Correlations in pp and pPb Collisions at LHCb †«. In: *Universe* 5 (Apr. 2019), p. 95. DOI: 10.3390/universe5040095.

[20] Morad Aaboud et al. »Femtoscopy with identified charged pions in proton-lead collisions at $\sqrt{s_{\mathrm{NN}}} = 5.02$ TeV with ATLAS«. In: *Phys. Rev. C* 96.6 (2017), p. 064908. DOI: 10.1103/PhysRevC.96.064908. arXiv: 1704.01621 [hep-ex].

[21] R. Hanbury Brown and R. Q. Twiss. »A Test of a new type of stellar interferometer on Sirius«. In: *Nature* 178 (1956), pp. 1046–1048. DOI: 10.1038/1781046a0.

[22] Gerson Goldhaber et al. »Influence of Bose-Einstein Statistics on the Antiproton-Proton Annihilation Process«. In: *Phys. Rev.* 120 (1 Oct. 1960), pp. 300–312. DOI: 10.1103/PhysRev.120.300. URL: https://link.aps.org/doi/10.1103/PhysRev.120.300.

[23] Michael Annan Lisa et al. »Femtoscopy in relativistic heavy ion collisions«. In: *Ann. Rev. Nucl. Part. Sci.* 55 (2005), pp. 357–402. DOI: 10.1146/annurev.nucl.55.090704.151533. arXiv: nucl-ex/0505014 [nucl-ex].

[24] Volodymyr Vovchenko and Horst Stoecker. »Thermal-FIST: A package for heavy-ion collisions and hadronic equation of state«. In: *Comput. Phys. Commun.* 244 (2019), pp. 295–310. DOI: 10.1016/j.cpc.2019.06.024. arXiv: 1901.05249 [nucl-th].

[25] T. Pierog et al. »EPOS LHC: Test of collective hadronization with data measured at the CERN Large Hadron Collider«. In: *Phys. Rev. C* 92 (2015), p. 034906. DOI: 10.1103/PhysRevC.92.034906.

[26] Yuki Kamiya et al. »K^-p Correlation Function from High-Energy Nuclear Collisions and Chiral SU(3) Dynamics«. In: *Phys. Rev. Lett.* 124 (13 Apr. 2020), p. 132501. DOI: 10.1103/PhysRevLett.124.132501. URL: https://link.aps.org/doi/10.1103/PhysRevLett.124.132501.

[27] Lyndon Evans and Philip Bryant. »LHC Machine«. In: *Journal of Instrumentation* 3.08 (Aug. 2008), S08001–S08001. DOI: 10.1088/1748-0221/3/08/s08001. URL: https://doi.org/10.1088/1748-0221/3/08/s08001.

[28] Elena Botta. »Particle identification performance at ALICE«. In: *5th Large Hadron Collider Physics Conference*. Sept. 2017. arXiv: 1709.00288 [nucl-ex].

[29] ALICE Figure Repository. »ALICE Schematics«. In: (May 2017). General Photo. URL: https://cds.cern.ch/record/2263642.

[30] Betty Bezverkhny Abelev et al. »Performance of the ALICE Experiment at the CERN LHC«. In: *Int. J. Mod. Phys. A* 29 (2014), p. 1430044. DOI: 10.1142/S0217751X14300440. arXiv: 1402.4476 [nucl-ex].

[31] K Aamodt et al. »Alignment of the ALICE Inner Tracking System with cosmic-ray tracks«. In: *JINST* 5 (2010), P03003. DOI: 10.1088/1748-0221/5/03/P03003. arXiv: 1001.0502 [physics.ins-det].

[32] ALICE collaboration. »The ALICE TPC, a large 3-dimensional tracking device with fast readout for ultra-high multiplicity events«. In: *Nuclear Instruments and Methods in Physics Research Section A: Accelerators, Spectrometers, Detectors and Associated Equipment* 622.1 (2010), pp. 316–367. ISSN: 0168-9002. DOI: https://doi.org/10.1016/j.nima.2010.04.042. URL: https://www.sciencedirect.com/science/article/pii/S0168900210008910.

[33] A. Akindinov et al. »Performance of the ALICE Time-Of-Flight detector at the LHC«. In: *Eur. Phys. J. Plus* 128 (2013), p. 44. DOI: 10.1140/epjp/i2013-13044-x.

[34] ALICE Figure Repository. »ALICE TPC-PID Performance«. In: (July 2018). TPC PID. URL: https://alice-figure.web.cern.ch/node/8670.

[35] ALICE Figure Repository. »ALICE TOF-PID Performance«. In: (Sept. 2016). TOF PID. URL: https://alice-figure.web.cern.ch/node/9564.

[36] K Aamodt et al. »The ALICE experiment at the CERN LHC«. In: *Journal of Instrumentation* 3.08 (2008), S08002. URL: http://stacks.iop.org/1748-0221/3/i=08/a=S08002.

[37] Torbjörn Sjöstrand, Stephen Mrenna and Peter Skands. »PYTHIA 6.4 physics and manual«. In: *Journal of High Energy Physics* 2006.05 (2006), p. 026. URL: http://stacks.iop.org/1126-6708/2006/i=05/a=026.

[38] F. Carena, W. Carena and S. Chapeland. »The ALICE data acquisition system«. In: *Nuclear Instruments and Methods in Physics Research Section A: Accelerators, Spectrometers, Detectors and Associated Equipment* 741 (2014), pp. 130–162. ISSN: 0168-9002. DOI: https://doi.org/10.1016/j.nima.2013.12.015. URL: https://www.sciencedirect.com/science/article/pii/S0168900213016987.

[39] L.V. Malinina et al. »Identical charged pion and kaon femtoscopic correlations in pp collisions at $\sqrt{\mathbf{s}} = \mathbf{13}$ TeV with event-shape selection.« In: *ALICE intern* (). URL: https://alice-notes.web.cern.ch/node/911.

[40] Shreyasi Acharya et al. »Event-shape and multiplicity dependence of freeze-out radii in pp collisions at $\sqrt{s} = 7$ TeV«. In: *JHEP* 09 (2019), p. 108. DOI: 10.1007/JHEP09(2019)108. arXiv: 1901.05518 [nucl-ex].

[41] Betty Abelev et al. »Transverse sphericity of primary charged particles in minimum bias proton-proton collisions at $\sqrt{s} = 0.9$, 2.76 and 7 TeV«. In: *Eur. Phys. J.* C72 (2012), p. 2124. DOI: 10.1140/epjc/s10052-012-2124-9. arXiv: 1205.3963 [hep-ex].

[42] Shreyasi Acharya et al. »Production of light-flavor hadrons in pp collisions at $\sqrt{s} = 7$ and $\sqrt{s} = 13$ TeV«. In: *Eur. Phys. J. C* 81.3 (2021), p. 256. DOI: 10.1140/epjc/s10052-020-08690-5. arXiv: 2005.11120 [nucl-ex].

[43] Shreyasi Acharya et al. »p-p, p-Λ and Λ-Λ correlations studied via femtoscopy in pp reactions at $\sqrt{s} = 7$ TeV«. In: *Phys. Rev. C* 99.2 (2019), p. 024001. DOI: 10.1103/PhysRevC.99.024001. arXiv: 1805.12455 [nucl-ex].

[44] Urs Achim Wiedemann and Ulrich W. Heinz. »Resonance contributions to HBT correlation radii«. In: *Phys. Rev. C* 56 (1997), pp. 3265–3286. DOI: 10.1103/PhysRevC.56.3265. arXiv: nucl-th/9611031.

[45] J. Bolz et al. »Resonance decays and partial coherence in Bose-Einstein correlations«. In: *Phys. Rev. D* 47 (9 May 1993), pp. 3860–3870. DOI: 10.1103/PhysRevD.47.3860. URL: https://link.aps.org/doi/10.1103/PhysRevD.47.3860.

[46] Adam Kisiel et al. »Femtoscopy in hydrodynamics-inspired models with resonances«. In: *Phys. Rev. C* 73 (6 June 2006), p. 064902. DOI: 10.1103/PhysRevC.73.064902. URL: https://link.aps.org/doi/10.1103/PhysRevC.73.064902.

[47] »The ALICE definition of primary particles«. In: (June 2017). URL: https://cds.cern.ch/record/2270008.

[48] F. Becattini and Ulrich W. Heinz. »Thermal hadron production in p p and p anti-p collisions«. In: *Z. Phys. C* 76 (1997). [Erratum: Z.Phys.C 76, 578 (1997)], pp. 269–286. DOI: 10.1007/s002880050551. arXiv: hep-ph/9702274.

[49] Volodymyr Vovchenko, Benjamin Dönigus and Horst Stoecker. »Canonical statistical model analysis of p-p , p -Pb, and Pb-Pb collisions at energies available at the CERN Large Hadron Collider«. In: *Phys. Rev. C* 100.5 (2019), p. 054906. DOI: 10.1103/PhysRevC.100.054906. arXiv: 1906.03145 [hep-ph].

[50] T. Kim B. Kim. »Analysis note for pseudorapidity density of charged particles in proton-proton collisions at $\sqrt{\mathbf{s}} = \mathbf{5.02}$ TeV«. In: *ALICE intern* (). URL: %7Bhttps://alice-notes.web.cern.ch/node/603%7D.

[51] S. Agostinelli et al. »Geant4—a simulation toolkit«. In: *Nuclear Instruments and Methods in Physics Research Section A: Accelerators, Spectrometers, Detectors and Associated Equipment* 506.3 (2003), pp. 250–303. ISSN: 0168-9002. DOI: https://doi.org/10.1016/S0168-9002(03)01368-8. URL: https://www.sciencedirect.com/science/article/pii/S0168900203013688.

[52] A. Nappi. »A Pitfall in the use of extended likelihood for fitting fractions of pure samples in mixed samples«. In: *Comput. Phys. Commun.* 180 (2009), pp. 269–275. DOI: 10.1016/j.cpc.2008.10.008. arXiv: 0803.2711 [physics.data-an].

[53] O. Arnold. »Two-particle baryon femtoscopy studies in proton-proton reactions at $\sqrt{s_{\mathrm{NN}}} = 7$ TeV measured with the ALICE experiment at the Large Hadron Collider«. In: (). URL: %7Bhttps://alice-notes.web.cern.ch/node/552%7D.

[54] D. Mihaylov et al. »p-Λ femtoscopy in pp High Multiplicity reactions at $\sqrt{\mathbf{s}} = \mathbf{13}$ TeV«. In: (). URL: https://alice-notes.web.cern.ch/node/900.

[55] B. Hohlweger et al. »p-p femtoscopy in pp High Multiplicity reactions at $\sqrt{\mathbf{s}} = \mathbf{13}$ TeV«. In: (). URL: https://alice-notes.web.cern.ch/node/891.

[56] A. Mathis et al. »p-p, p-Λ, p-Ξ and Λ-Λ correlations studied via femtoscopy in pp reactions at $\sqrt{s} = 13$ TeV«. In: (). URL: https://alice-notes.web.cern.ch/node/738.

[57] D. L. Mihaylov et al. »A femtoscopic correlation analysis tool using the Schrödinger equation (CATS)«. In: *The European Physical Journal C* 78.5 (May 2018), p. 394. ISSN: 1434-6052. DOI: 10.1140/epjc/s10052-018-5859-0. URL: https://doi.org/10.1140/epjc/s10052-018-5859-0.

[58] M. G. Bowler. »Extended sources, final state interactions and Bose-Einstein correlations«. In: *Zeitschrift für Physik C Particles and Fields* 39 (Mar. 1988), pp. 81–88. URL: https://doi.org/10.1007/BF01560395.

[59] G. Colangelo, J. Gasser and H. Leutwyler. »$\pi\pi$ scattering«. In: *Nucl. Phys. B* 603 (2001), pp. 125–179. DOI: 10.1016/S0550-3213(01)00147-X. arXiv: hep-ph/0103088.

[60] A. M. Sirunyan et al. »Bose-Einstein correlations in pp, pPb, and PbPb collisions at $\sqrt{s_{\mathrm{NN}}} = 0.9$–7 TeV«. In: *Phys. Rev. C* 97 (6 2018), p. 064912. DOI: 10.1103/PhysRevC.97.064912.

[61] Urs Achim Wiedemann and Ulrich Heinz. »New class of Hanbury-Brown–Twiss parameters«. In: *Phys. Rev. C* 56 (2 Aug. 1997), R610–R613. DOI: 10.1103/PhysRevC.56.R610.

[62] William H. Press et al. *Numerical Recipes 3rd Edition: The Art of Scientific Computing*. Cambridge University Press.

[63] Adam Kisiel, Mateusz Gałażyn and Piotr Bożek. »Pion, kaon, and proton femtoscopy in Pb–Pb collisions at $\sqrt{s_{\mathrm{NN}}}$=2.76 TeV modeled in (3+1)D hydrodynamics«. In: *Phys. Rev. C* 90.6 (2014), p. 064914. DOI: 10.1103/PhysRevC.90.064914. arXiv: 1409.4571 [nucl-th].

[64] A. N. Makhlin and Yu. M. Sinyukov. »Hydrodynamics of Hadron Matter Under Pion Interferometric Microscope«. In: *Z. Phys. C* 39 (1988). Ed. by R. M. Weiner, p. 69. DOI: 10.1007/BF01560393.

[65] B.R. Schlei et al. »Transverse expansion and effective radii of sources in high energy collisions«. In: *Physics Letters B* 293.3 (1992), pp. 275–281. ISSN: 0370-2693. DOI: https://doi.org/10.1016/0370-2693(92)90883-6. URL: https://www.sciencedirect.com/science/article/pii/0370269392908836.

[66] Alice Ohlson. »Collective behavior in small systems«. In: *Nucl. Phys. A* 967 (2017). Ed. by Ulrich Heinz, Olga Evdokimov and Peter Jacobs, pp. 97–104. DOI: 10.1016/j.nuclphysa.2017.06.023. arXiv: 1901.00710 [nucl-ex].

[67] V Khachatryan et al. »Evidence for collectivity in pp collisions at the LHC«. In: *Physics Letters B* 765 (Feb. 2017).

[68] K. Aamodt et al. »The ALICE experiment at the CERN LHC«. In: *JINST* 3 (2008), S08002. DOI: 10.1088/1748-0221/3/08/S08002.

[69] Rene Brun, Federico Carminati and Fons Rademakers. »The ALICE Off-Line Strategy: A Successful Migration to OO«. In: (Jan. 2000).

[70] Rene Brun and Fons Rademakers. »ROOT — An object oriented data analysis framework«. In: *Nuclear Instruments and Methods in Physics Research Section A: Accelerators, Spectrometers, Detectors and Associated Equipment* 389.1 (1997). New Computing Techniques in Physics Research V, pp. 81–86. ISSN: 0168-9002. DOI: https://doi.org/10.1016/S0168-9002(97)00048-X. URL: https://www.sciencedirect.com/science/article/pii/S016890029700048X.

Acknowledgements

First of all, before going into details, I want to express my biggest gratitude to all of my colleagues at the E62 chair, especially Prof. Laura Fabbietti for managing the many nice people (which during COVID was most probably one the hardest jobs on the planet known to humankind), and for providing ever since my bachelor thesis an fantastic environment to conduct research and hone my understanding of physics. The time spent with colleagues during these years, in private and at the office, are an invaluable experience for me and teached me a lot about camaraderie and team-work. This work wouldn't and couldn't have reached the level of quality without the support of many people. Therefore I would like to thank my both extremely talented supervisors Dr. Valentina Mantovani Sarti (Vale) and Dr. Dimitar Lubomirov Mihaylov (Dimi), both of you were never bothered to discuss with me even my most trivial questions and always had an open ear regardless of the topic. From Vale I learned a great deal how to navigate inside the jungle of resonances and thermal predictions. And Dimi, the Jedi-Grandmaster of femtoscopic sources, couldn't have done a better job of imparting even a fraction of his knowledge to this padawan. Further I would like to thank the 'Femto Oldtimers', Dr. Andreas Mathis (Andi) and Dr. Bernhard Hohlweger (Bernie), although both may have already left the chair, the legacy of Femtoscopy is still going strong. And basically my knowledge of how to extract correlations from data comes purely from discussions and tutorials given by Andi and Bernie. Last but not least I want to thank Dr. Ante Bilandzic for his humor, introducing me to the wonderland of bash, and making me familiar with the concept of bootstrapping. All of which greatly helped in dealing with challanges I was confronted with during the completion of this work. I also have to thank people outside the chair Dr. Benjamin Dönigus and Dr. Volodymyr Vovchenko for explaining some part of Thermal-FIST to me and helping me in getting the output in which I am interested in. As the data for this work were provided by the ALICE collaboration I would like to thank the thousands of people necessary to operate and maintain the detector and especially the many talented physicist (inside the PWG) I had the joy of working together. Finally I would like to express my sincere gratitude to my familiy, my parents, my brother, and grandparents, who were ever supporting me on my way.

List of Figures

List of Tables